

NGR-05-002-160

(NASA-CR-155562) AN INVESTIGATION OF N78-16984  
TECHNIQUES FOR THE MEASUREMENT AND  
INTERPRETATION OF COSMIC RAY ISOTOPIC  
ABUNDANCES Ph.D. Thesis (California Inst. of Tech.) 243 p HC A11/MF A01 CSCI 03B G3/93 02516  
Unclas

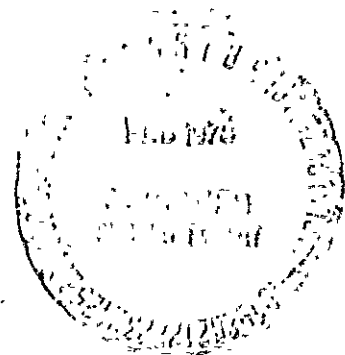
---

CALIFORNIA INSTITUTE OF TECHNOLOGY

---

PASADENA, CALIFORNIA

---



AN INVESTIGATION OF TECHNIQUES FOR THE  
MEASUREMENT AND INTERPRETATION OF  
COSMIC RAY ISOTOPIC ABUNDANCES

Thesis by  
Mark Edward Wiedenbeck

SRL 77-8

December 9, 1977

AN INVESTIGATION OF TECHNIQUES FOR THE  
MEASUREMENT AND INTERPRETATION OF  
COSMIC RAY ISOTOPIC ABUNDANCES

Thesis by  
Mark Edward Wiedenbeck

In Partial Fulfillment of the Requirements  
for the Degree of  
Doctor of Philosophy

California Institute of Technology  
Pasadena, California

1978

(Submitted December 9, 1977)

ACKNOWLEDGMENTS

I am pleased to acknowledge the invaluable contribution made to this work by my advisor, Professor Edward Stone. It was at his suggestion that this investigation was undertaken and it was his advice which has, on a number of occasions, greatly contributed to its progress.

I also wish to acknowledge Professor Rochus Vogt for the many insights which he has provided both concerning this work and concerning the role of the physicist in the world.

Numerous other persons have contributed directly and indirectly to this work. To them I am deeply grateful. Don Skelton has contributed much to the mechanical design of the HEIST experiment and has provided many interesting ideas concerning the joys of experimental physics. James Zumberge and Dr. Frank Hagen have contributed extensively both in effort and ideas to the development of the experiment. Without the fine electronics design work of Bill Blodgett and the electronic support of Daryl Dzioba this experiment would not have been possible. Capable assistance was provided during the early phases of development of the instrument by Thomas Stoughton and by Mark Heuschen.

This work has also benefitted from the comments of Drs. Alan Cummings, Frank Marshall, Tom Garrard, Gordon Hurford, Dick Mewaldt and Sol Vidor as well as those of Rick Cook and Steward Hartman.

Dr. Perez-Mendez and Mr. Jerry Stoker have graciously provided suggestions and materials which have aided in the construction of the hodoscope system.

We have received invaluable assistance in performing heavy ion calibrations of the instrument from the Heckman group at the Lawrence Berkeley Laboratory.

I thank Dr. Michel Cassé for valuable conversations concerning the interpretation of cosmic ray observations.

I am grateful to the National Science Foundation, the State of California and the California Institute of Technology for financial assistance during my graduate years.

Finally, my deepest thanks are due to my wife, Pam, for her years of support and for her criticism of the form and content of this thesis.

This work has been supported by NASA under NGR 05 002 160.

ABSTRACT

An instrument, the Caltech High Energy Isotope Spectrometer Telescope (HEIST), has been developed to measure isotopic abundances of cosmic ray nuclei in the charge range  $3 \leq Z \leq 28$  and the energy range between 30 and 800 MeV/nuc by employing an energy loss -- residual energy technique. Measurements of particle trajectories and energy losses are made using a multiwire proportional counter hodoscope and a stack of CsI(Tl) crystal scintillators, respectively. A detailed analysis has been made of the mass resolution capabilities of this instrument.

Landau fluctuations set a fundamental limit on the attainable mass resolution, which for this instrument ranges between  $\sim .07$  AMU for  $Z \sim 3$  and  $\sim .2$  AMU for  $Z \sim 26$ . Contributions to the mass resolution due to uncertainties in measuring the path-length and energy losses of the detected particles are shown to degrade the overall mass resolution to between  $\sim .1$  AMU ( $Z \sim 3$ ) and  $\sim .3$  AMU ( $Z \sim 26$ ).

A formalism, based on the leaky box model of cosmic ray propagation, is developed for obtaining isotopic abundance ratios at the cosmic ray sources from abundances measured in local interstellar space for elements having

three or more stable isotopes, one of which is believed to be absent at the cosmic ray sources. This purely secondary isotope is used as a tracer of secondary production during propagation. This technique is illustrated for the isotopes of the elements O, Ne, S, Ar and Ca.

The uncertainties in the derived source ratios due to errors in fragmentation and total inelastic cross sections, in observed spectral shapes, and in measured abundances are evaluated. It is shown that the dominant sources of uncertainty are uncorrelated errors in the fragmentation cross sections and statistical uncertainties in measuring local interstellar abundances.

These results are applied to estimate the extent to which uncertainties must be reduced in order to distinguish between cosmic ray production in a solar-like environment and in various environments with greater neutron enrichments.

TABLE OF CONTENTS

<u>Section</u>	<u>Title</u>	<u>Page</u>
1.	INTRODUCTION	1
2.	INSTRUMENTATION	10
2.1	Measurement Technique	10
2.2	Instrument -- Overall Description	38
2.3	Trajectory Measurement	55
2.4	Energy Measurements	95
3.	CALCULATIONS	131
3.1	Information from Isotopic Composition	132
3.1.1	Source Abundances	132
3.1.2	Secondary Production and Propagation	134
3.1.3	Radioactive Species	136
3.2	Cosmic Ray Propagation -- Leaky Box Model	139
3.3	Secondary Tracer Formalism	146
3.3.1	Analysis of Uncertainties -- Motivation	150
3.3.2	Source Ratio Uncertainties	152
3.3.2.1	Abundances of Parent Nuclei	157
3.3.2.2	Fragmentation Cross Sections	163
3.3.2.3	Total Inelastic Cross Sections	167
3.3.2.4	Spectral Indices	168
3.3.2.5	Isotopic Abundances	170
3.3.2.6	Summary of Uncertainties	171
3.3.3	Curves for Interpreting Local Abundances	173

3.3.3.1	Source Ratio Curves	176
3.3.3.2	Statistical Error Curves	186
3.3.3.3	Calculational Error Curves	187
3.3.4	Range of Source Abundances	190
3.3.5	Solar Modulation Effects	198
4.	SUMMARY AND CONCLUSIONS	204
APPENDICIES		
A.	UNCERTAINTY IN MEASURED ABUNDANCE RATIOS	211
A.1	Statistical Errors	211
A.2	Systematic Errors	214
B.	TRAJECTORY UNCERTAINTIES	216
B.1	Absolute Position Uncertainty	220
B.2	Uncertainty in $\sec\theta$	221
REFERENCES		224

LIST OF FIGURES

<u>Figure Number</u>	<u>Title</u>	<u>Page</u>
1	Geometry for $\Delta E-E'$ Measurement.	11
2	Proton range-energy relation in CsI.	1b
3	Relation between abundance uncertainty, mass resolution and number of events.	23
4	Resolution required to obtain an inflection point in a bi-Gaussian distribution.	2b
5	Effect of $\Delta E$ detector thickness on mass resolution.	31
6	Mass uncertainty due to Landau fluctuations vs. particle range.	3b
7	Cross sectional view of HEIST instrument.	39
8	Scale drawings of sensors in HEIST instrument.	42
9	Intervals of charge and energy accessible to the HEIST instrument.	4b
10	Geometrical factor vs. maximum angle of incidence.	50
11	Expanded view of single MWPC.	5b
12	Distribution of image charge on MWPC cathode.	61
13	MWPC delay line pulse shapes.	65
14	Block diagram of position sensing circuitry.	68
15	MWPC signal processing example.	71
16	Effect of MWPC suppressor.	75
17	MWPC charge collection vs. applied high voltage.	78
18	MWPC transfer function (time vs. position).	81

<u>Figure Number</u>	<u>Title</u>	<u>Page</u>
19	MWPC position resolution and linearity.	84
20	MWPC position resolution vs. signal amplitude.	87
21	MWPC time (position) distributions.	89
22	Uncertainty in $\Delta E$ detector thickness vs. angle of incidence.	93
23	Mechanical assembly of scintillator stack.	96
24	Contour map of D2 scintillator thickness.	101
25	Nominal response to particles stopping in D7.	104
26	Block diagram of pulse height analyzer circuitry.	107
27	Saturation characteristics of EMI 9530R pm tube.	110
28	Energy measurement uncertainties vs. deposited energy.	114
29	Contour map of light collection efficiency in D4 scintillator.	118
30	Temperature variation of pm tubes during balloon flight.	124
31	Mass resolution vs. particle range for $^9\text{Be}$ , $^{16}\text{O}$ , $^{28}\text{Si}$ and $^{56}\text{Fe}$ .	128
32	Relationship between source and local abundance ratios and source ratio uncertainties due to statistical errors and fragmentation cross section errors.	177
33	Number of events and level of cross section errors needed to distinguish between solar-like source and sources with various neutron enrichments.	193
B.1	Geometry used in analysis of trajectory uncertainties.	218

LIST OF TABLES

<u>Table Number</u>	<u>Title</u>	<u>Page</u>
1	Partial derivatives used in mass resolution evaluation.	21
2	HEIST detector thicknesses.	35
3	Positions of HEIST sensors.	45
4	HEIST count rates for various elements vs. magnetic cutoff and atmospheric depth.	53
5	Mechanical characteristics of HEIST MWPC's.	58
6	Delay line characteristics.	64
7	Source and local cosmic ray abundances.	154
8	Sources of uncertainty in source abundance ratios.	156
9	Effect of solar modulation on local abundance ratios.	203
B.1	Position uncertainties at various depths in the HEIST scintillator stack.	222

## 1. INTRODUCTION

Measurements of the nuclear composition (both elemental and isotopic) of material on the earth, in meteorites, in the sun and stars, and in the interstellar medium have contributed greatly to our understanding of the astrophysical conditions under which this material was synthesized. In fact, such measurements have been essential to the development of the theory of nucleosynthesis. The material observed in these sites generally exists in thermal equilibrium with its surroundings and this has probably been the case ever since it was synthesized.

The nuclei in the cosmic radiation form a sample of matter which can be observed at kinetic energies greatly in excess of thermal energies (cosmic rays have been observed at energies up to  $10^{20}$  eV (Brownlee et al., 1970)). At present it is not clear whether this material is formed in sites different from those which produce the matter observed in the solar system, or whether the same sites produce both populations of matter with the cosmic rays simply being that small fraction which subsequently gets accelerated to near-relativistic energies. Not only is it possible that the cosmic rays will provide information concerning astrophysical objects other than

those which produced the solar system material, but they also may contain information concerning the time evolution of such sources. Measurements of radioactive nuclides in the cosmic rays (Hagen et al., 1977; Garcia-Munoz et al., 1977b; Webber et al., 1977) lead to estimates of  $\sim 10^6$ - $10^7$  years as the age of the cosmic rays. This is much younger than the age of solar system material, which has been estimated to be  $\sim 4.5 \times 10^9$  years.

Improvements in the instrumentation used for measurements of the nuclear component of the cosmic rays have led to measurements of 1) the abundances of individual elements in the cosmic rays in the charge range  $Z \leq 28$ , 2) isotopic abundances of the elements H and He, 3) elemental abundances in the charge range  $Z > 28$ , 4) mean masses of elements with  $3 \leq Z \leq 28$ , and 5) isotopic abundances of elements with  $3 \leq Z \leq 8$ . Reviews of these improving measurements of the elemental and isotopic composition of the cosmic rays have been presented by Garcia-Munoz (1973), Stone (1973), Lund (1975), Meyer (1975) and Waddington (1977). In addition, a number of instruments which should be capable of isotopic abundance measurements for all elements up through Ni have recently begun making measurements or will soon do so. It is believed that such measurements of the isotopic composition of the cosmic rays will further our

understanding of the astrophysical processes involved in the synthesis and acceleration of this material.

In section 2 of this thesis we discuss the development of one such instrument and present a detailed analysis of the influence of a variety of instrumental parameters on the mass resolution attainable with this instrument. In addition to evaluating the expected performance of our instrument, this analysis serves to indicate those aspects of the measurement in which improvements in the instrumentation can significantly improve the capabilities of this instrument or of other instruments of similar design.

Techniques which have been used for cosmic ray mass determination involve measuring two parameters such as total energy, range in a selected absorbing material, velocity, magnetic rigidity, specific ionization rate or intensity of Čerenkov light emission. Each of these quantities can be expressed as a product of a function of velocity and a function of the particle's charge and/or mass. The fact that only a limited number of discrete values of charge and mass are possible allows one in some cases to determine both of these quantities from measurements of only two to the parameters listed above. Techniques for measuring charge and mass using

combinations of measurements of total energy, specific ionization and Cerenkov emission have been reviewed by Stone (1974).

The Caltech High Energy Isotope Spectrometer Telescope (HEIST) is designed to measure the mass of cosmic ray particles in the charge range  $3 \leq Z \leq 28$  with energies between 30 and 800 MeV/nuc (the energy interval varying with particle charge within these limits). An energy-loss - residual energy technique is employed. This technique involves measuring the amount of energy that the particle loses in passing through an absorber of known thickness and measuring the residual energy with which the particle emerges from this absorber. This technique has been employed by a number of investigators for measuring both elemental and isotopic abundances. References to publications describing these measurements can be found in the reviews listed above.

Several innovations have been included in the HEIST instrument. CsI(Tl) crystal scintillators are used to make the energy loss measurements. The use of crystal scintillators rather than the commonly used plastic scintillators should significantly reduce the degree of saturation of the scintillation efficiency when the scintillator is exposed to the heavily ionizing particles

of interest here. The effects of scintillator saturation on mass resolution are discussed by Webber and Kish (1972). Also, a stack of eight scintillators of progressively increasing thickness have been employed. By summing the energy losses in all detectors prior to the one in which a particle stops we can insure that the absorber thickness is a large fraction of the particle's range. This technique significantly improves the mass resolution over that obtainable using a thin  $dE/dx$  detector followed by a thick total energy detector. A multiwire proportional counter (MWPC) hodoscope is used to make precise measurements ( $\sigma_{MWPC} \sim 1$  mm) of the particle's trajectory. These measurements make it possible to make corrections for the particle's angle of incidence and for variations of thickness and light collection efficiency with position in the scintillators. Also a technique whereby signals from two different dynodes of each photomultiplier tube are analyzed using a logarithmic pulse height analyzer allows us to achieve the large dynamic range required in order to measure signals throughout the charge range of interest while still maintaining an adequate pulse height resolution throughout that range.

Instruments such as the one which we describe should be capable, even with the limited statistics normally obtained in cosmic ray experiments, of determining whether local isotopic abundance distributions originate in a source which is drastically different from that which produced the solar system material. However, it is possible that differences between the cosmic ray sources and a solar-like source may be reasonably subtle, arising, for example, from differences in the state of evolution of the seed material which provides the fuel for a common nucleosynthesis process. If it is necessary to distinguish source differences which are not dramatic, then it will be necessary to significantly improve the statistical accuracy of the cosmic ray measurements and also to obtain more precise values of the nuclear cross sections required for calculating the secondary contributions to the observed fluxes.

In section 3 of this thesis we present a formalism which can be used in certain cases for obtaining isotopic source abundance ratios and their uncertainties. This treatment is based on the "leaky-box model" of cosmic ray propagation (Gloeckler and Jokipii, 1969; Meneguzzi et al. 1971). We use an isotope which is believed to be absent at the cosmic ray sources as a tracer of the production of secondary cosmic rays during propagation.

Measurements of the abundances of this isotope and of two other isotopes of the same element in local interstellar space can then be used to derive the relative abundances of the latter two isotopes at the cosmic ray sources. This type of analysis makes it possible to interpret measurements of the isotopic make-up of a single element in a way which should not be affected by charge-dependent processes which may be involved in the acceleration of the cosmic rays (Cassé et al., 1975a).

We consider in detail the interpretation of the isotopic composition of the elements O, Ne, S, Ar and Ca. These elements should provide significant astrophysical information. In particular, they should make possible the determination of the neutron enrichment of the cosmic ray sources and the state of evolution of the seed material which has been processed by these sources.

For the case of a solar-like cosmic ray source, we evaluate the contributions of uncertainties in a variety of parameters--local isotopic abundances, composition of parent species, nuclear cross sections and spectral shapes--to the uncertainty in the calculated source abundance ratios. In this way we identify dominant sources of uncertainty. We find that uncertainties in the interpretation of isotope measurements obtained with

instruments now being developed and flown should be dominated by two sources of error: 1) by statistical errors in the measured isotopic abundances and 2) by uncertainties in the fragmentation cross sections necessary for evaluating the secondary contributions to the observed fluxes.

We then narrow our consideration to these two sources of error and evaluate, for a wider range of observed flux ratios, the relative uncertainties which they will produce in the derived source abundance ratios. These results are obtained using typical estimates of the counting statistics and cross section errors which can presently be achieved. However, the uncertainties which we obtain can easily be scaled for other conditions. The details and limitations of such scaling are also examined.

We have applied our uncertainty estimates to the problem of determining the extent to which statistical and cross section errors must be reduced in order to distinguish between cosmic ray production in a solar-like cosmic ray source and production in various non-solar environments. In particular, we derive the number of cosmic ray events of the elements S and Ca and the level of uncertainty in the fragmentation cross sections which must be achieved in order to distinguish various levels of

neutron enrichment over a solar-like environment. This treatment is based on a model for the production of the elements S through Ca in an explosive oxygen burning process, as presented by Woosley et al. (1973). We find that present uncertainty levels should permit one to distinguish a source environment enriched in neutrons by a factor of  $\approx 3$  over the solar composition by using measurements of the isotopic composition of cosmic ray sulfur. In the case of the calcium isotopes, it appears that reduction of the important uncertainties will be required even to distinguish a solar-like source from a source having as much as a factor of 5 enhancement of neutron excess over the solar value.

Finally, we make estimates of the magnitude of the corrections which must be made for solar modulation effects in order to apply this formalism to measurements made in the vicinity of the earth.

## 2. INSTRUMENTATION

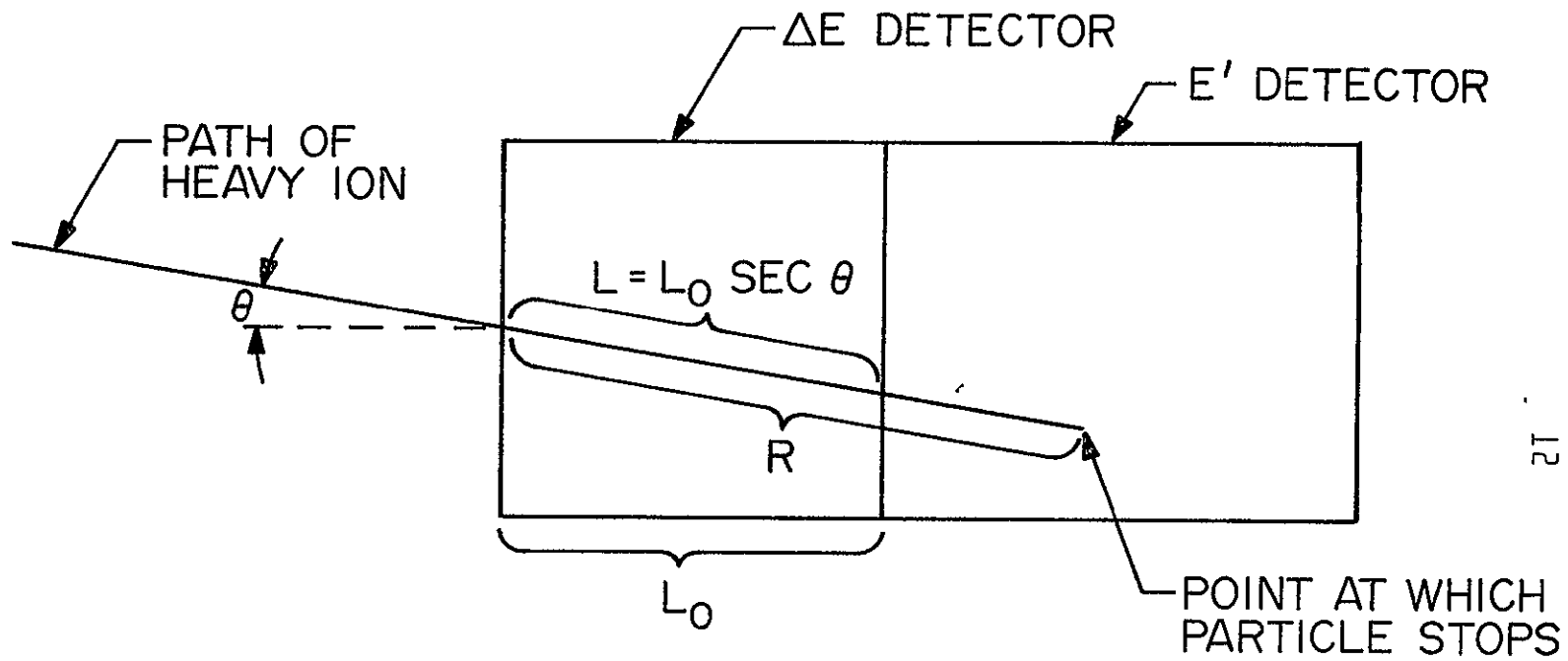
### 2.1 Measurement Technique

The HEIST instrument is designed to determine the mass of cosmic ray nuclei impinging upon it by means of an energy-loss - residual energy measurement. The basic detector geometry is illustrated in figure 1. The energy loss in the first detector is referred to as  $\Delta E$  and the energy deposited in the second detector is referred to as  $E'$ . The measurement relies upon the fact that while the specific ionization of a charged particle depends only on its charge and its velocity (or equivalently its energy per nucleon), particles of mass numbers  $A$  and  $A+1$  that have the same energy per nucleon will have total kinetic energies with a relative difference of  $1/A$ . This difference is less than 2% for the isotopes of nickel, the heaviest nuclei which we are trying to identify.

As a charged heavy particle passes through matter it loses energy predominantly by means of collisions with atomic electrons in the medium. In the energy range of interest here,  $\sim 1-1000$  MeV/nuc, the specific ionization is given by (Barkas and Berger, 1964; Janni, 1966)

FIGURE 1

Schematic illustration of geometry for  
 $\Delta E-E'$  measurement of particle mass.



$$\frac{1}{\rho} \frac{dE}{dx} = 0.307 \text{ cm}^2/\text{g} \frac{Z^2}{\beta^2} \frac{Z}{A} \quad (1)$$

$$\times \left\{ \ln \left[ \frac{2 m c^2 \beta^2}{I (1-\beta^2) \sqrt{1 + \frac{\gamma}{M} \frac{m}{m_p} + \frac{1}{M^2} \left(\frac{m}{m_p}\right)^2}} \right] - \beta^2 - \frac{2}{Z} \sum_i C_i - \frac{\Delta}{2} \right\}$$

In this expression,

$Z$  is the particle's charge in units of the proton charge,  $1.602 \times 10^{-19}$  Coulombs,

$M$  is the particle's mass in units of the proton mass,  $m_p = 938.28 \text{ MeV}/c^2$ ,

$\rho$  is the density ( $\text{g}/\text{cm}^3$ ) of the absorber,

$Z$  is the atomic number of the absorber,

$A$  is the atomic weight of the absorber,

$I$  is the ionization potential of the absorber,

$m$  is the electron mass,  $0.511 \text{ MeV}/c^2$ ,

$\beta$  is the velocity of the charged particle in units of the velocity of light,  $c = 3.00 \times 10^{10} \text{ cm}/\text{sec}$ ,

$\gamma$  is the Lorentz factor,  $\gamma = \frac{1}{\sqrt{1-\beta^2}}$ ,

$-\frac{2}{Z} \sum_i C_i$  is a correction for the fact that the electrons of the medium are bound in atomic shells,

$-\frac{\Delta}{2}$  is a polarization correction which accounts for the fact that the presence of the heavy ion distorts the shape of the electron

ORIGINAL PAGE IS  
OF POOR QUALITY

cloud of near-by atoms in such a way as to partially shield these electrons.

The polarization and shell corrections are small for the range of energies of interest and will be neglected below. In addition, it should be noted that if the square root in the logarithm is neglected (it varies by  $\sim 0.1\%$  from unity for protons at  $1$  GeV), then equation 1 can be written in the form:

$$\frac{1}{\rho} \frac{dE}{dx} = Z^2 S\left(\frac{E}{M}\right).$$

Here the function  $s(E/M)$  is the specific ionization (or mean rate of energy loss per unit of matter traversed) of a proton in the material of interest, and is expressed in  $\text{MeV}/(\text{g}/\text{cm}^2)$ . The mean range of a particle is obtained from the integral:

$$R_{Z,M}\left(\frac{E}{M}\right) = \int_0^E \frac{dE}{\left(\frac{dE}{dx}\right)} = \int_0^E \frac{1}{\rho Z^2} \frac{dE}{S\left(\frac{E}{M}\right)} = \frac{1}{\rho} \frac{M}{Z^2} \int_0^{\frac{E}{M}} \frac{d\left(\frac{E}{M}\right)}{S\left(\frac{E}{M}\right)}$$

$$R_{Z,M}\left(\frac{E}{M}\right) = \frac{M}{Z^2} R_p\left(\frac{E}{M}\right) \quad (2)$$

Here  $R_p(E/M) \cong R_{H^1}(E/M)$  is the range of a proton of energy  $E/M$ . Numerous tabulations of  $R_p$  vs.  $E/M$  are available (Barkas and Berger, 1964; Janni, 1966; Northcliffe and Schilling, 1970).

The above discussion assumes that the charge,  $Z$ , of the ion does not change as the particle slows down. However when the ion slows to a point where its velocity is comparable to the velocity of atomic electrons in their orbits, it becomes possible for the ion to pick up atomic electrons thereby altering  $Z$ . For  $Z=28$  this occurs for energies in the range  $E/M \lesssim 10$  MeV/nuc (Northcliffe and Schilling, 1970). This effect, although significant enough to be considered in the present measurement, will for the sake of simplicity be neglected in the following discussion.

The function  $R_{z,M}(E/M)$  can be approximated with reasonable accuracy by a power law in  $E/M$  over  $\sim 3$  decades variation of  $E/M$ . We can write

$$R_{z,M}\left(\frac{E}{M}\right) = \frac{kM}{Z^2} \left(\frac{E}{M}\right)^a \quad (2')$$

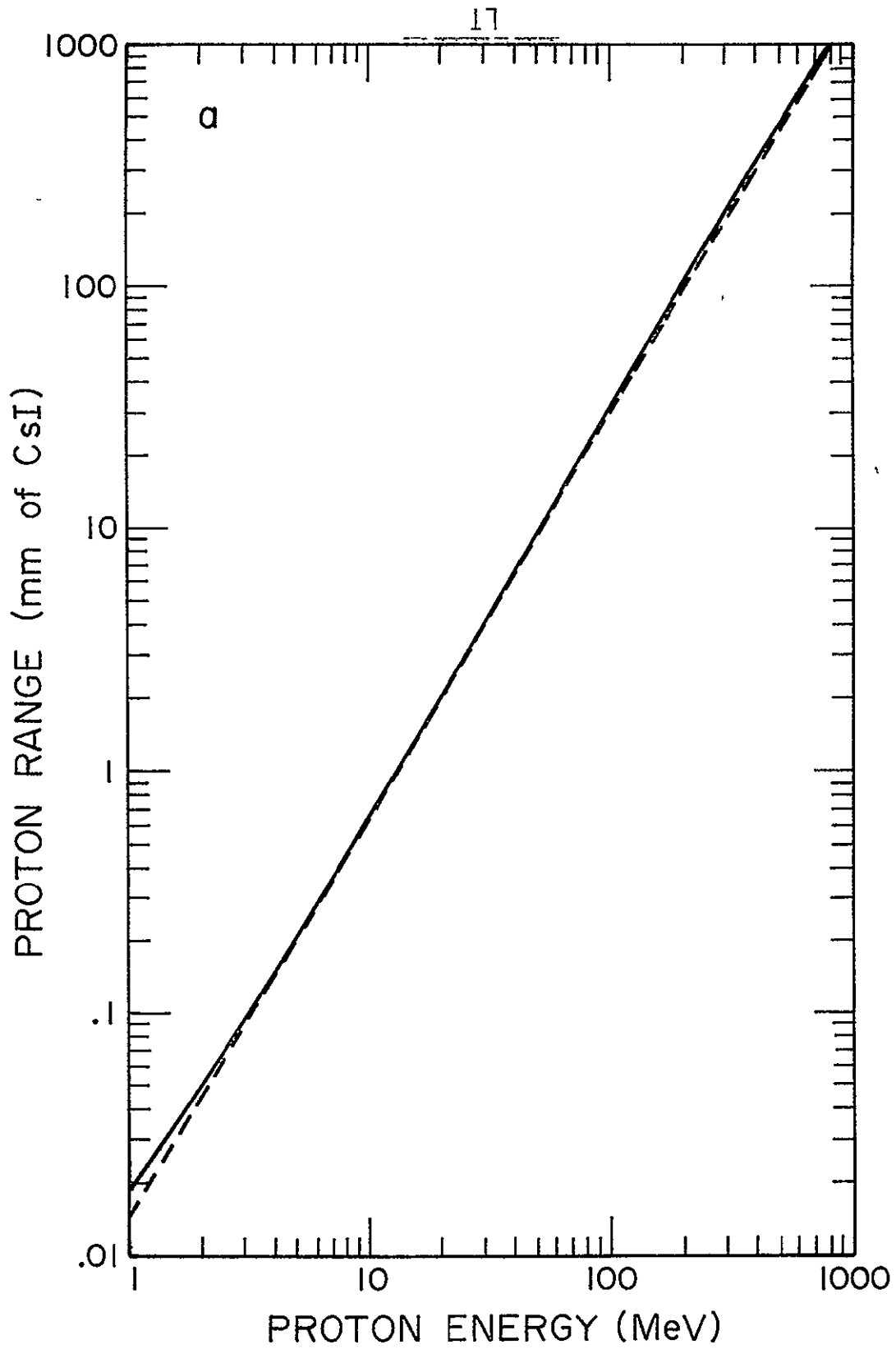
where  $k=.0142$  mm of CsI and  $a=1.664$ . Figure 2a shows the exact form of  $R_p(E/M)$  as well as this power law approximation. Figure 2b shows the fractional difference of these two quantities. By noting that the particle's range and energy after passing through a layer of thickness  $L$  are  $R_{z,M}(E/M)-L$  and  $E'$  respectively, we can write:

FIGURE 2

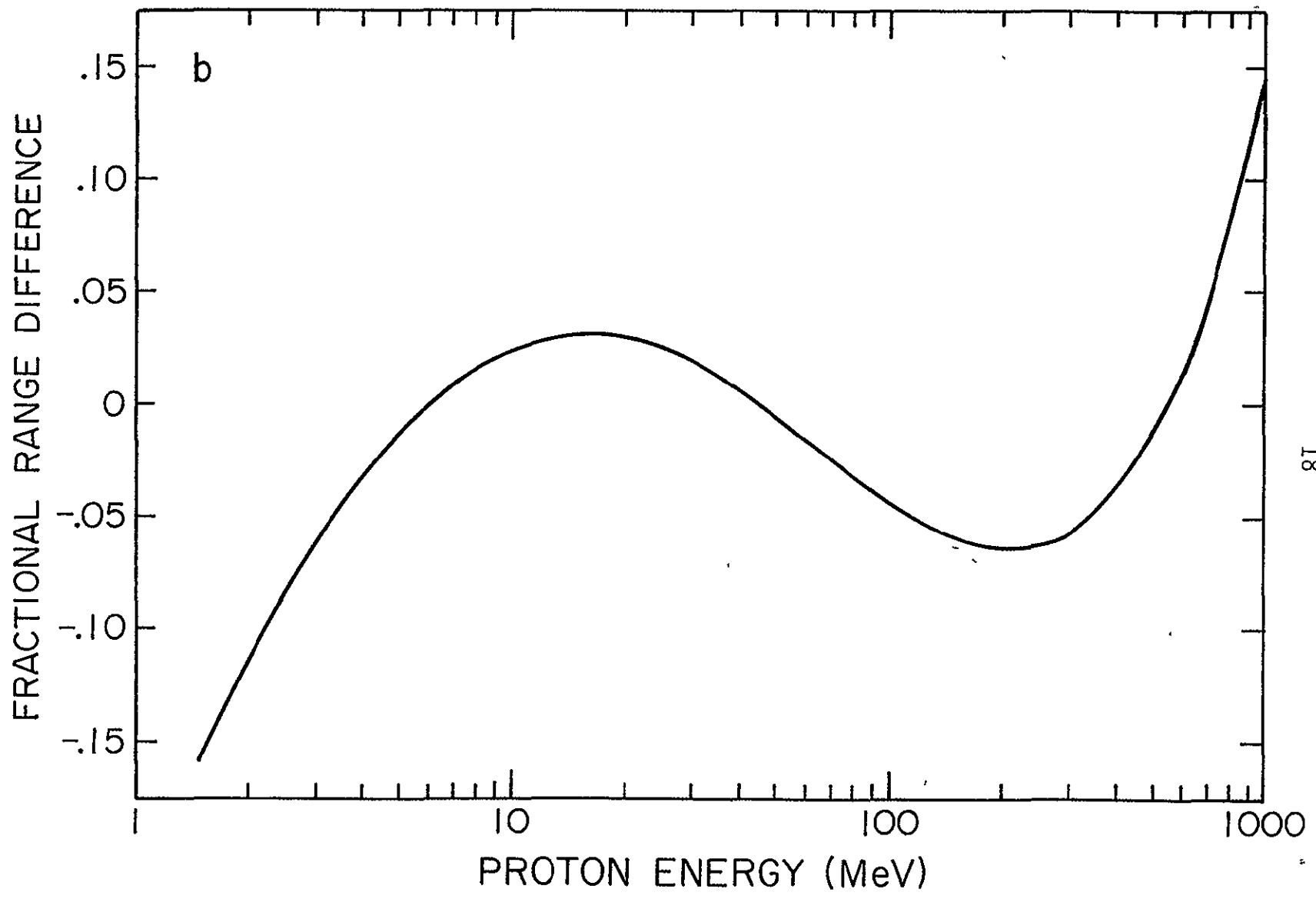
Proton range in Csl vs. particle energy.

a) Solid curve is exact relation as given by Janni (1966), dashed curve is power law approximation.

b) Fractional difference between exact relation and power law approximation.



ORIGINAL PAGE IS  
OF POOR QUALITY



$$R_{z,M}\left(\frac{E}{M}\right) - L = \frac{M}{Z^2} R_p\left(\frac{E'}{M}\right), \quad (3)$$

or

$$R_{z,M}\left(\frac{E}{M}\right) - L = \frac{kM}{Z^2} \left(\frac{E'}{M}\right)^\alpha. \quad (3')$$

By eliminating  $R_{z,M}(E/M)$  between 2 and 3 we obtain an implicit relation for  $M$  in terms of  $Z$  and the measurable quantities  $L$ ,  $\Delta E$  and  $E'$ :

$$0 = f_z(M, \Delta E, E', L) = R_p\left(\frac{\Delta E + E'}{M}\right) - R_p\left(\frac{E'}{M}\right) - \frac{Z^2}{M} L \quad (4)$$

In the power law approximation we can explicitly solve for  $M$ :

$$M = \frac{k}{Z^2 L} (E^\alpha - E'^\alpha)^{\frac{1}{\alpha-1}}. \quad (4')$$

In what follows we shall assume that the particle's charge,  $Z$ , is known. This is reasonable since, due to the discrete nature of the nuclear charge and mass, both of these quantities can be determined from measurements of  $\Delta E$  and  $E'$ . Experiments employing the  $\Delta E$ - $E'$  technique have already succeeded in resolving individual elements with  $Z \leq 28$  (see, for example, the review by Garcia-Munoz, 1973).

The uncertainties in the masses which we will derive can be expressed as

$$\begin{aligned} \sigma_M^2 = & \left( \frac{\partial M}{\partial \Delta E} \right)_{E,L}^2 \sigma_{\Delta E(\text{Landau})}^2 + \left( \frac{\partial M}{\partial \Delta E} \right)_{E',L}^2 \sigma_{\Delta E(\text{meas})}^2 \\ & + \left( \frac{\partial M}{\partial E'} \right)_{\Delta E,L}^2 \sigma_{E'(\text{meas})}^2 + \left( \frac{\partial M}{\partial L} \right)_{\Delta E,E'}^2 \sigma_L^2. \end{aligned} \quad (5)$$

In this equation,  $\sigma_{\Delta E(\text{Landau})}$  is the uncertainty in the energy loss in the  $\Delta E$  detector due to statistical fluctuations in the ionization energy loss process, and  $\sigma_{\Delta E(\text{meas})}$ ,  $\sigma_{E'(\text{meas})}$  and  $\sigma_L$  are the uncertainties in our measurements of  $\Delta E$ ,  $E'$  and  $L$  respectively. Equation 5 applies only if the various contributions to the mass uncertainty are statistically independent. This condition is not strictly correct for our measurement, but the error made in using it should not be significant. Equation 4 can be used to obtain the required partial derivatives of  $M$  with respect to the measured quantities. Table 1 summarizes these derivatives. The measurement uncertainties will be evaluated in the course of the discussion of the instrument.

This section will discuss our mass resolution requirements and the limits on the mass resolution attainable using the  $\Delta E$ - $E'$  technique. It is possible to plot lines of constant mass,  $M$ , on a  $\Delta E$  vs.  $E'$  graph.

TABLE 1

Partial Derivatives Used for Evaluating Mass Resolution

Quantity	Exact Expression	Power Law Approximation
$\left(\frac{\partial M}{\partial L}\right)_{\Delta E, E'}$	$-\left[\frac{(E/M)}{z^2 s(E/M)} - \frac{(E'/M)}{z^2 s(E'/M)} - \frac{L}{M}\right]^{-1}$	$\frac{-1}{a-1} \frac{M}{L}$
$\left(\frac{\partial M}{\partial \Delta E}\right)_{E', L}$	$\frac{\frac{1}{z^2 s(E/M)}}{\frac{(E/M)}{z^2 s(E/M)} - \frac{(E'/M)}{z^2 s(E'/M)} - \frac{L}{M}}$	$\frac{a}{a-1} \frac{M R}{E L}$
$\left(\frac{\partial M}{\partial E'}\right)_{\Delta E, L}$	$\frac{\frac{1}{z^2 s(E/M)} - \frac{1}{z^2 s(E'/M)}}{\frac{(E/M)}{z^2 s(E/M)} - \frac{(E'/M)}{z^2 s(E'/M)} - \frac{L}{M}}$	$\frac{a}{a-1} \frac{M R}{E' L} \left[ \left(1 - \frac{L}{R}\right)^{\frac{1}{a}} - \left(1 - \frac{L}{R}\right) \right]$
$\left(\frac{\partial M}{\partial \Delta E}\right)_{E, L}$	$\frac{\frac{1}{z^2 s(E'/M)}}{\frac{(E/M)}{z^2 s(E/M)} - \frac{(E'/M)}{z^2 s(E'/M)} - \frac{L}{M}}$	$\frac{a}{a-1} \frac{M R}{E L} \left(1 - \frac{L}{R}\right)^{1 - \frac{1}{a}}$

ORIGINAL PAGE IS  
OF POOR QUALITY

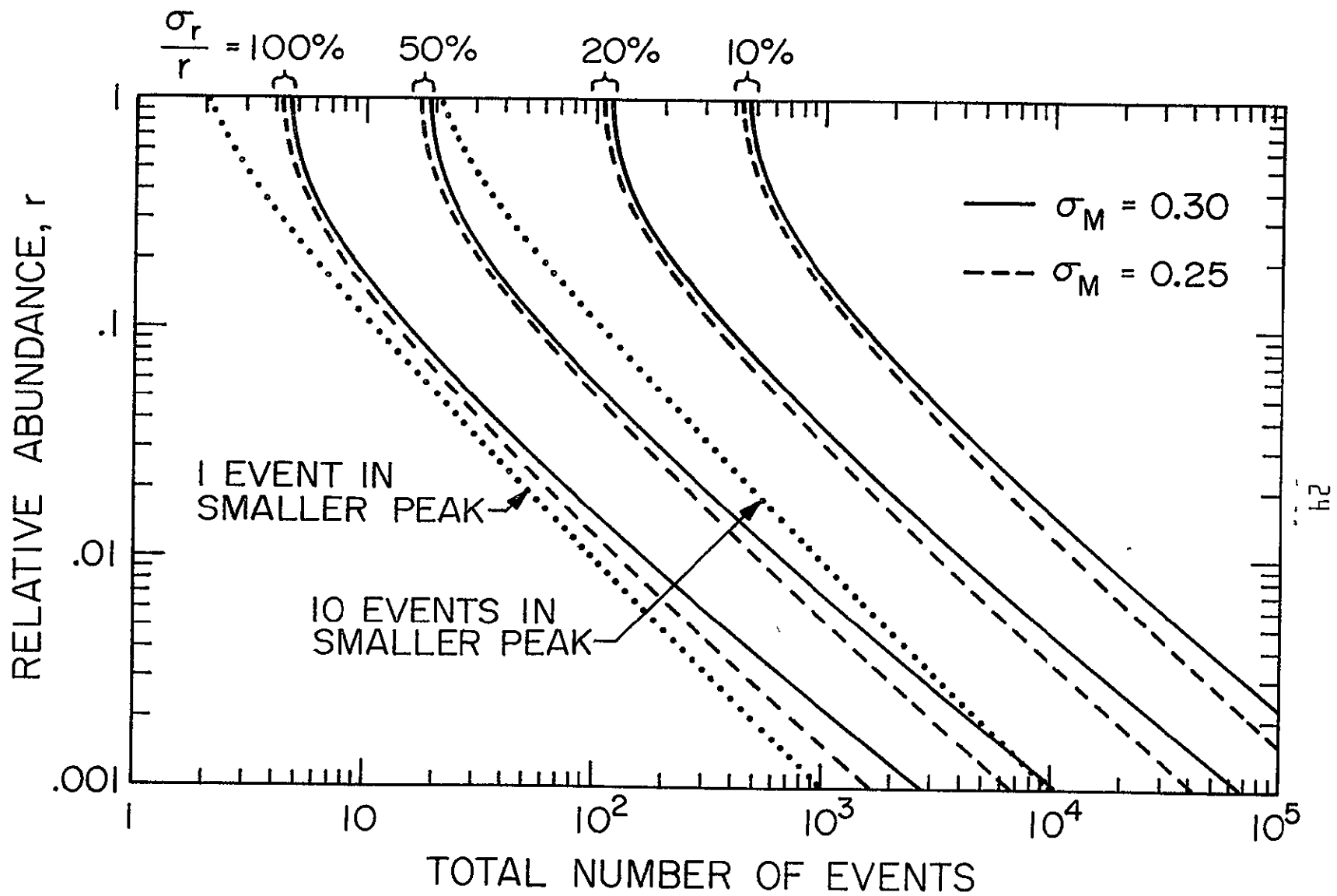
This formal procedure can be carried out even for non-integral values of  $M$ . By dividing the  $\Delta E-E'$  plane in this way the events corresponding to a particular element can be binned to form a mass histogram. In our discussion of our ability to obtain isotope ratios from such a histogram we will treat the simple case in which only two isotopes have non-negligible abundances. If we know that the mass peaks have Gaussian shape and if we accurately know the mass resolution,  $\sigma_M$ , of the instrument then we can use the method of least squares to obtain the abundance ratio of these two species. In addition, the uncertainty in this ratio can be obtained from the curvature of the  $\chi^2$  at its minimum (Bevington, 1969; Mathews and Walker, 1970). The details of this procedure are discussed in appendix A.

Figure 3 shows as a function of the abundance ratio,  $r$ , the number of events required to obtain relative uncertainties of 10%, 20%, 50% and 100% in our estimate of this ratio. The number of counts is weakly dependent on the mass resolution as well. The solid curves in the figure are calculated for  $\sigma_M = 0.3$  units and the dashed curves are calculated for  $\sigma_M = 0.25$  units (where the separation between the centers of the two Gaussian distributions is defined as one unit). In addition, a pair of dotted curves are included in the figure to

FIGURE 3

Number of events required to determine abundance ratios with uncertainties of 10%, 20%, 50% and 100%. Curves are shown for mass resolutions of 0.25 and 0.30 times the mean separation between the distributions. Dotted curves indicate combinations of  $N$  and  $r$  which yield 1 and 10 events of the less abundant species.

ORIGINAL PAGE IS  
OF POOR QUALITY



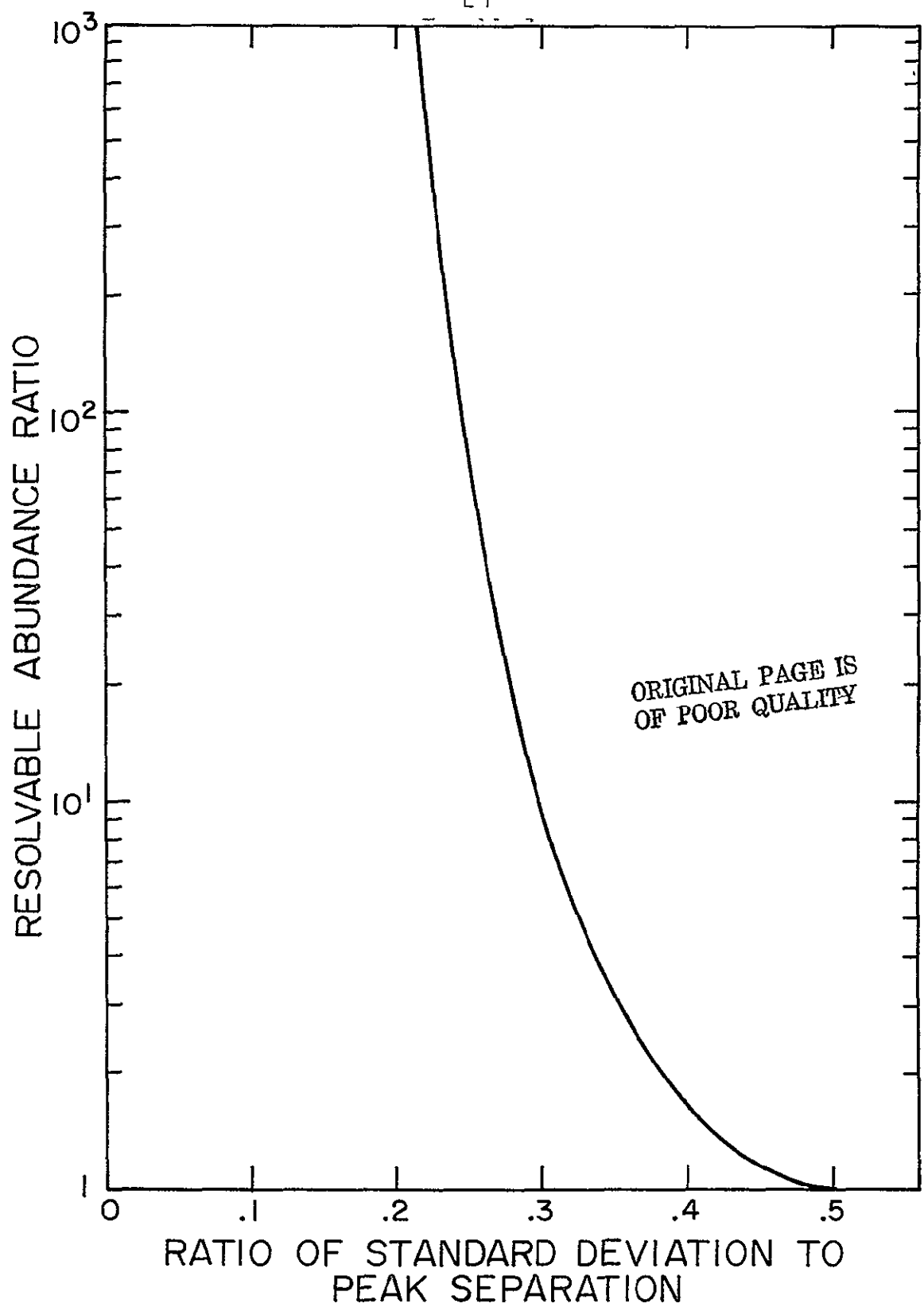
indicate those combinations of  $r$  and  $N$  which yield 1 and 10 counts in the peak having the smaller abundance. It is not expected that this type of calculation of  $\sigma_r$  will be reliable when there are  $\lesssim 10$  counts in the less abundant peak for reasons mentioned in appendix A.

It should be noted that although distributions of known shape can be separated by fitting techniques even when they have a large degree of overlap (as indicated by the weak dependence of  $\sigma_r$  on  $\sigma_M$  in figure 3), it is important that we be able to achieve a reasonable degree of separation. This is because this measurement is subject to various systematic errors which will tend to produce non-Gaussian distributions whose precise shape is difficult to determine. As an estimate of the required mass resolution we have calculated the mass resolution for which an inflection point is obtained between two Gaussian distributions whose means are separated by one unit, as a function of the ratio of the number of counts in the two distributions (Stone, 1973; Hagen, 1975). The details of this calculation are outlined in appendix A and the results are summarized in figure 4.

If the iron produced in the cosmic ray sources consists of a single isotope,  $A$ , one expects a ratio  $N(A-1)/N(A) \lesssim 0.1$  at earth due to spallation reactions in

FIGURE 4

Relative abundance in two Gaussian distributions for which an inflection point is obtained as a function of the ratio of standard deviation to peak separation.



the interstellar medium. Thus we need to achieve a mass resolution of  $\lesssim 0.30$  AMU. There are, however, instances where the mass peaks which we are attempting to resolve are separated by two atomic mass units. For a given element nuclear pairing effects (Evans, 1955; Preston, 1962) enhance the stability of nuclei with even numbers of neutrons ( $N$ ). Hence, there are cases where an odd- $N$  isotope lies between two isotopes of interest, and this isotope can be neglected either because it is unstable (e.g.,  $^{39}\text{Ar}$ ) or because its production is suppressed in the astrophysical environment of interest and it is not produced in significant amounts by spallation reactions during propagation (e.g.,  $^{41}\text{Ca}$ ). In such cases we can resolve the two even- $N$  nuclei with a mass resolution as large as  $\sim 0.5$  AMU.

The fundamental limit on the mass resolution attainable by the  $\Delta E-E'$  technique is due to the statistical nature of the ionization energy loss process. This results in Landau fluctuations--a distribution of possible  $\Delta E$  values for a monoenergetic beam of identical particles incident on the detector. The energy losses of interest here are sufficiently large in comparison with the energy that the particle can transfer in a single collision so that the Landau distribution is accurately approximated by its Gaussian limit (Seltzer and Berger,

1964; Rossi, 1952),

$$\sigma_{\Delta E(\text{Landau})}^2 = (0.396 \text{ MeV})^2 \frac{Z}{A} \frac{1}{2} (\gamma^2 + 1) \rho L,$$

where

$L$  = thickness of  $\Delta E$  detector (cm),

$\gamma = \frac{1}{\sqrt{1-\beta^2}}$  (Lorentz factor),

$\rho$  = density of the detector material ( $\text{g}/\text{cm}^3$ ),

$Z$  = mean atomic number of the detector material,

$A$  = mean atomic weight of the detector material.

This expression applies only for  $L$  sufficiently small so that the particle's specific ionization does not change significantly as it traverses the  $\Delta E$  detector.

The  $\Delta E$  detectors of interest here are thick enough so that a correction must be made for the deceleration of the particle. We introduce a "deceleration factor",  $D$ , in the above expression for  $\sigma_{\Delta E(\text{Landau})}$  to make this correction (Hurford, 1974).  $D$  is always greater than unity, since an energy loss larger (smaller) than the mean energy loss early in the  $\Delta E$  detector will result in a particle of lower (higher) than average energy and hence of higher (lower) than average specific ionization. This particle will also tend to have a greater (smaller) than average

energy loss later in the  $\Delta E$  detector.  $D$  is a function of  $L/R$  (the ratio of the  $\Delta E$  detector thickness to the particle's range) which increases from 1 at  $L/R=0$  to  $\sim 3$  for  $L/R \sim 0.95$ . The deceleration factor which we employ differs slightly from that used by Hurford since we include the velocity dependence of  $\sigma_{\Delta E(\text{Landau})}$  in obtaining this correction.

So far the thickness,  $L$ , of the  $\Delta E$  detector has not been specified. The effect which Landau fluctuations and energy measurement uncertainties can have on the mass resolution of the instrument can be minimized by an appropriate choice of this thickness. Figure 5 illustrates this point. The long  $45^\circ$  line in figure 5a is a line of constant energy, 1550 MeV. The point along this line at which a given particle falls depends on the ratio,  $L/R$ , of the particle's path-length in the  $\Delta E$  detector to its range. The pairs of line segments intersecting the constant energy line are constant mass lines corresponding to the isotopes  $^9\text{Be}$  and  $^{10}\text{Be}$  as they would appear for various choices of the thickness  $L_0$ . The notable features of this graph are 1) the separation between neighboring isotopes decreases as  $E'$  approaches  $E$  (or equivalently as  $L$  approaches 0) and 2) for  $E' \sim 0$  the constant mass lines become parallel to the constant energy line while for  $E' \sim E$  they become parallel to lines of constant  $\Delta E$ .

FIGURE 5

Example illustrating the effects of various choices of  $\Delta E$  detector thickness,  $L$ , for the case of Be isotopes at a total kinetic energy of 1550 MeV ( ${}^9\text{Be}$  range is 44.8 mm of CsI;  ${}^{10}\text{Be}$  range is 41.7 mm of CsI).

a) Constant mass lines for the isotopes  ${}^9\text{Be}$  and  ${}^{10}\text{Be}$  for several values of the  $\Delta E$  detector thickness. Separation between isotope tracks is greatest when  $L$  is a large fraction of the particle's range.

b) Energy changes required to produce a change of 1 AMU in the calculated mass. The curves are labeled as follows:

$\Delta E$  -Change in  $\Delta E$  with  $E'$  constant.

$E'$  -Change in  $E'$  with  $\Delta E$  constant.

Landau -Change in  $\Delta E$  with  $\Delta E+E'$  constant.

Also shown is the uncertainty in  $\Delta E$  due to Landau fluctuations.



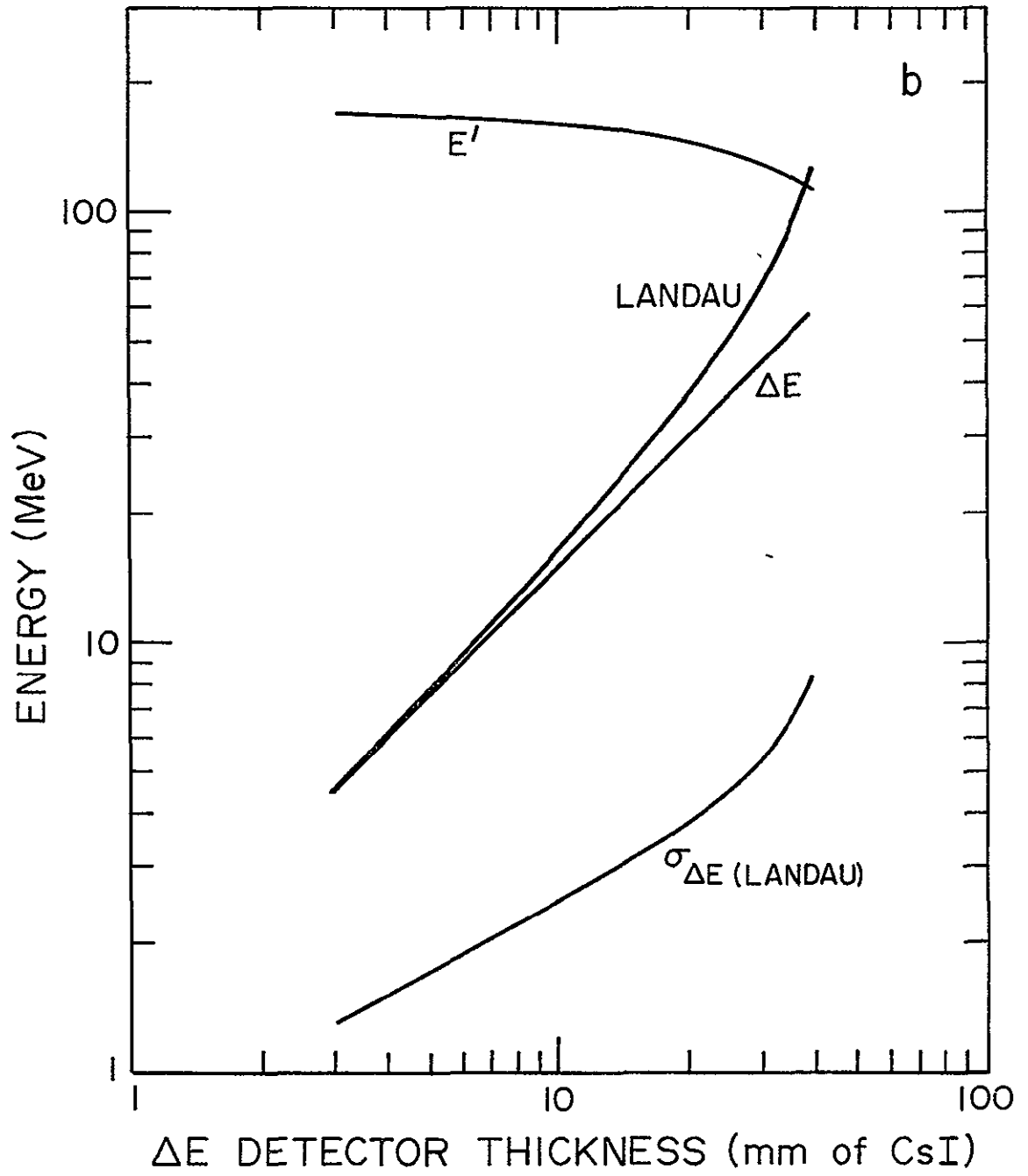


Figure 5b shows, as a function of  $L$ , the amounts which  $\Delta E$  and  $E'$  must separately be altered (as will be caused by errors in measuring these quantities) in order to alter the mass which we would calculate for the event by one mass unit. Also shown is the amount which  $\Delta E$  must be varied with  $\Delta E + E'$  constant (as will be caused by Landau fluctuations) to produce a one mass unit change. In addition the figure shows the rms change in  $\Delta E$  (and  $E'$ ) that will be caused by Landau fluctuations in the  $\Delta E$  detector. It can be seen that the increasing separation of the mass tracks adequately compensates for the increasing Landau fluctuations as we increase the thickness of the  $\Delta E$  detector.

In order to keep  $\Delta E \sim E$  we utilize a stack of eight separate scintillation counters for energy measurements. The scintillator in which a particle stops is treated as the  $E'$  detector and the energy losses in all the earlier detectors are summed to form the  $\Delta E$  measurement. The thicknesses of the scintillators are chosen so that we obtain  $L/R \approx 0.7$  in all but the first few detectors. Table 2 summarizes the thicknesses of the CsI(Tl) scintillators.

Figure 6 shows, for selected isotopes, the limiting mass resolution attainable with the HEIST instrument. It is assumed that for a particle stopping in  $D_n$  the energy

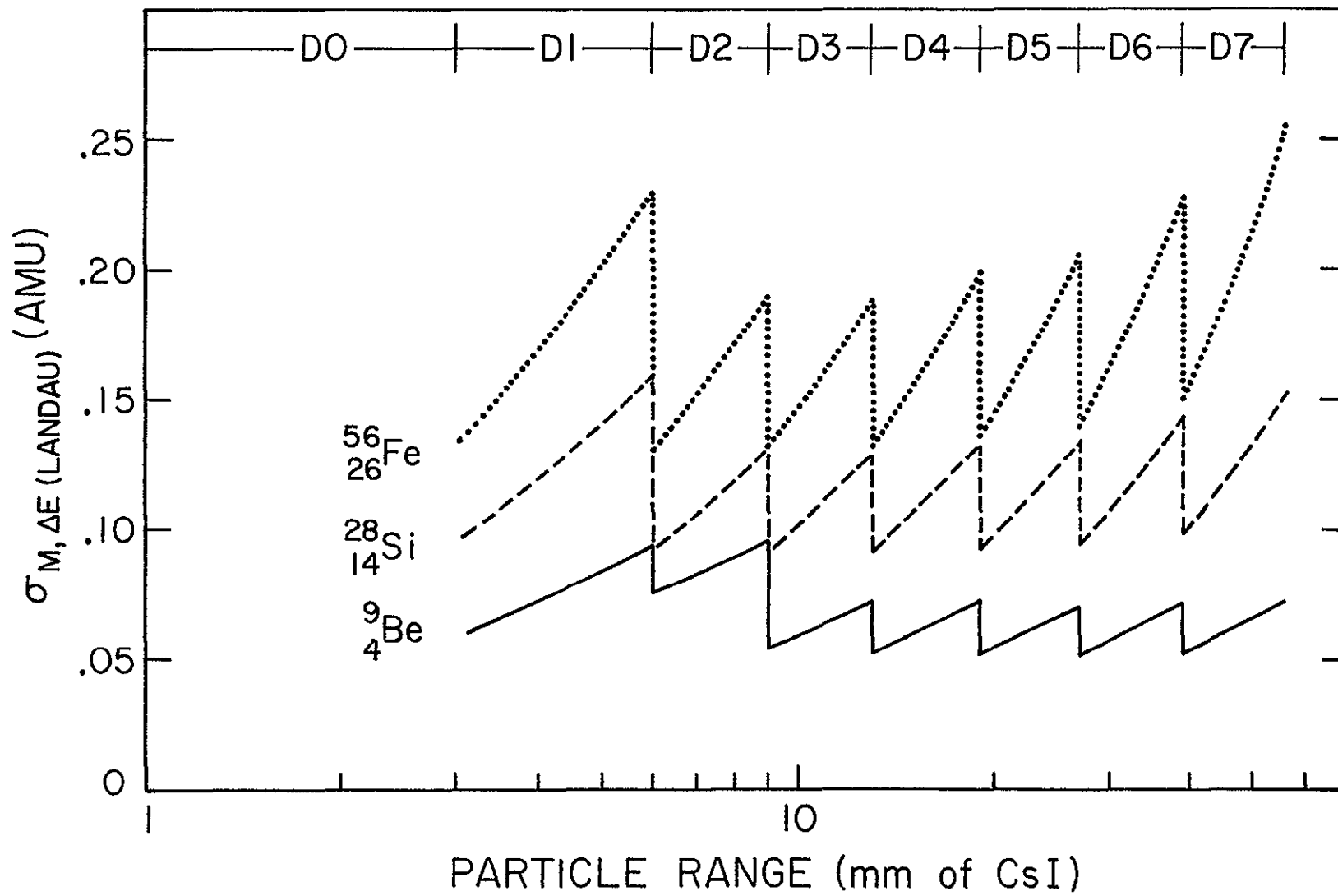
TABLE 2

HEIST Detector Thicknesses

<u>Detector</u>	<u>Nominal Thickness</u>		<u>Sum Thru This Detector</u>		<u>Maximum L/R</u>
	<u>mm</u>	<u>g/cm<sup>2</sup></u>	<u>mm</u>	<u>g/cm<sup>2</sup></u>	
D0	3	1.4	3	1.4	----
D1	3	1.4	6	2.7	0.50
D2	3	1.4	9	4.1	0.67
D3	4	1.8	13	5.9	0.69
D4	6	2.7	19	8.6	0.68
D5	8	3.6	27	12.2	0.70
D6	12	5.4	39	17.6	0.69
D7	17	7.7	56	25.3	0.70

FIGURE b

Contribution of Landau fluctuations to the uncertainty in measured masses for normally incident particles. All detectors prior to the detector in which the particle stops are summed to form the  $\Delta E$  measurement.



losses in  $D_0$  through  $D_{n-1}$  will be added to form the  $\Delta E$  measurement. The sawtooth pattern is primarily due to the variation of the L/R ratio as discussed above.

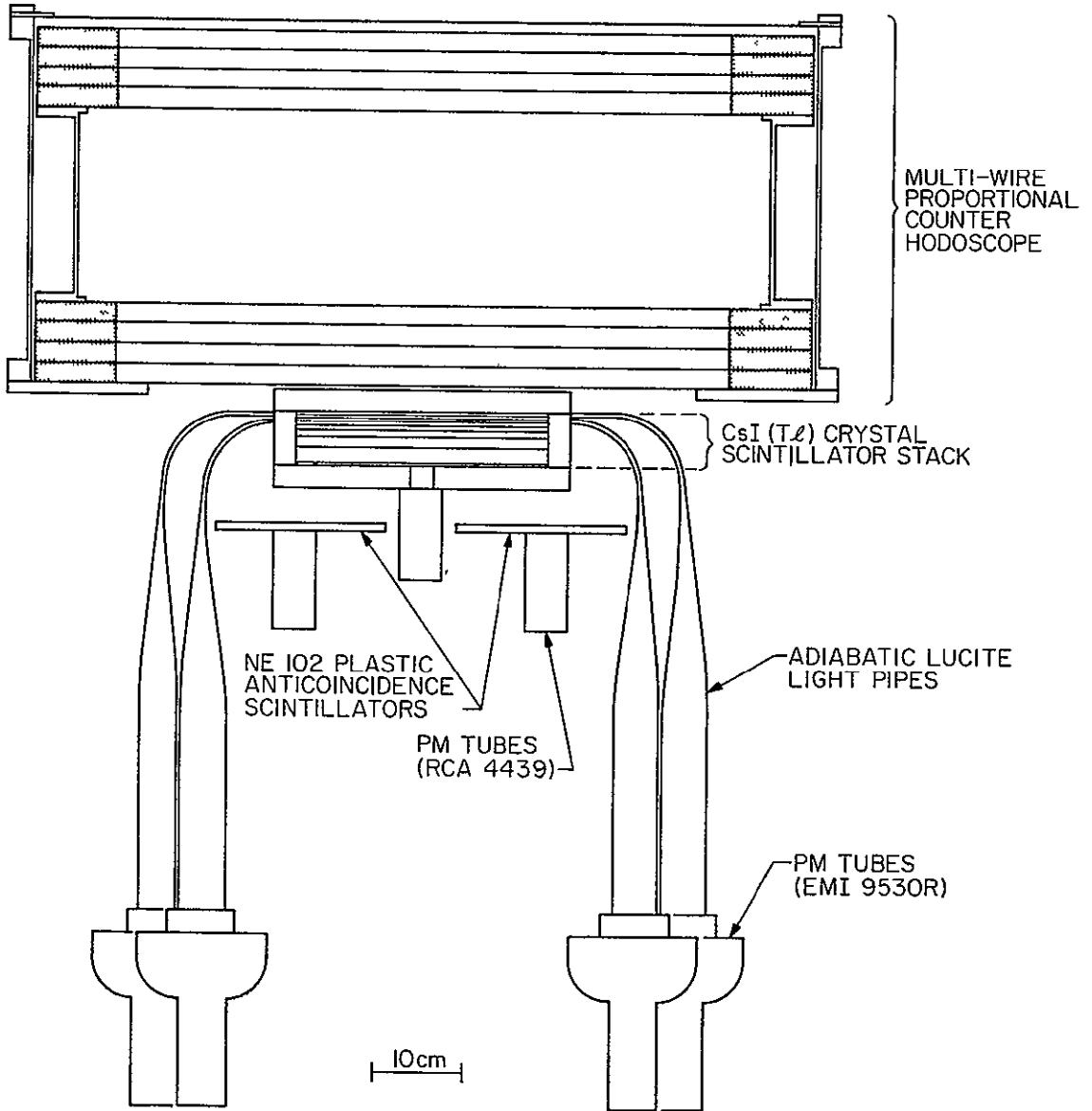
In addition to precise measurements of  $\Delta E$  and  $E'$ , it is necessary to precisely measure the trajectories of the cosmic ray particles. Since a given fractional uncertainty in L, the particle's path-length in the  $\Delta E$  detector, results in the same fractional uncertainty in the calculated mass (see table 1) and since L is proportional to the secant of the particle's angle of incidence,  $\theta$ , it is essential to precisely measure  $\theta$ . Also, it is important to know the position at which each particle passed through the scintillator stack since corrections must be made for positional variations in the thickness and light collection efficiency of each scintillator. These corrections will be discussed in detail below.

## 2.2 Instrument -- Overall Description

Figure 1 shows a cross sectional view of the HEIST instrument. It consists of two basic parts. On top is a hodoscope consisting of eight multiwire proportional chambers (MWPC's) oriented so that alternate chambers measure x and y coordinates along a particle's trajectory.

FIGURE 1

Cross sectional view of the HEIST instrument. The cross section is taken along a diagonal of the proportional counter hodoscope. The light pipes and attached photomultipliers lie off of this plane and are shown projected onto it.



Beneath the hodoscope is a stack of nine thin, large diameter CsI(Tl) crystal scintillators. The uppermost eight scintillators are used for making precise measurements of a particle's energy losses. Each of these scintillators is coupled to a 130 mm (5") photomultiplier tube by means of an adiabatic lucite light pipe. The ninth scintillator is directly viewed by a 38 mm (1-1/2") photomultiplier and is used to identify particles which did not stop in the upper eight scintillators. In addition, two plastic scintillators located below the crystal stack are used in anticoincidence to reduce the background of wide angle particles that can exit from the side of the crystal stack. Figures 8a and b are schematic views from above and from one edge of the detector stack showing the relative spacing of the various detectors. The various sensors are identified as follows: X1 through X4 are the MWPC's used for measuring the x-coordinates of a particle's trajectory, Y1 through Y4 are the MWPC's used for measuring the corresponding y-coordinates, and D0 through D7 are the CsI(Tl) scintillators used for making energy loss measurements. Table 3 lists the relative positions of the sensors shown in figure 8b.

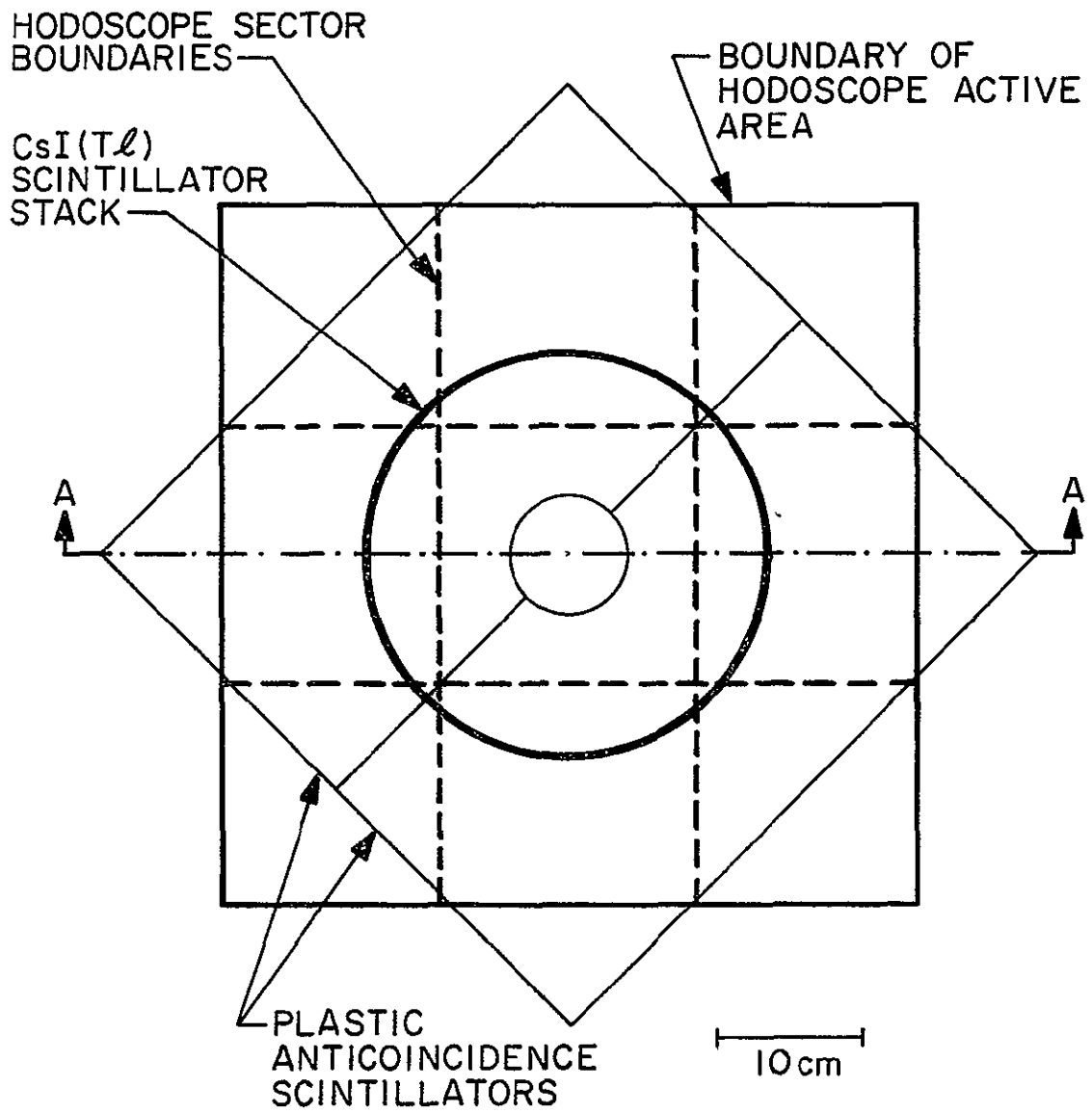
Figure 9 illustrates, for particles with  $M \approx 2Z$ , the intervals of charge and energy over which the HEIST instrument is capable of mass measurements. Two sets of

FIGURE 8

Scale drawings of particle detecting regions of the HEIST instrument.

a) View from above.

b) View taken through section A-A indicated in figure 8a. Note that this view is at  $45^\circ$  to that shown in figure 7.



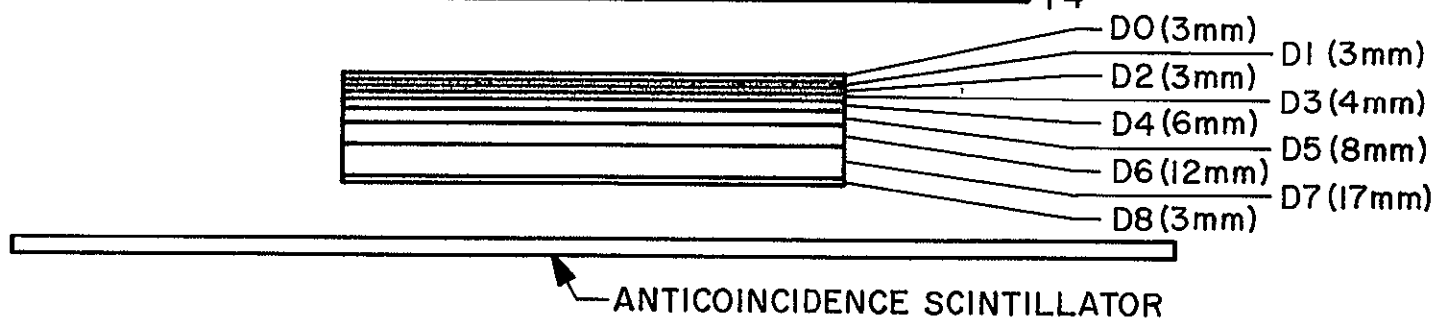
ORIGINAL PAGE IS  
OF POOR QUALITY



b



h



10 cm

TABLE 3

## Positioning of HEIST Sensors

	<u>cm</u>	<u>inches</u>
Bottom of hodoscope base plate*	0	0
Bottom of Y <sub>4</sub> cathode	0.975	2.476
Bottom of X <sub>4</sub> cathode	1.857	4.717
Bottom of Y <sub>3</sub> cathode	2.739	6.957
Bottom of X <sub>3</sub> cathode	3.618	9.190
Bottom of Y <sub>2</sub> cathode	13.024	33.081
Bottom of X <sub>2</sub> cathode	13.907	35.324
Bottom of Y <sub>1</sub> cathode	14.789	37.564
Bottom of X <sub>1</sub> cathode	15.678	39.822
Top of D <sub>0</sub> scintillator	-0.648	-1.646
Top of D <sub>1</sub> scintillator	-0.783	-1.989
Top of D <sub>2</sub> scintillator	-0.918	-2.332
Top of D <sub>3</sub> scintillator	-1.046	-2.657
Top of D <sub>4</sub> scintillator	-1.214	-3.084
Top of D <sub>5</sub> scintillator	-1.453	-3.691
Top of D <sub>6</sub> scintillator	-1.770	-4.496
Top of D <sub>7</sub> scintillator	-2.245	-5.702
Top of D <sub>8</sub> scintillator	-2.916	-7.407

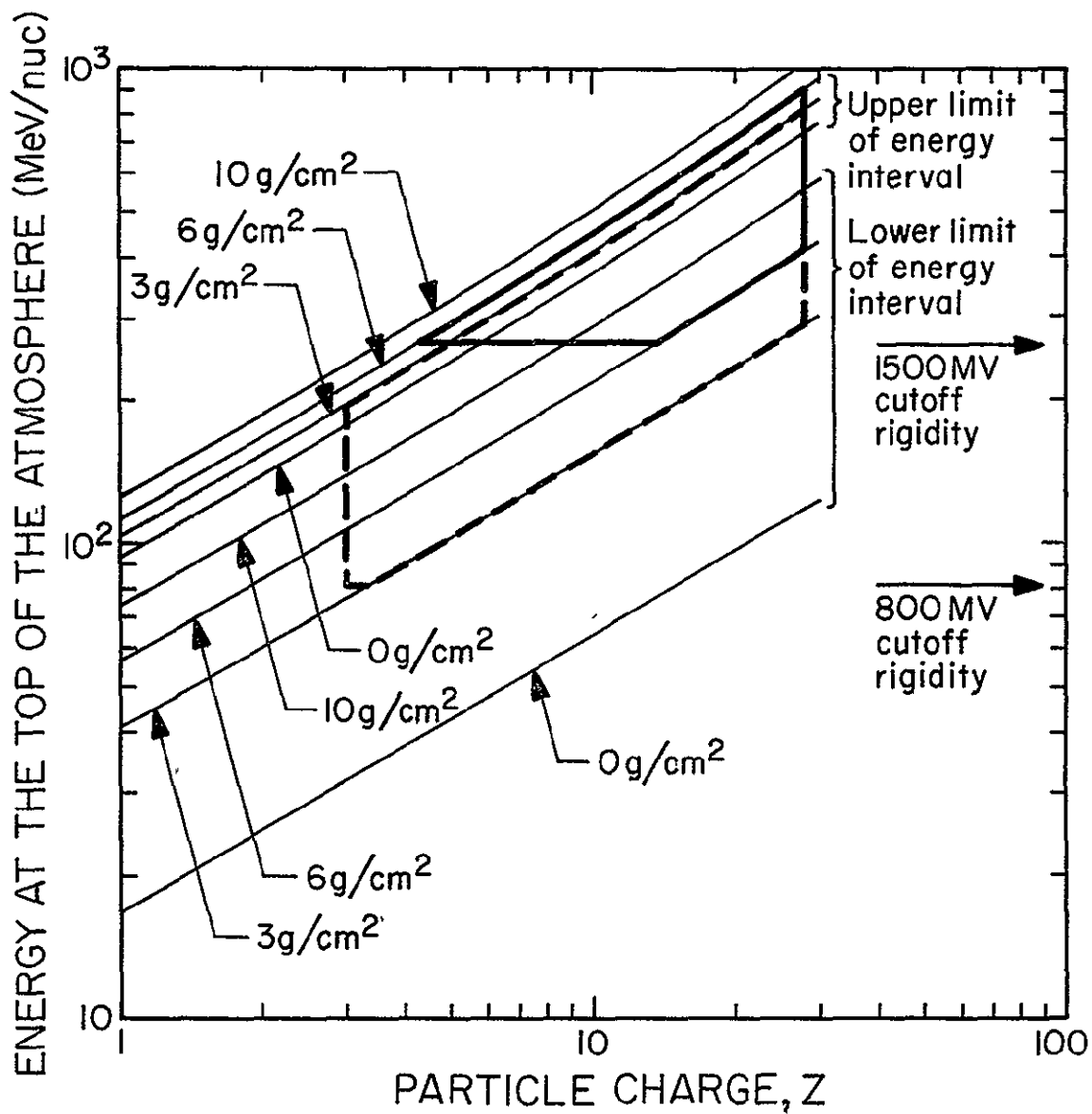
---

\* Reference level.

FIGURE 9

Intervals of charge and energy at the top of the earth's atmosphere which are accessible to the HEIST instrument for normally incident particles. Curves indicating the upper and lower limits of the energy intervals which can be detected are shown for atmospheric depths of 0, 3, 6 and 10 g/cm<sup>2</sup>. Outlined regions correspond to flights at 1500 MV magnetic cutoff and 6 g/cm<sup>2</sup> atmospheric depth (solid box) and at 800 MV cutoff and 3 g/cm<sup>2</sup> depth (dashed box) as discussed in the text. Energies corresponding to magnetic rigidities of 800 and 1500 MV are indicated by arrows for particles with M/Z=2.

ORIGINAL PAGE IS  
OF POOR QUALITY



curves are included. The curves in each set are labeled according to the amount of overlying material (air plus material above the scintillator stack in the gondola). The lower set shows the energy which a normally incident particle must have at the top of the atmosphere in order to just penetrate to the D0-D1 boundary in the scintillator stack. The upper set of curves is for particles which just penetrate to the D7-D8 boundary. For normally incident particles of a given charge the energy interval above the atmosphere from which the HEIST instrument will accumulate stopping particles is simply the interval between the two curves corresponding to the appropriate amount of overlying material. We also indicate the energies which correspond to geomagnetic cutoff rigidities of 800 and 1500 MV. In figure 9 we illustrate charge and energy regions viewed by the HEIST instrument in two cases. The solid box corresponds to a flight at a 1500 MV cutoff with 6 g/cm<sup>2</sup> of residual atmosphere.\* The relatively high magnetic cutoff in this case restricts observations to elements with  $Z \geq 5$  and severely restricts the energy interval obtained for elements with  $Z \lesssim 13$ . The dashed box corresponds to a

---

\* Such a flight was made on 6 June 1977 from Aberdeen, S.D.

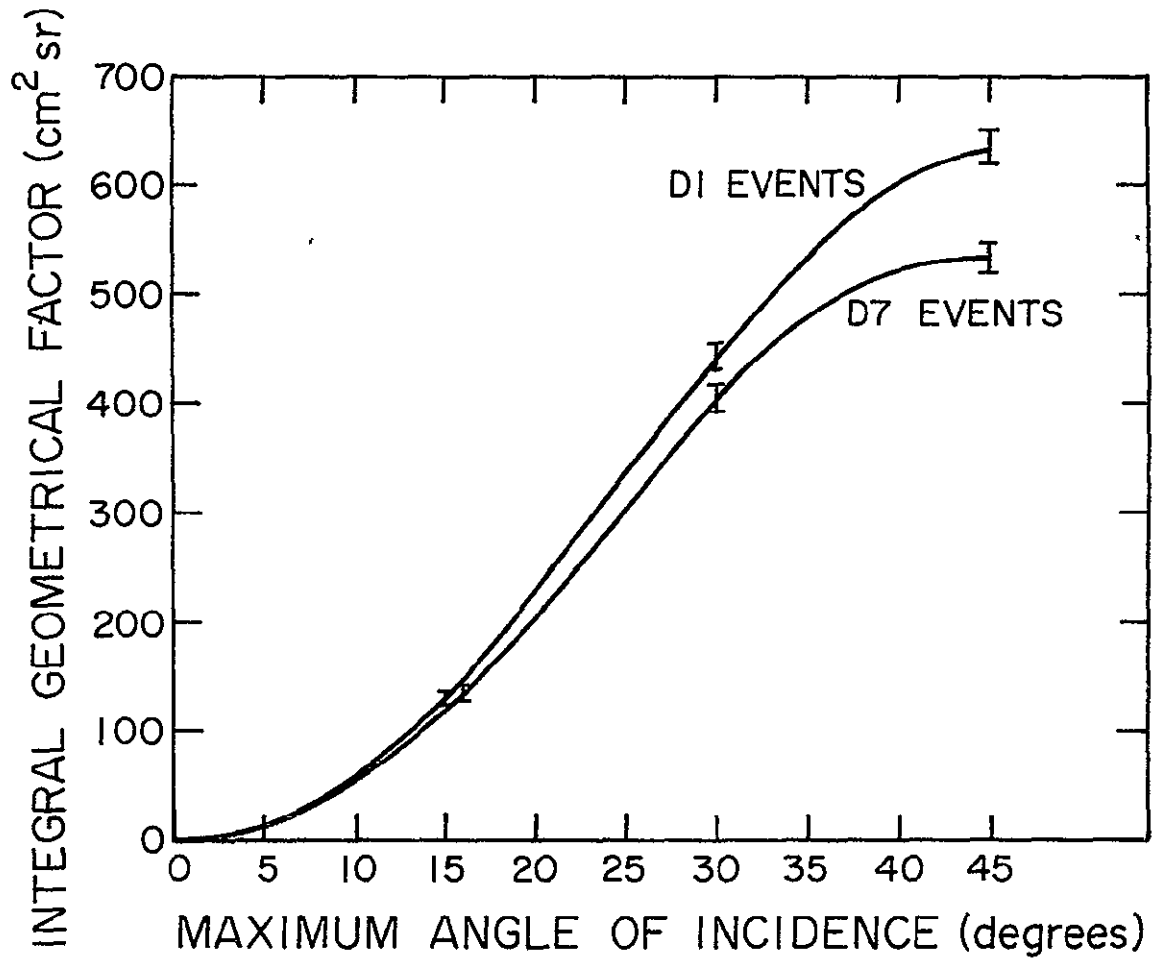
flight with a cutoff rigidity of 800 MV at an atmospheric depth of  $3 \text{ g/cm}^2$ . In this case the cutoff has little effect and elements can be observed all the way down to the instrumental limit of  $Z=3$ . It is clear from figure 9 that it is desirable to fly this instrument at northerly latitudes in order to obtain a geomagnetic cutoff  $\approx 800 \text{ MV}$ .

In normal operation, a stopping particle must trigger at least one x and one y MWPC in both the upper and lower halves of the hodoscope, must trigger two of the first three scintillators and not trigger either the bottom crystal or the plastic anticoincidence counter. Figure 10 shows the integral geometrical factor (geometrical factor at angles less than a specified maximum angle) for accumulating stopping particles in two of the ranges of the instrument as a function of the particles' maximum accepted incidence angle. These geometrical factors are the result of a Monte Carlo calculation (Sullivan, 1971) and the error bars just reflect the finite number of trajectories used in the calculation. Although the instrument is capable of accepting events out to large angles, the quality of the data will decrease at the larger angles due to increasing uncertainty in the angle of incidence and to the increased amount of atmosphere which these particles must traverse before reaching the

FIGURE 10

Geometrical factor for collection of particles impinging on the detector stack at angles less than the indicated maximum angle. Geometrical factors are shown for particles stopping in detectors D<sub>1</sub> and D<sub>7</sub>. The error bars are the result of the finite number of trajectories used in the Monte Carlo calculation.

ORIGINAL PAGE IS  
OF POOR QUALITY



instrument.

Table 4 shows the number per day of cosmic ray particles of each of the elements from Li through Ni that are expected to stop in the instrument after traversing the overlying atmosphere without having undergone a nuclear interaction. Only events with angles of incidence  $<30^\circ$  from the axis of the instrument are included. The values in table 4 are calculated using local interplanetary spectra based on the oxygen spectrum reported by Garcia-Munoz et al. (1977a) and on the elemental abundance ratios compiled by Silberberg et al. (1976) from the work of a number of investigators.

In table 4 rates are shown for geomagnetic cutoffs of 800 MV and 1500 MV, typical of launch sites in southern Canada and the northern United States respectively, as well as for a variety of thicknesses of residual atmosphere. The effects of the residual atmosphere are twofold: first, ionization energy loss in the air causes a given energy interval at the instrument to map into a higher energy interval at the top of the atmosphere, thereby causing particles which had higher rigidity above the atmosphere to be observed, and second, nuclear interactions between cosmic ray particles and the air deplete the population of surviving cosmic rays while

TABLE 4

HEIST Count Rates (events/day) vs.  
Atmospheric Depth and Geomagnetic Cutoff

Element	800 MV cutoff				1500 MV cutoff			
	0g/cm <sup>2</sup>	3g/cm <sup>2</sup>	6g/cm <sup>2</sup>	10g/cm <sup>2</sup>	0g/cm <sup>2</sup>	3g/cm <sup>2</sup>	6g/cm <sup>2</sup>	10g/cm <sup>2</sup>
Li	444	432	365	298	0	0	18	88
Be	366	337	284	230	0.4	38	86	129
B	1200	1070	885	688	134	307	424	508
C	5330	4670	3750	2790	561	1240	1660	1960
N	1510	1260	990	709	336	480	561	605
O	6240	5020	3860	2670	1900	2350	2570	2600
F	127	98	74	50	55	61	62	50
Ne	1330	1010	743	490	548	600	611	490
Na	233	170	124	80	116	120	118	80
Mg	1760	1264	899	578	846	873	854	578
Al	269	189	132	84	147	147	132	84
Si	1380	954	656	417	735	730	656	417
P	66	45	30	19	39	38	30	19
S	326	219	147	92	188	181	147	92
Cl	50	33	22	14	31	30	22	14
Ar	168	110	72	45	102	97	72	45
K	96	62	40	25	62	58	40	25
Ca	265	168	110	68	169	158	110	68
Sc	44	28	18	11	31	28	18	11
Ti	210	132	84	51	155	132	84	51
V	90	56	35	21	68	56	35	21
Cr	185	113	72	43	139	113	72	43
Mn	117	71	45	27	90	71	45	27
Fe	1440	862	545	324	1103	862	545	324
Co	6.1	3.6	2.3	1.3	4.8	3.6	2.3	1.3
Ni	63	37	23	14	48	37	23	14
total	23300	18400	14000	9800	7600	8800	9000	8300
events/sec	.27	.21	.16	.11	.088	.10	.10	.10

ORIGINAL PAGE IS  
OF POOR QUALITY

producing atmospheric secondaries. The fraction of the particles which have undergone nuclear interactions at various depths in the atmosphere can be seen by comparing the rates listed for a 800 MV cutoff in Table 4 for these depths with the rate with no residual atmosphere. Calculations by Silberberg and Tsao (1977) indicate that the isotopic composition of most elements does not vary greatly with atmospheric depth. However, it is clearly desirable to minimize the fraction of atmospheric secondaries collected in order to reduce the uncertainty involved in extrapolating abundance ratios to interplanetary space.

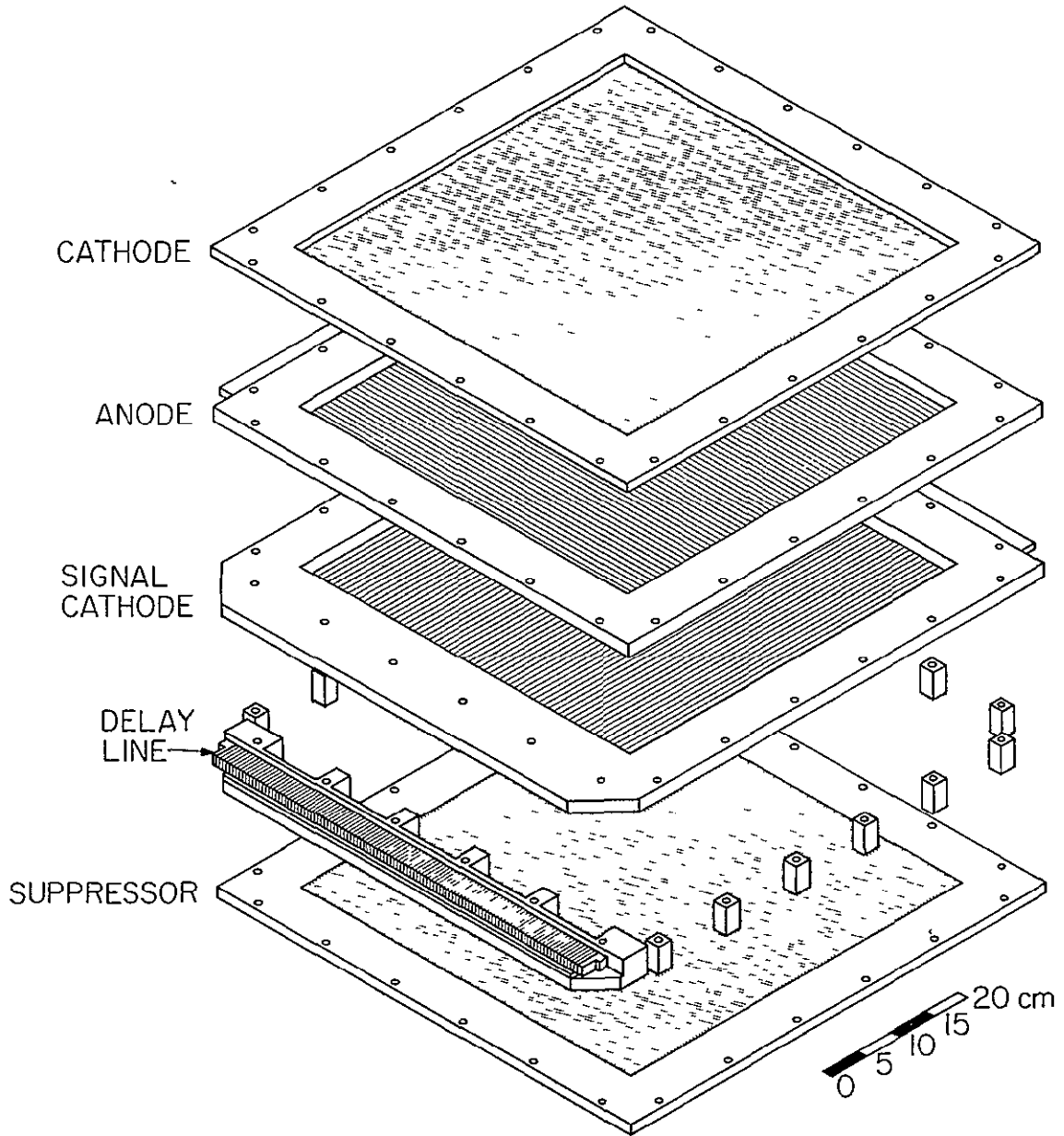
The total thickness of the crystal stack,  $25.3 \text{ g/cm}^2$ , is not negligible compared to the  $56 \text{ g/cm}^2$  nuclear interaction length of Fe in CsI. In the longer ranges approximately  $1/3$  of the incident iron particles will undergo a nuclear interaction and become unusable for mass determination. This limit excludes the possibility of extension of the  $\Delta E-E'$  technique to measurement of cosmic ray isotopes at energies greater than a few GeV/nuc.

### 2.3 Trajectory Measurement

The hodoscope consists of eight identical multiwire proportional chambers. Figure 11 shows a detailed view of a single chamber and table 5 summarizes the mechanical characteristics of the chambers. The sensitive area of the chamber is 48cm x 48cm (2300 cm<sup>2</sup> area). The frames on which the proportional counter planes are constructed are machined out of G-10 epoxy-glass material. Printed circuit boards with copper pads to which the chamber wires can be soldered are inlaid in the frames. The anode plane is composed of 20  $\mu$ m diameter stainless steel wires spaced 4.2 mm apart. There are two cathode planes, each spaced 4 mm away from the anode plane. The upper cathode consists of a sheet of 6.4  $\mu$ m thick aluminized mylar and serves only to establish the appropriate voltage difference across the 4 mm cathode-to-anode gap. The lower cathode is composed of 25  $\mu$ m diameter stainless steel wires spaced 2.1 mm apart. This plane is used both to obtain the required potential difference and to sense (in one dimension) the location at which the avalanche takes place. The cathode wires are oriented perpendicular to the anode wires in order to allow position measurements with finer resolution than the spacing between wires, as will be discussed below. The bottom plane in each MWPC is another sheet of 6.4  $\mu$ m aluminized mylar. This plane,

FIGURE 11

Expanded view of a single multiwire proportional counter. Thicknesses are expanded 4x over the indicated scale for clarity. Wire spacings are not drawn to scale.



ORIGINAL PAGE IS  
OF POOR QUALITY

Table 5

MWPC Mechanical Characteristics

frame material	G-10 (epoxy-glass)
active area	48 cm x 48 cm
cathode-to-anode spacing	4 mm
cathode-to-suppressor spacing	8.9 mm
anode wire spacing	4.23 mm
cathode wire spacing	2.12 mm
anode wires	20 $\mu$ m diameter stainless steel
cathode wires	25 $\mu$ m diameter stainless steel
upper cathode and suppressor	6.4 $\mu$ m mylar, aluminized on both sides

which we call a suppressor, is operated at approximately  $3/4$  of the anode voltage and serves to collect charge deposited in the region below the cathode wires. We employ a cathode coupled delay line readout of the Perez-Mendez design (Grove et al., 1970, 1972, 1973).

The operation of multiwire proportional chambers has been reviewed by Charpak (1970). Electrons which are detached from atoms of the chamber gas by the passage of a charged particle through the sensitive volume of the chamber rapidly drift toward the nearest anode wire. In the region of large electric field near the anode wire they avalanche. The resulting secondary electrons are collected on the anode wire, and as the remaining sheath of positive ions drifts slowly ( $\sim 150$  nsec) through the region of large field near the anode wire an image charge is induced on the cathode wires. The centroid of this image charge distribution in the direction perpendicular to the cathode wires represents the location at which the cosmic ray particle traversed the chamber since the primary electrons have not drifted in this direction.

The image charge is distributed on the cathode wires approximately according to

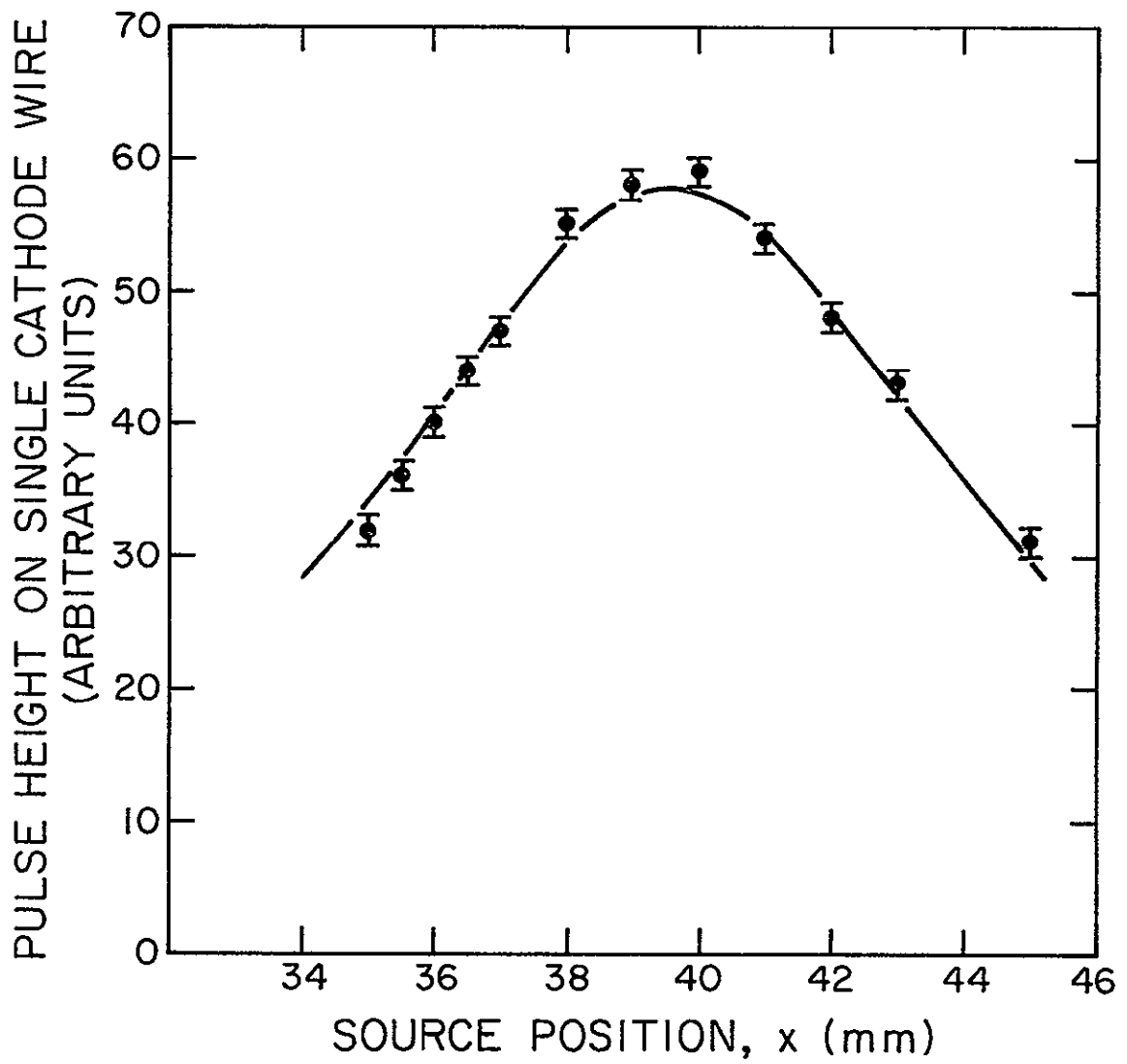
$$Q_n \propto \frac{1}{l_0^2 + (x_n - x)^2} \quad (6)$$

where  $l_0$  is the cathode-to-anode spacing,  $x_n$  is the location of the  $n^{\text{th}}$  cathode wire and  $x$  is the x-coordinate of the cosmic ray trajectory (Lacy and Lindsey, 1973). This expression is easily derived by integrating the image charge distribution on a conducting plane (the cathode plane) due to a point charge (the avalanche) located a distance  $l_0$  above the plane along parallel strips of equal width (the wires). We have measured this distribution in a prototype of our proportional chambers by pulse height analyzing signals on a single cathode wire produced by a collimated source of 5.9 keV x-rays ( $^{55}\text{Fe}$ ). The distance of the source from the wire being analyzed was varied in precisely known steps. The resulting variation of pulse height with source position can be seen in figure 12. In addition, the predictions of equation 6 are shown. We have used the independently determined value of  $l_0 = 5.52$  mm, but have adjusted the height and center position of the curve to fit the data.

For our flight chambers  $l_0$  is 4 mm and the spacing between adjacent cathode wires is 2.1 mm, so  $2/3$  of the total image charge is distributed over  $\sim 5/6$  cathode wires. The centroid of this distribution can be interpolated to a fraction of the wire spacing. The cathode signal is capacitively coupled onto an electromagnetic delay line, resulting in a pair of pulses travelling in opposite

FIGURE 12

Distribution of image charge on MWPC cathode wires due to avalanche at the anode. The data were accumulated using a collimated  $^{55}\text{Fe}$  source of 5.9 keV x-rays. Error bars represent uncertainties in determining the mean of the accumulated distributions of pulse heights. The solid curve shows the expected shape of this distribution, as discussed in the text.



ORIGINAL PAGE IS  
OF POOR QUALITY

directions down the line. Measurement of the difference of the arrival times of these two pulses allows one to determine one coordinate of the cosmic ray's trajectory.

The delay lines which we use are modeled after those developed by the Perez-Mendez group (Grove et al., 1973; Perez-Mendez and Parker, 1974). Table 6 lists the characteristics of our delay lines. It should be noted that the delay and attenuation measurements were obtained while the delay line was clamped to the printed circuit boards of the chamber cathode, thus they include any effects due, for example, to added capacitance to ground. Figure 13 shows pulses obtained at one end of the delay line from identical signals injected at three positions along the line--near each of the ends and near the center. It is clear from the picture that not only does the pulse suffer attenuation by a factor  $\sim 3$  as it traverses the entire length of the line, but its shape is noticeably altered as well. The timing circuitry requires that the signals received at the two ends of the delay line be of approximately the same shape and amplitude. The variation shown in figure 13 caused excessive variation of the time difference obtained by these circuits as the signal amplitude was varied at a fixed position along the delay line.

Table b

Delay Line Characteristics

Mechanical

length	53 cm
width	3.2 cm
thickness	0.32 cm
core material	G-7 (fiber glass with silicone binder)
ground plane	copper strips on kapton backing
compensation material	aluminum strips on mylar backing, strips at 45° to axis of line
winding	82 turns/cm (208/inch) of 38 AWG magnet wire

b4

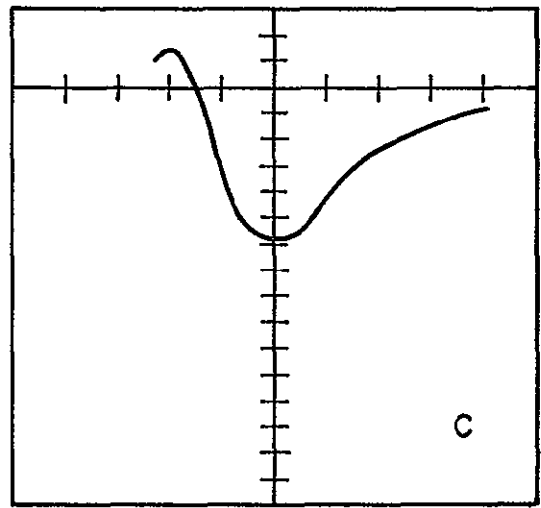
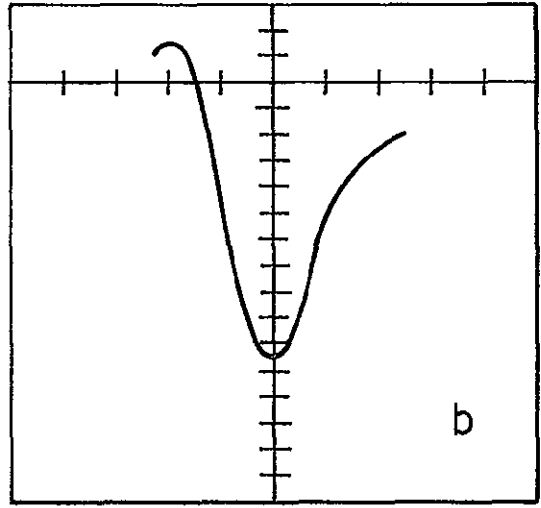
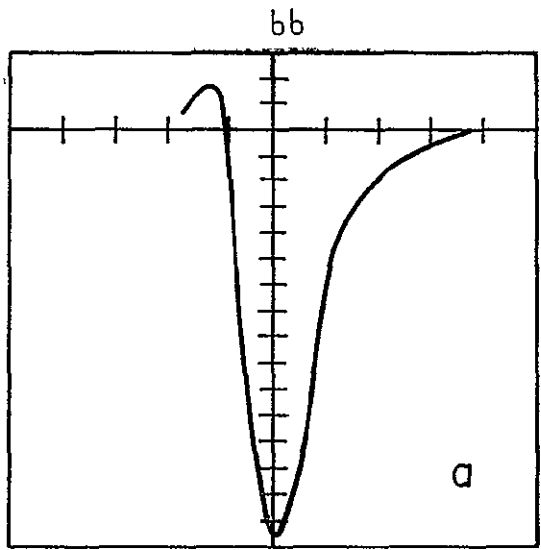
Electrical

delay	15 nsec/cm
characteristic impedance	1500 $\Omega$
attenuation (for MWPC pulses)	factor of 2 per 34 cm
DC resistance	11 $\Omega$ /cm

ORIGINAL PAGE IS  
OF POOR QUALITY

FIGURE 13

Pulse shapes received at one end of 53 cm long delay line for identical pulses injected near the receiving end (a), near the center (b) and near the opposite end (c). Tick marks on the horizontal axes are separated by 100 nsec and those on the vertical axes are separated by 4 mV.

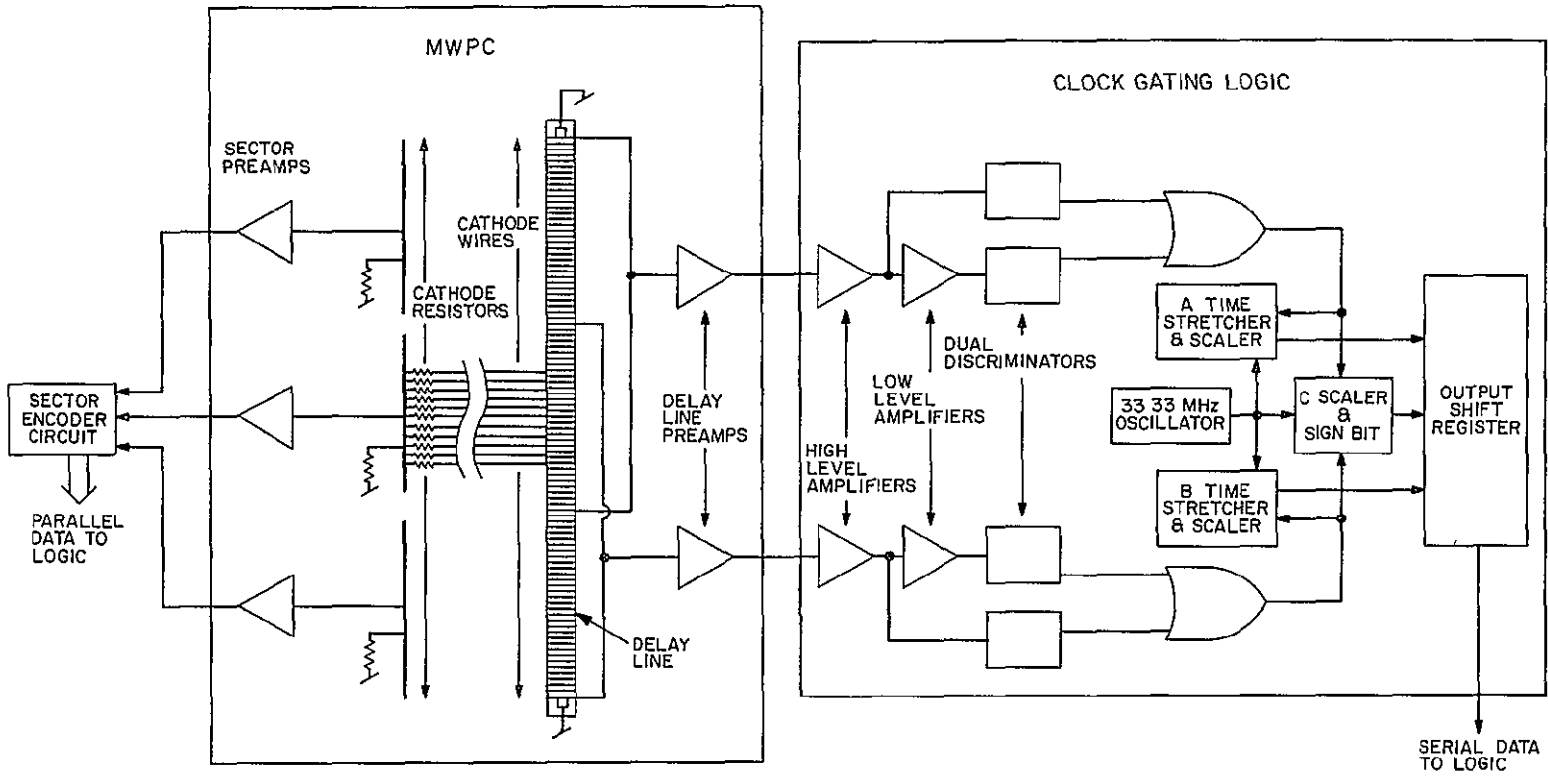


To reduce the magnitude of this effect a system of taps was devised. The delay line is divided into thirds as shown in figure 14. Signals from one end of the delay line and from the delay line tap located nearest to the opposite end of the line are connected together at the input to a preamplifier located midway between these points. Similarly signals from the other end and the other tap are connected at the input of a second preamp. In obtaining the time differences for an event the timing circuitry ignores all but the first pulse from each preamp, so the position measurement is unaffected by the eventual arrival of the delay line pulse at the second input to the preamp. Also, reflections from the ends of the delay line (the preamps have input impedances much less than the characteristic impedance of the line) will not affect the measurement.

With this arrangement of taps the maximum time difference corresponds to  $1/3$  of the entire delay line and the degree of attenuation and distortion of the pulses is reduced. However, an ambiguity has been introduced--any given time difference will correspond to three different positions in the chamber. In order to resolve this ambiguity a system of charge sensitive amplifiers and comparators was introduced. A fixed time after the passage of a charged particle through the instrument the

FIGURE 14

Block diagram of position sensing  
circuitry.



b9

ORIGINAL PAGE IS  
OF POOR QUALITY

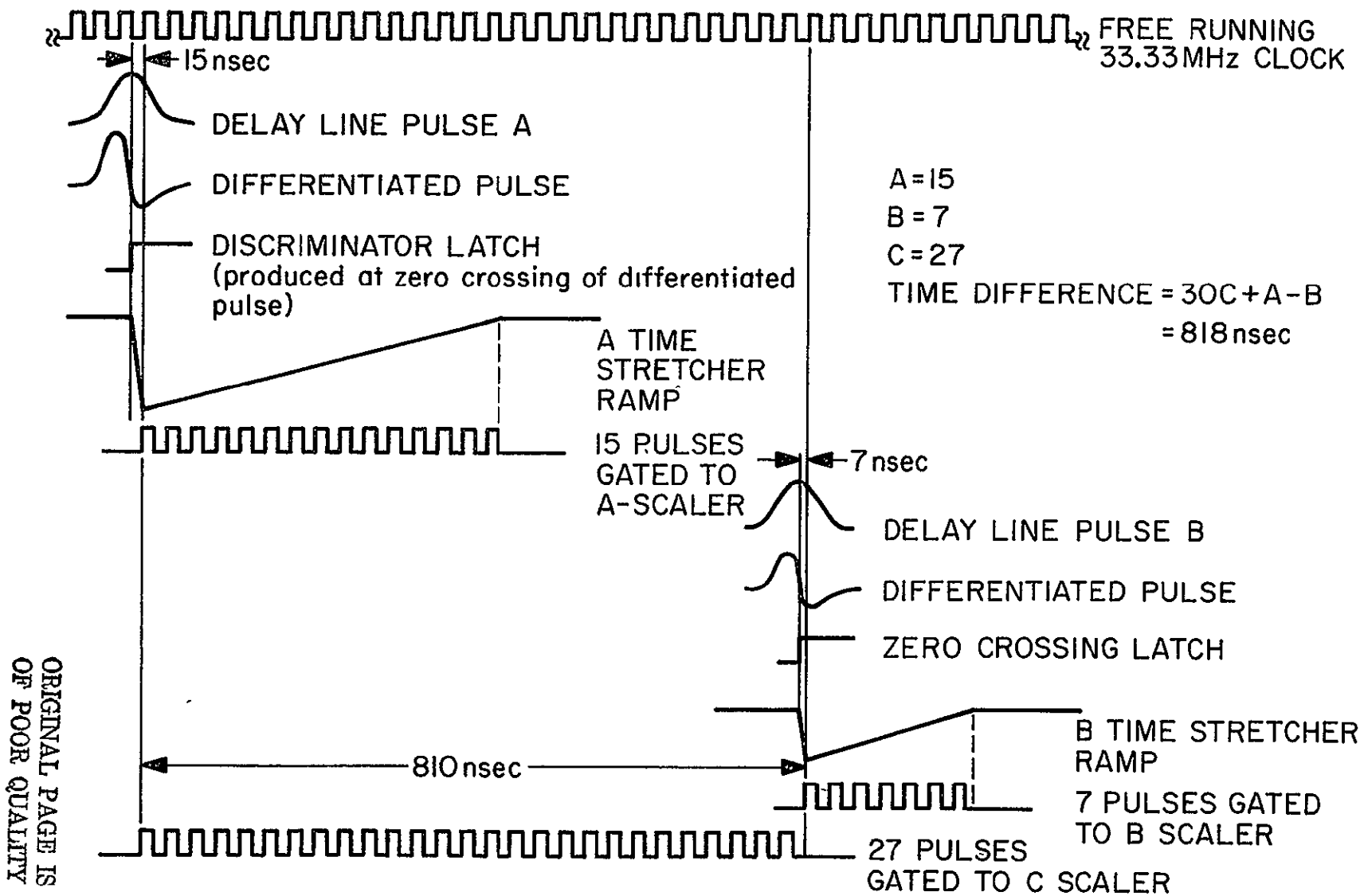
outputs of these sector preamps are examined and the number of the sector having the largest signal is encoded and inserted into the data stream for that event.

Figure 14 is a block diagram of the position sensing circuitry and figure 15 shows how a digital time difference is obtained from the two delay line pulses. The output of a delay line preamp goes into a "high level amplifier" which differentiates and amplifies the pulse. The output of this amplifier goes two places: first, to a discriminator which will produce a logic pulse at the time of the zero crossing of the differentiated pulse if the pulse amplitude is sufficiently large, and second, to another stage of amplification followed by an identical discriminator. The two discriminator pulses are "ORed" to produce the pulse which defines one end of the time interval. This dual amplifier and discriminator arrangement is required to handle the large dynamic range of signals expected from the hodoscope,  $\sim 130:1$ .

When the pulse is large enough to trigger the high level discriminator, the timing will be done using this pulse since propagation delays through the low level amplifier ensure that the high level pulse will arrive first. The discriminator pulse initiates the charging of a capacitor by the time stretcher circuit. When the next

FIGURE 15

Example illustrating the processing of delay line pulses to obtain a digital time difference.



ORIGINAL PAGE IS  
 OF POOR QUALITY

pulse from the 33.33 MHz clock arrives the time stretcher starts to discharge this capacitor at  $1/29$  of the charging rate. During the discharge time clock pulses are gated to the "A-scaler". The final count in this scaler represents the time interval (measured in nanoseconds) between the arrival of the pulse from the delay line and the occurrence of the next clock pulse. The other delay line pulse is treated in an identical manner resulting in a second vernier measurement in the "B-scaler". Finally, the "C-scaler" counts the number of clock pulses between the arrivals of the two delay line pulses. This C-scaler count gives the gross time interval (in units of 30 nsec), and the combination  $30C+A-B$  is the total time difference in nanoseconds.

We have found that in order to obtain position resolution which is not limited by the spacing of the cathode wires it is essential that the charge deposited outside of the active volume of the chamber, beyond the plane of cathode wires, not be allowed to drift to the anode. The suppressor plane was introduced to achieve this result. If this charge were permitted to drift to the anode, it would distort our measurements of the position of the cosmic ray's track since the electric field lines which the electrons follow in this region have a component in the direction which we are trying to

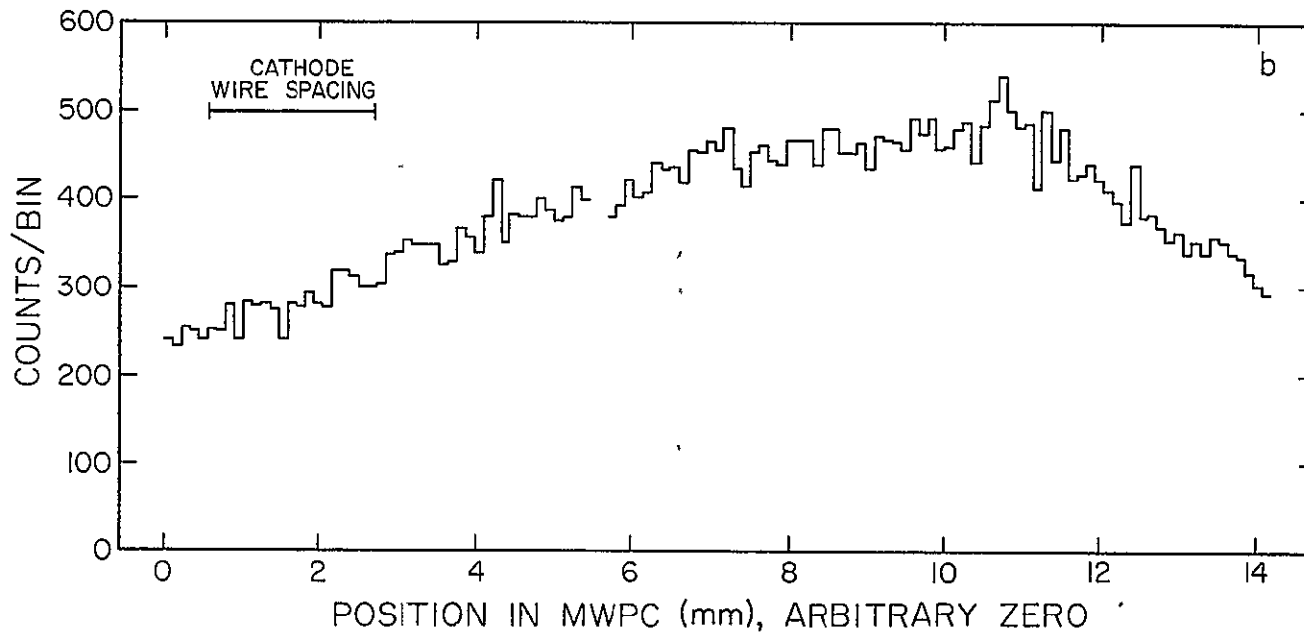
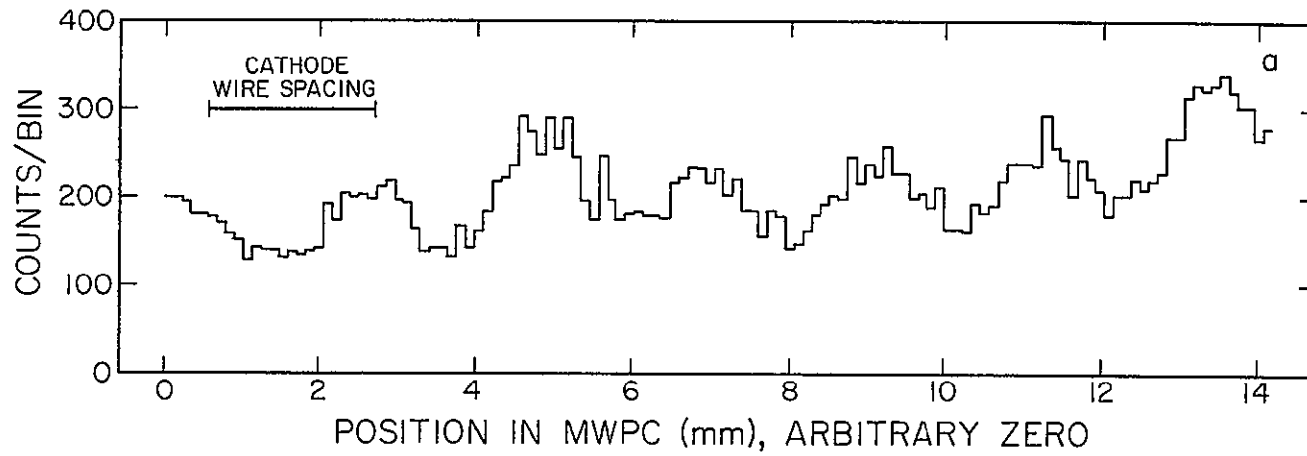
measure. This effect is illustrated in figure 1b. A prototype chamber was illuminated by an uncollimated  $^{55}\text{Fe}$  source and distributions of the resulting positions were accumulated. The data in figure 1ba were accumulated with the suppressor grounded. The resulting distribution consists of a number of peaks produced by the effect described above added to a smooth distribution obtained from x-rays which interacted in the normally active volume of the chamber. Data in figure 1bb were taken with the suppressor biased at 1500 volts. The peaks have been eliminated since the suppressor can now collect the charge deposited in the volume between the cathode plane and the suppressor. In both distributions the smooth large scale structure is due to non-uniform illumination by the x-ray source. When the chamber is illuminated with charged particles the effect of the suppressor is less dramatic, since in this case each event deposits charge in both the active region and in the region between cathode and suppressor planes. When the suppressor is not biased the measured position will be an average of the positions at which the charge from the normally active region and the charge from the region between the lower cathode and the suppressor arrive at the anode of the chamber, weighted by the magnitudes of the charges.

FIGURE 1b

MWPC response to uncollimated  $^{55}\text{Fe}$  x-ray source. The spacing between adjacent cathode wires is indicated.

a) No bias applied to suppressor.

b) Suppressor biased at 1500 volts.



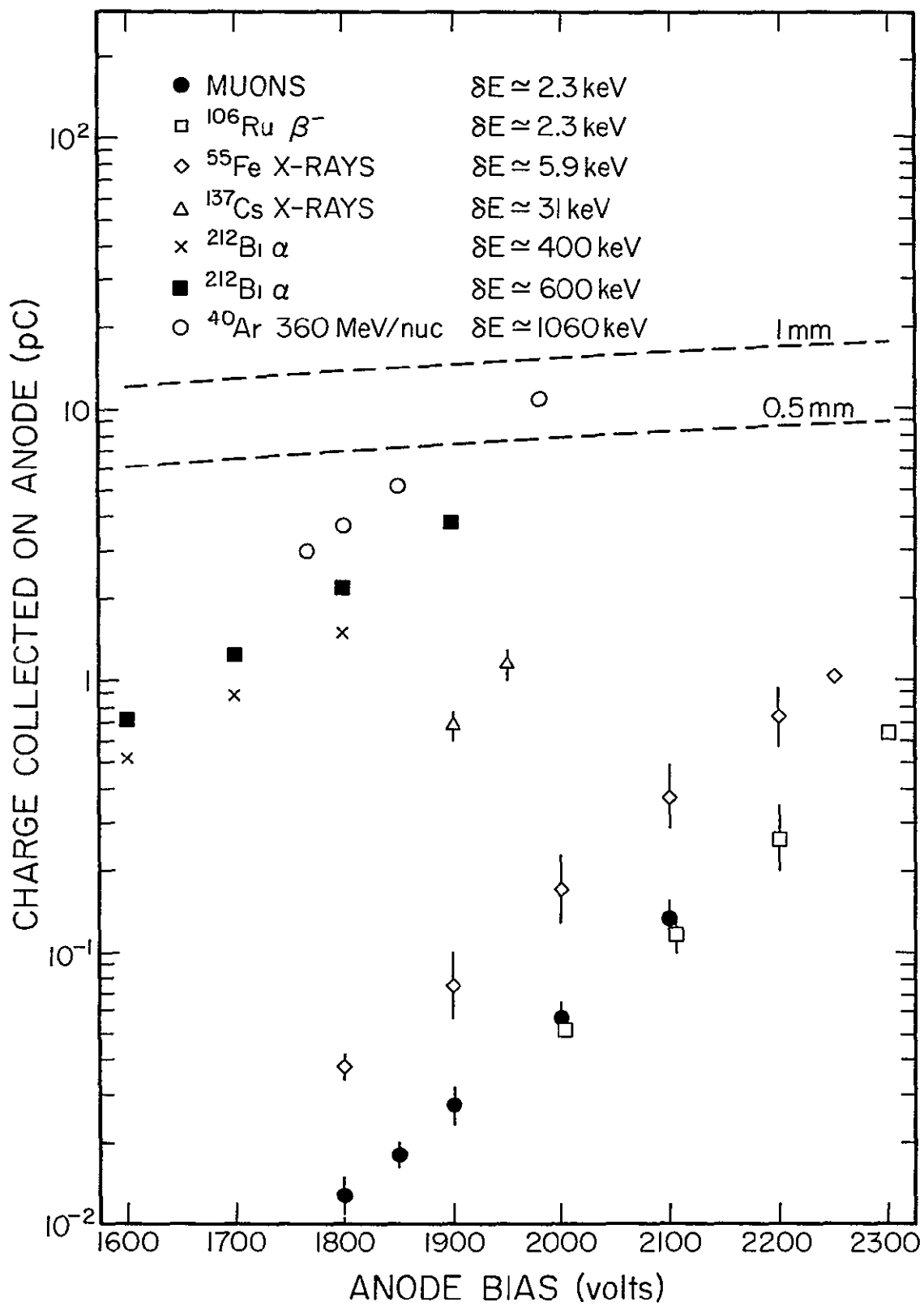
ORIGINAL PAGE IS  
OF POOR QUALITY

We use a mixture of 70% Ar plus 30% CO<sub>2</sub> as the proportional chamber gas. We have measured the gain characteristics of our chambers when stimulated with various sources of radiation. Figure 17 shows the charge collected on the chamber anode as a function of the anode voltage for each of these radiations. Where error bars are included they indicate the range of charges collected when a number of different proportional counters were tested. These gain differences are believed to be due to small variations in the chamber geometry (which will alter the chamber capacitance and thereby alter the static charge on the anode and the chamber gain) and possibly in part to a small degree of contamination of the chamber gas.

Our estimates of the energy deposited in the 1.34 mg/cm<sup>2</sup> active thickness of the chamber are indicated in the figure. At any given value of the anode voltage, the measured charges do not increase in proportion to the energy deposited. The dashed lines in the figure indicate the magnitude of the static charge on sections of the anode wire 0.5 mm and 1.0 mm in length. Doolittle et al. (1973) estimate that the effective length along the anode wire of the distribution of charge produced in the avalanche will lie within these limits for a chamber geometry similar to ours. When the charge in the

FIGURE 11

Charge collected on MWPC anode when exposed to various sources of radiation as a function of anode voltage. The error bars, where present, indicate the range of measurements obtained from a number of chambers that were tested. Also indicated are the charge levels (indicated by dashed lines) at which space charge effects are expected to be significant, as discussed in the text.



ORIGINAL PAGE IS  
OF POOR QUALITY

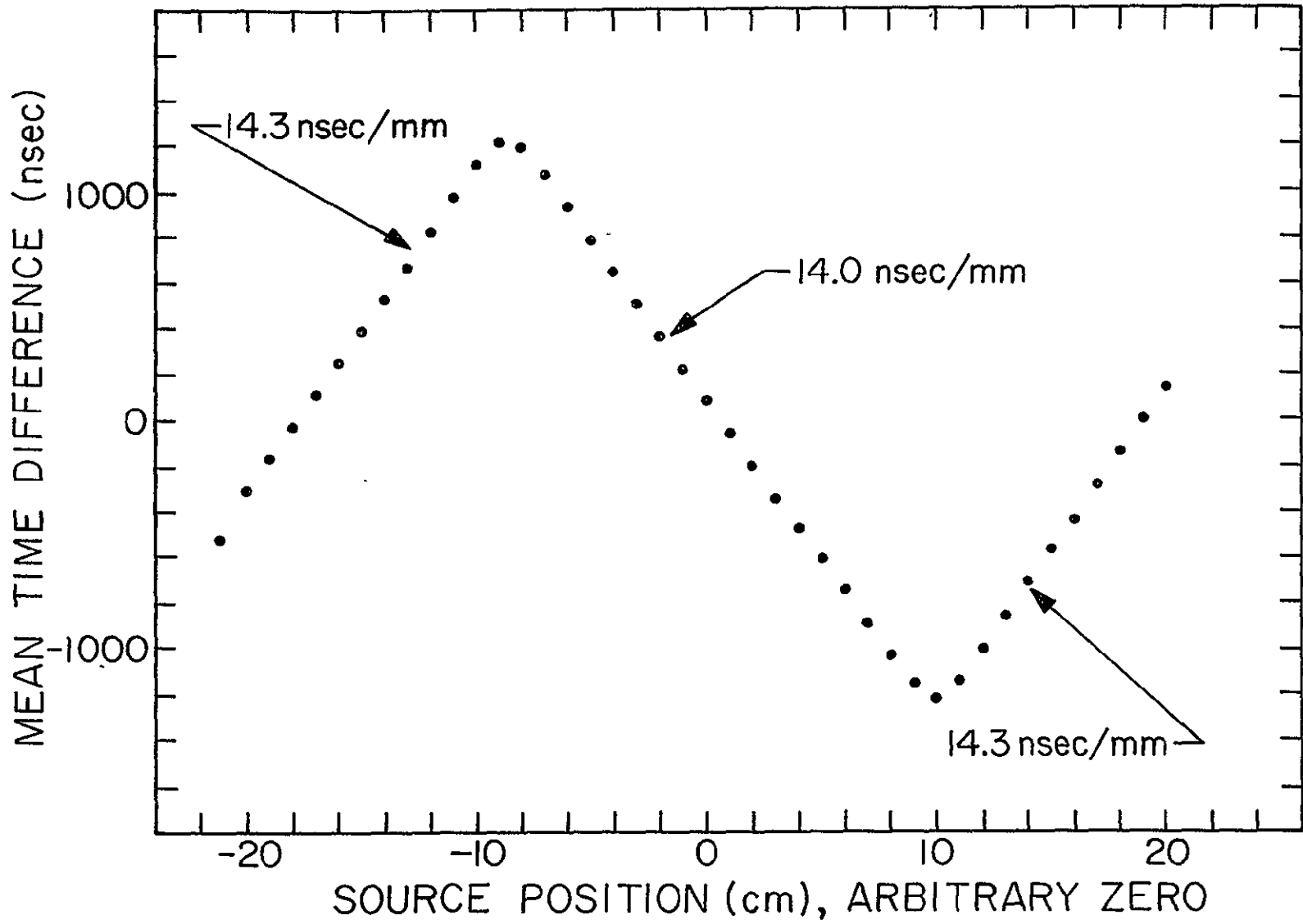
avalanche is comparable to this static charge, a reduction in the gain of the chamber is expected since the charge in the electron cloud reduces the electric field seen by late arriving electrons.

Ideally, the position measurements made using the techniques described above should be independent of the amplitude of the pulse being measured. However we observe a residual peak-to-peak time variation of  $\sim 15-25$  nsec when we stimulate the chambers with pulses of various amplitudes at a fixed position. The main dependence on pulse amplitude of the technique which we use to measure position is caused by failure of the analog circuits at the two ends of the delay line to precisely track one another due to attenuation of the delay line pulses.

Figure 18 shows the transfer function (time vs. position) obtained in one of the hodoscope planes. These data were obtained by accumulating distributions of times while exposing the chamber to a beam of collimated alpha particles obtained from the decay of  $^{212}\text{Bi}$  (a short lived descendant of  $^{228}\text{Th}$ ). This source was mounted on a movable stage driven by a precision lead screw. After the desired number of events (typically 4000-5000) had been accumulated at a given source position, the source was moved a selected distance and the next distribution was

FIGURE 18

MWPC transfer function (time vs. position) measured using collimated  $\alpha$ -source. The errors in measuring both the position and time difference are too small to be displayed on this scale.



accumulated. The figure shows that there is a sizeable deviation from linearity near each of the taps. Distortion of the transfer function is to be expected at positions located closer to a tap than the width of a typical delay line pulse, ( $\sim 150-200$  nsec or  $\sim 10-13$  mm). At these places pulses travelling in both directions arrive at the most distant delay line preamp close enough in time to overlap and cause the shaping amplifier to slightly alter the time of the zero-crossing of the differentiated delay line pulse.

Figure 19 shows a more detailed view of the response of one pair of hodoscope planes over a 10 mm interval near the center of the chamber. These data were accumulated at source positions 0.2 mm apart. Figure 19a is a plot of time vs. position, figure 19b shows the standard deviation of the time distributions obtained, and figure 19c shows the deviations of the means of the distributions from a least squares straight line fit. The fact that the deviations from a straight line are small, at least over distances as large as 1 cm, shows that a relatively small number of calibration points are required to obtain the transfer function of each hodoscope plane to the accuracy that we require.

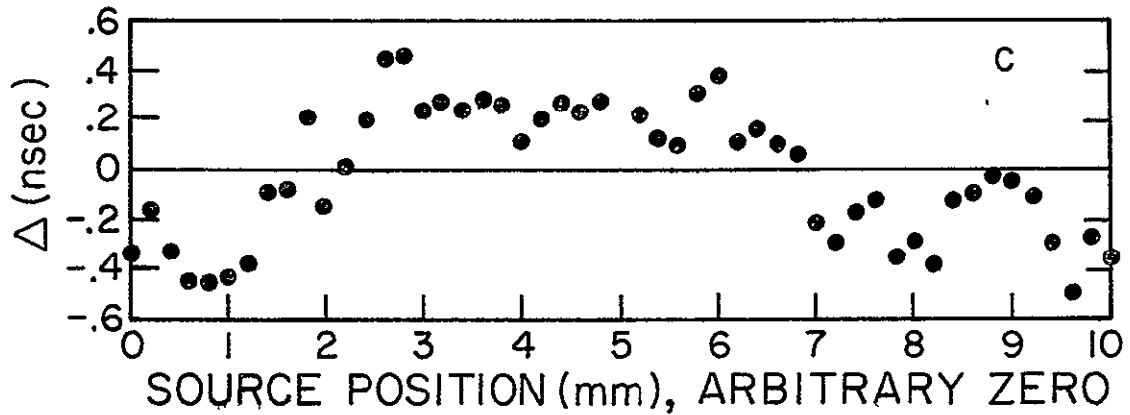
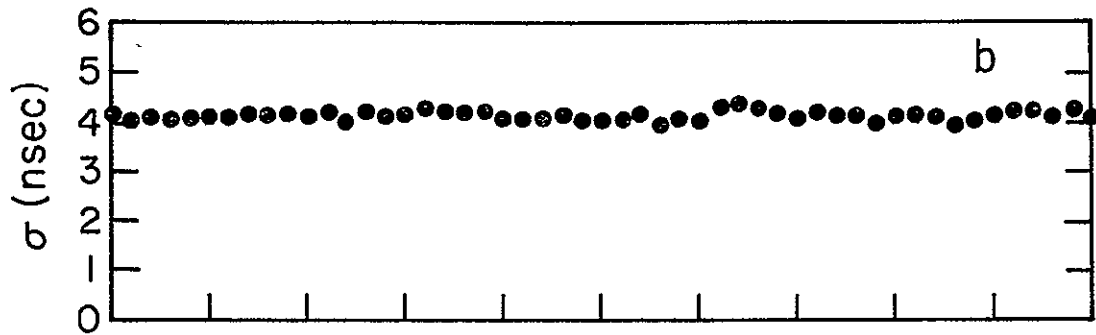
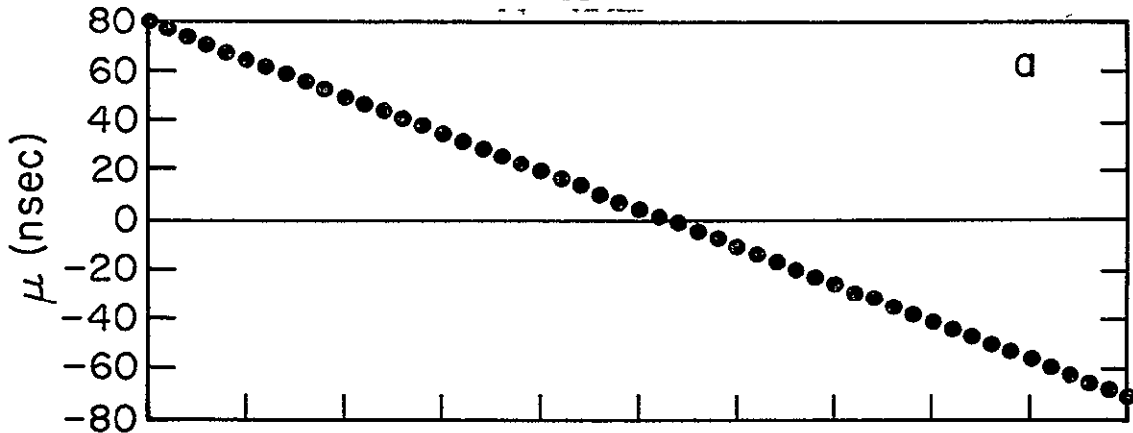
FIGURE 19

MWPC response over a limited section of the chamber (1 cm), measured with a collimated  $\alpha$ -source.

a) Mean time ( $\mu$ ) vs. position transfer function.

b) Standard deviation ( $\sigma$ ) of the measured position distributions.

c) Deviation ( $\Delta$ ) of transfer function from best-fit straight line.



ORIGINAL PAGE IS  
OF POOR QUALITY

Figure 20 shows the MWPC resolution (rms) as function of signal amplitude. The points indicated by dots and triangles were obtained by using a pulser signal with a 150 nsec rise-time injected onto one of the cathode wires. The shape of this curve is the result of random noise in the input stages of the delay line amplifiers. Also included on the plot are points obtained by using a collimated  $^{210}\text{Po}$  alpha source and varying the chamber high voltage in order to vary the pulse amplitude produced. The correspondence between pulser amplitude and anode charge was obtained by observing pulses from both the pulser and from charged particles at the output of the delay line preamps. The rms widths of the  $\alpha$  distributions track those of the pulser well at low amplitudes, but then level off at  $\sim 4$  nsec (FWHM  $\sim 9.4$  nsec). This is predominantly the result of the finite size of the collimator being used.

In figure 21 we show typical time distributions acquired using various sources of radiation. A collimated source of alpha particles (8.785 MeV kinetic energy) from the decay of  $^{212}\text{Bi}$  was used to produce the distribution in figure 21a. Figures 21b and c show histograms of time differences of x-coordinates measured in the X1 and X2 proportional counters when the hodoscope was exposed to parallel beams of fully stripped  $^{40}\text{Ar}$  ions at energies of

FIGURE 20

Dependence of the rms position resolution in a single MWPC on pulse amplitude. Measurements are shown for the chamber stimulated with an electronic pulser and with a collimated source of  $\alpha$ -particles. The insert shows the collimator geometry used.

ORIGINAL PAGE IS  
OF POOR QUALITY

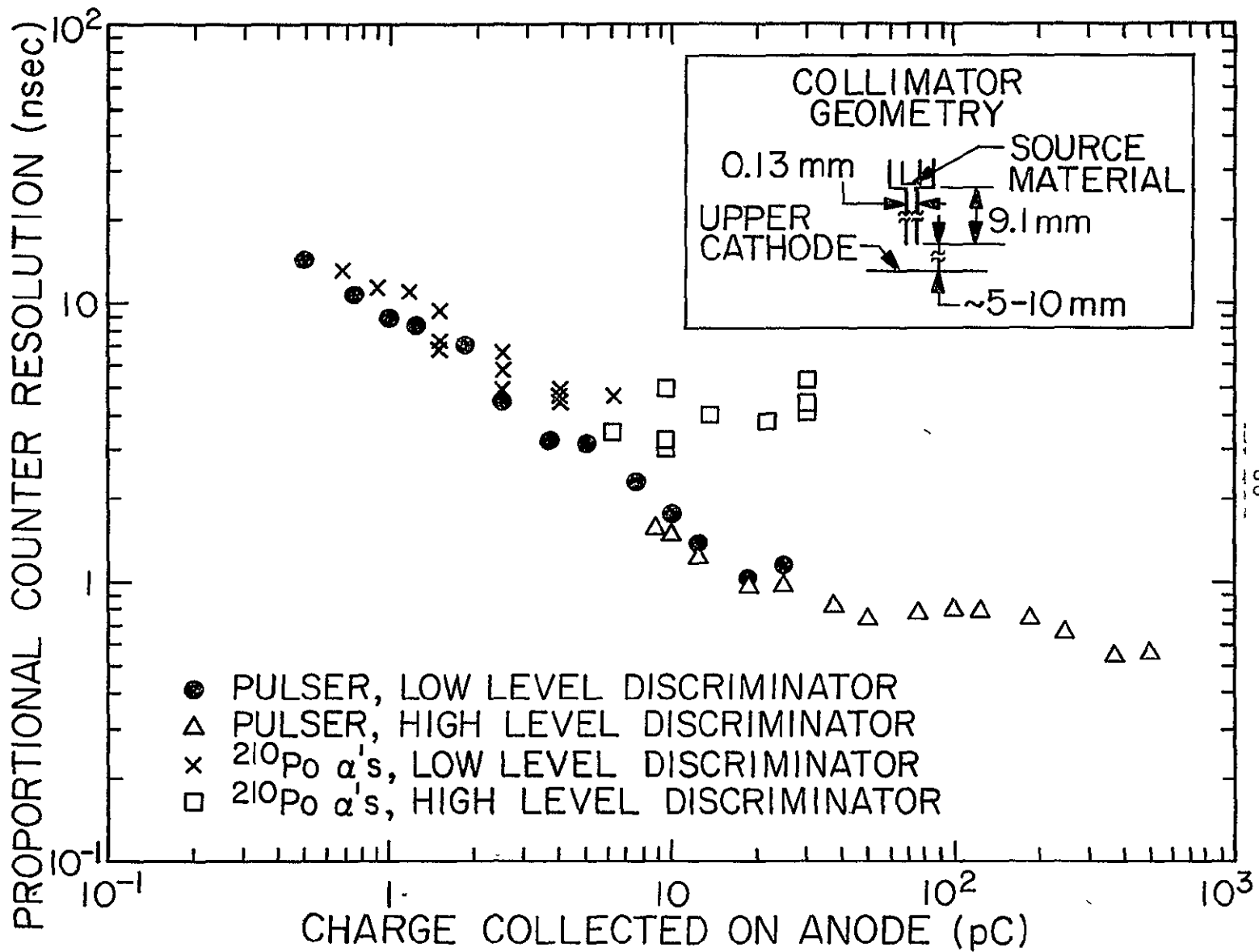


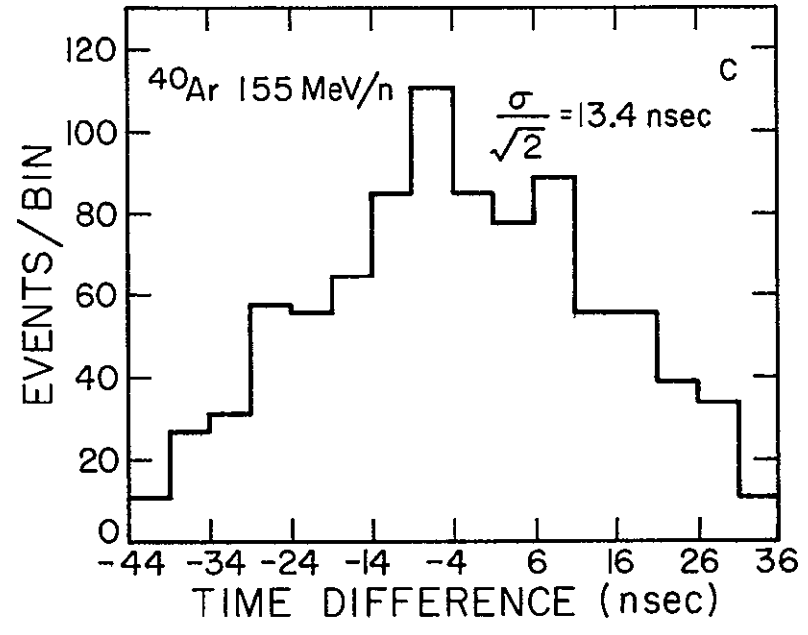
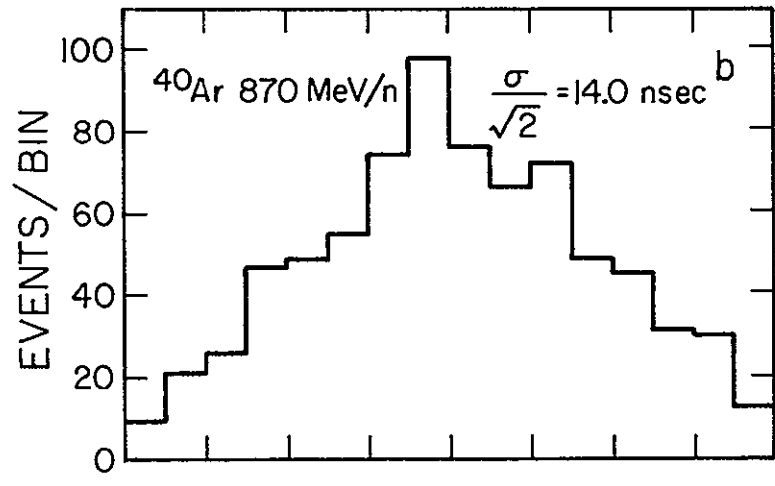
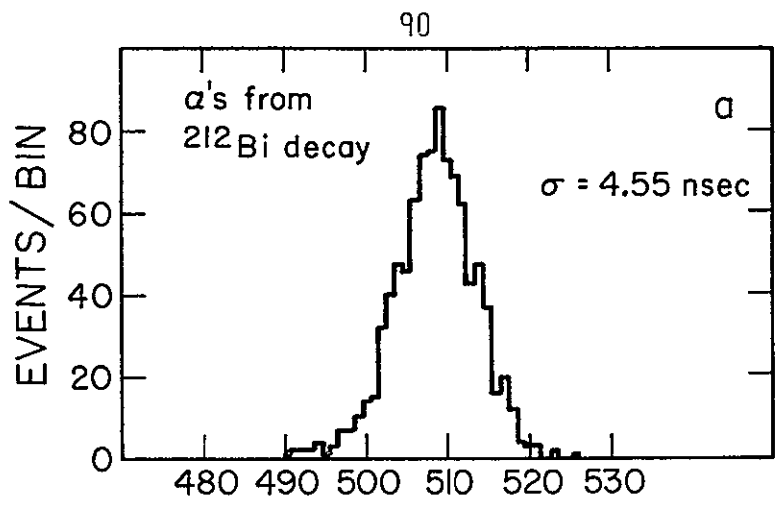
FIGURE 21

Time distributions illustrating MWPC resolution.

a) Chamber stimulated by a collimated source of  $\alpha$ -particles.

b) Chamber stimulated by a parallel beam of normally incident, fully stripped  $^{40}\text{Ar}$  ions at 870 MeV/nuc. The abscissa is the difference between position measurements in the  $X_1$  and  $X_2$  proportional counters. The areas of the hodoscope from which events are selected is discussed in the text.

c) Same as (b) for 155 MeV/nuc  $^{40}\text{Ar}$ .



ORIGINAL PAGE IS  
OF POOR QUALITY

870 MeV/nuc and 155 MeV/nuc respectively. Events selected for inclusion in these plots lie within a band extending 2000 nsec ( $\sim 13$  cm) in the y direction and 33 nsec ( $\sim 2$  mm) in the x direction. By using the difference  $X_1 - X_2$ , we eliminate the mean variation of the measured time over this 33 nsec x interval. Since both  $X_1$  and  $X_2$  are subject to random errors and these errors are independent and are assumed to come from distributions of the same standard deviation, we must divide the standard deviation obtained from the distribution of  $X_1 - X_2$  by  $\sqrt{2}$  in order to obtain the resolution of a single hodoscope plane. The resolution obtained using energetic  $^{40}\text{Ar}$  ions is significantly larger than that obtained using alpha particles (where the resolution obtained is limited by the size of the collimator employed). This may be related to the production of knock-on electrons in the former case. However, this possibility has not been thoroughly investigated.

The trajectory of a particle passing through the hodoscope can be determined from two measurements of its x position and two measurements of its y position along its track. For each event we make four measurements of x and four of y. These redundant measurements permit a consistency check of the hodoscope data. In addition, doubling the number of position measurements improves the

overall position resolution by a factor of approximately  $\sqrt{2}$ . In appendix B the uncertainties in  $\sec\theta$  and in the position at which the particle's track passed through the various scintillators are derived from the hodoscope resolution and the geometrical configuration of the instrument. For the hodoscope geometry used in this experiment the relative uncertainty in our determination of  $\sec\theta$  is found to be

$$\frac{\sigma_{\sec\theta}}{\sec\theta} = 0.0016 \cdot \sin 2\theta \cdot \sigma_{\text{MWPC}}$$

where  $\theta$  is the particle's angle of incidence and  $\sigma_{\text{MWPC}}$  is the position resolution in a single proportional counter in millimeters. This contribution to our thickness uncertainty is shown in figure 22.

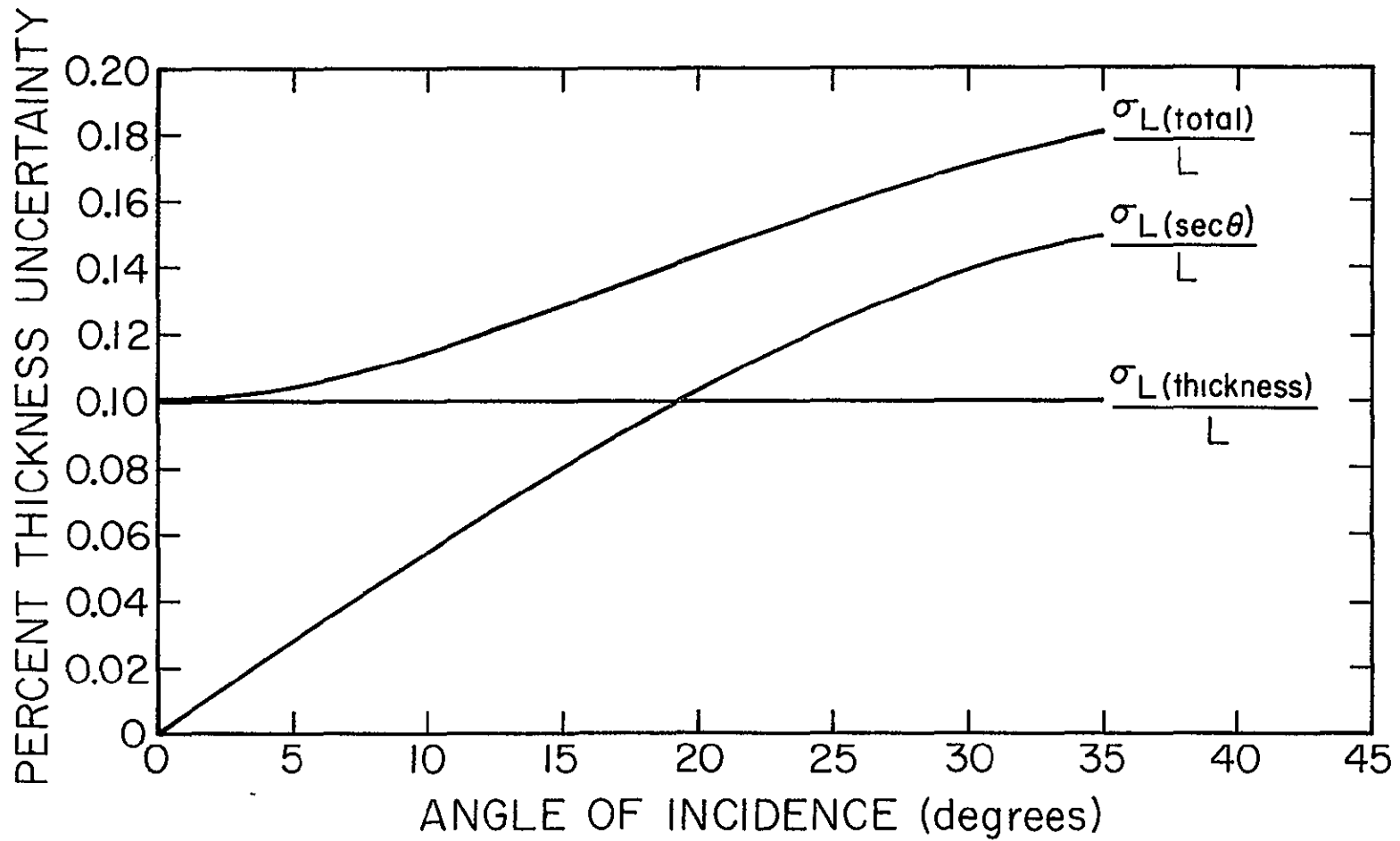
Also shown in figure 22 is the contribution to our thickness uncertainty due to the crystal thickness variations (to be discussed later). This contribution depends on the precision with which we can determine the position at which the particle passed through each of the scintillators. In appendix B we show that the uncertainty in the x and y positions at which a particle's track intersects a given level in the scintillator stack varies between 0.87 and 1.09 times  $\sigma_{\text{MWPC}}$ .

ORIGINAL PAGE IS  
OF POOR QUALITY

FIGURE 22

Relative uncertainty (rms) in  $\Delta E$  detector thickness,  $L$ , along with contributions due to angular uncertainty and to thickness mapping uncertainty. These uncertainties are plotted as a function of the particle's angle of incidence,  $\theta$ .

ORIGINAL PAGE IS  
OF POOR QUALITY.



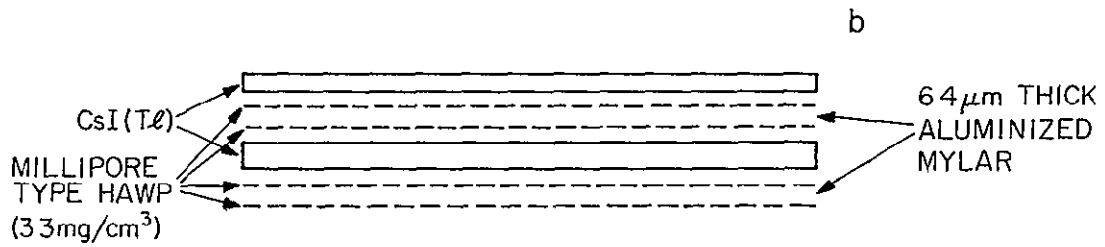
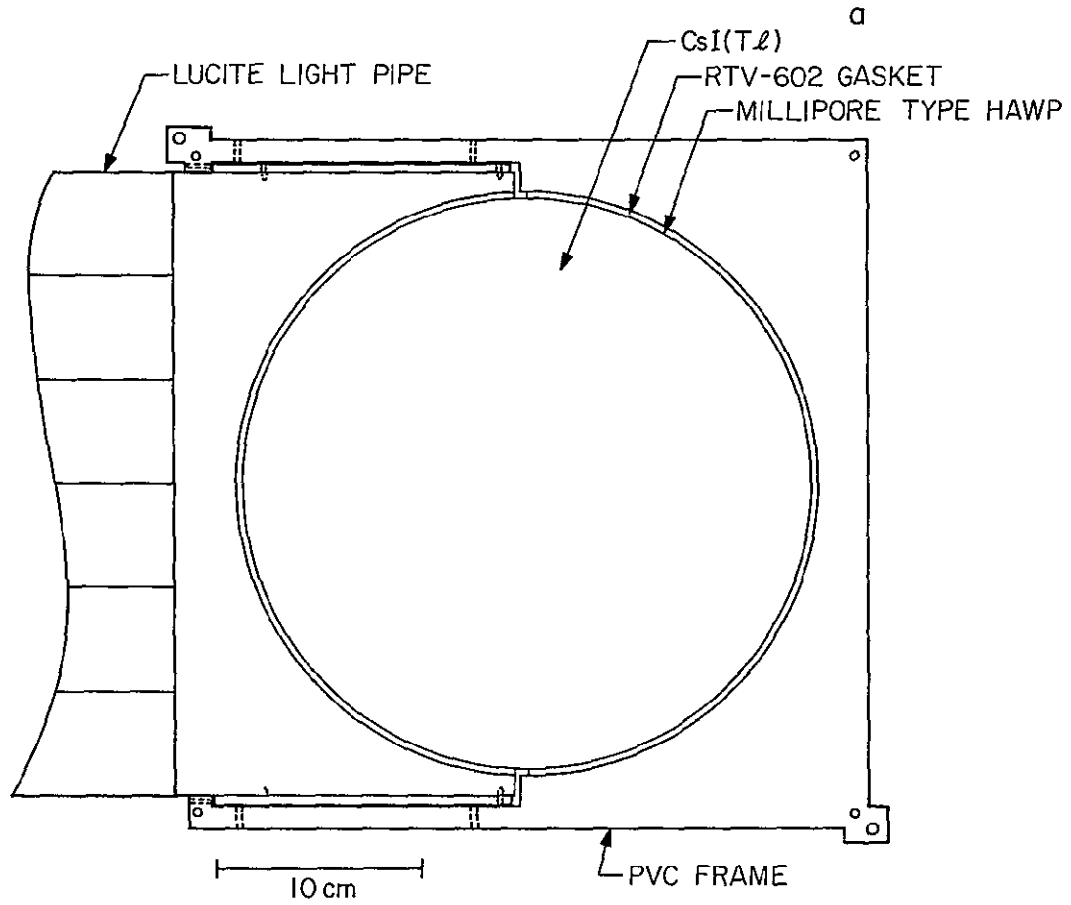
## 2.4 Energy Measurements

A detailed view of the scintillator stack is shown in figure 23. Each scintillator is a disk of CsI(Tl) (Harshaw Chemical Company, Solon, Ohio) eleven inches (27.9 cm) in diameter. The thicknesses vary from 3 mm ( $1.35 \text{ g/cm}^2$ ) to 17 mm ( $7.67 \text{ g/cm}^2$ ). The top and bottom faces of each disk have Harshaw's "standard crystal polish" while the circumferences are unpolished. Each crystal is connected to a lucite light pipe. The light pipe is coupled to the crystal along  $1/2$  of the crystal's circumference through a RTV-602 transparent silicone rubber gasket. The opposite edge of the crystal is in contact with a thin strip of Millipore filter paper (type HAWP) which acts as an efficient diffusely reflecting surface at the wave lengths of the CsI(Tl) emission. This filter paper is backed by another RTV-602 gasket which acts as a deformable cushion attached to a PVC plastic frame. A pair of screws pull this assembly together and force the light pipe into optical contact with the scintillator. The light pipe is divided into six lucite strips which are bent so as to adiabatically transport light to the face of a 130 mm (5") photomultiplier tube (EMI 9530R).

FIGURE 23

Mechanical assembly of the scintillator stack.

- a) Coupling between CsI(Tl) scintillator and lucite light pipe.
- b) Material used to separate adjacent crystals (not to scale).



ORIGINAL PAGE IS  
OF POOR QUALITY

Successive scintillators are separated by two sheets of Millipore and a single sheet of aluminized mylar. The total amount of material between crystals is approximately  $7 \text{ mg/cm}^2$ . The aluminized mylar is used to ensure that light produced in one crystal will not be transmitted into an adjacent crystal. The Millipore sheets in contact with each of the crystal faces improve the transport of light to the light pipes. Tests indicate that diffuse reflection by the Millipore dominates internal reflection at the crystal-air interface, presumably due to inadequate polishing of the crystal surfaces. On some of the crystals an additional "compensation piece" of aluminized mylar was added over a fraction of the crystal surface between the crystal and the Millipore. This piece serves to reduce the light collection efficiency in areas where it otherwise would be excessively large. The result is smaller light collection gradients.

It is necessary to obtain thickness maps of each of the scintillators. Low resolution maps were made for each of the crystals by looking at the variation of the attenuation of a beam of collimated, low energy  $\gamma$ -rays. The crystal to be measured was positioned between the  $\gamma$ -ray source ( $^{57}\text{Co}$  with  $E_\gamma=122 \text{ keV}$  or  $^{133}\text{Ba}$  with  $E_\gamma=356 \text{ keV}$ ) and a small NaI(Tl) scintillator (2.54 cm diameter x 2.54 cm thick) mounted on a pm tube. The

counting rate in the photopeak seen in the NaI(Tl) scintillator was measured with the CsI(Tl) crystal in a number of positions. The difference in thickness between two places on the crystal can be obtained from

$$\Delta z = \frac{1}{\mu} \ln \left( \frac{N_0}{N} \right)$$

where  $\Delta z$  is the thickness difference,  $\mu$  is the  $\gamma$ -ray absorption coefficient of CsI(Tl) at the energy of the  $\gamma$ -ray being used, and  $N_0$  and  $N$  are respectively the number of counts obtained in a fixed time interval at a reference position (the center of the disk) and at the position of interest. The number of counts required in order to obtain an uncertainty of  $\sigma_{\Delta z}$  in the thickness difference measurement is

$$N = \frac{2}{(\mu \sigma_{\Delta z})^2}$$

where we have used the fact that  $N_0 \sim N$  for the thickness differences which we are considering. In order to obtain thickness differences with uncertainties less than 0.1% of the crystal thickness it was necessary to obtain between  $1 \times 10^5$  and  $8 \times 10^6$  counts at each position, depending on which crystal was being mapped and which of the  $\gamma$ -ray sources was being used. Each thickness measurement was an average over an area  $\sim 2$  to  $3$  cm in diameter.

ORIGINAL PAGE IS  
OF POOR QUALITY

One of the resulting maps is shown in figure 24. The maximum thickness gradients obtained over the area which we were able to map ranged between 1.2 and 2.9  $\mu\text{m}/\text{mm}$  on all crystals except D5. The D5 crystal exhibited thickness variations as large as 6  $\mu\text{m}/\text{mm}$ . If we estimate the thickness gradients in the various combinations of crystals to be used for the  $\Delta E$  measurement (that is, in the combination D0 through Dn-1 for the case where a particle stops in Dn) by simply summing the maximum thickness gradients in each of these crystals, we find that this overall gradient is less than 0.1% of the  $\Delta E$  detector thickness per mm in all cases. This gradient combined with our position resolution yields a relative thickness uncertainty of

$$\frac{\sigma_{L(\text{thickness})}}{L} \lesssim 0.001 .$$

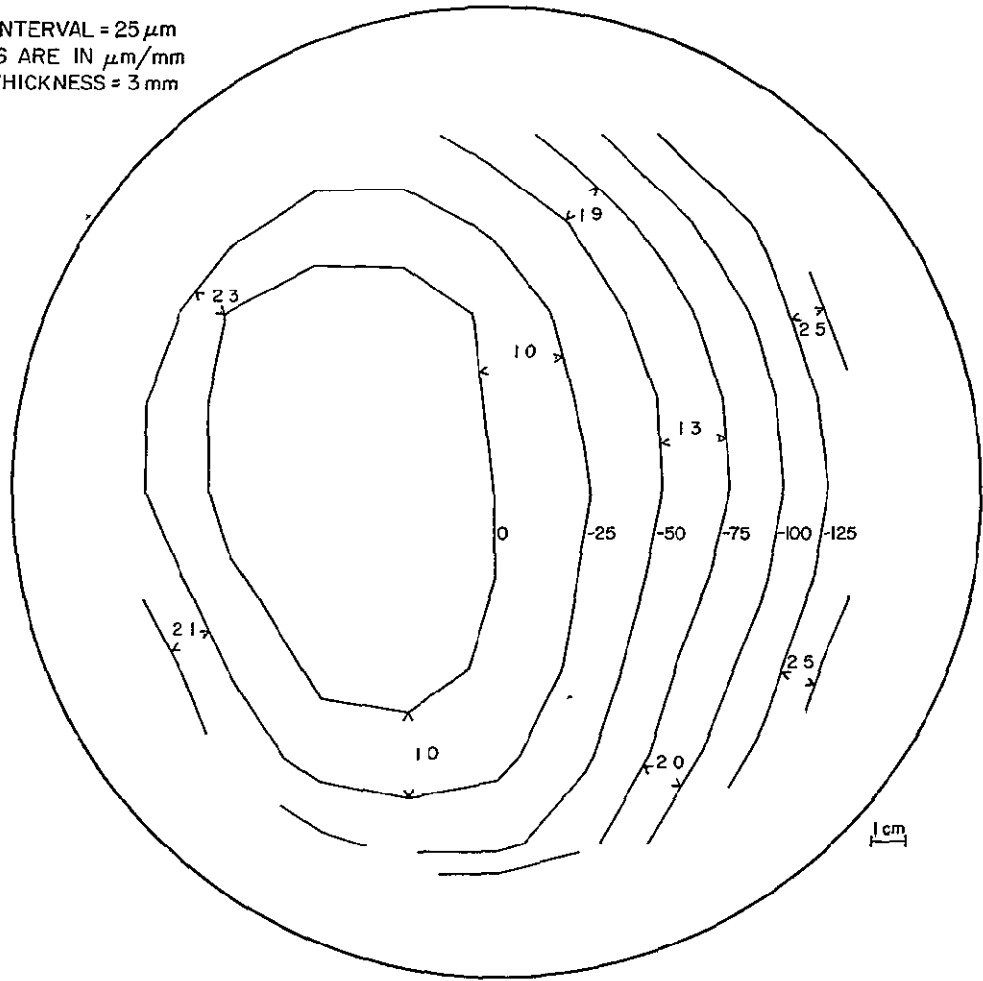
Here we have assumed that uncertainties in the thickness at any given point in the crystal can be calibrated with an uncertainty  $\lesssim 0.03\%$  so that the uncertainty in obtaining thicknesses will only depend on the precision with which we can determine the point at which a particle passed through the crystal and on the thickness gradients. This condition should be obtainable from a heavy ion calibration with reasonable counting statistics. In figure 22 it can be seen that the thickness uncertainty is

FIGURE 24

Thickness contour map of D<sub>2</sub> scintillator. Thicknesses shown are differences from thickness at the center of the crystal. The nominal thickness of this crystal is 3 mm. Thickness gradients are also indicated.

D2 SCINTILLATOR THICKNESS VARIATION

CONTOUR INTERVAL =  $25 \mu\text{m}$   
GRADIENTS ARE IN  $\mu\text{m}/\text{mm}$   
NOMINAL THICKNESS = 3 mm



ORIGINAL PAGE IS  
OF POOR QUALITY

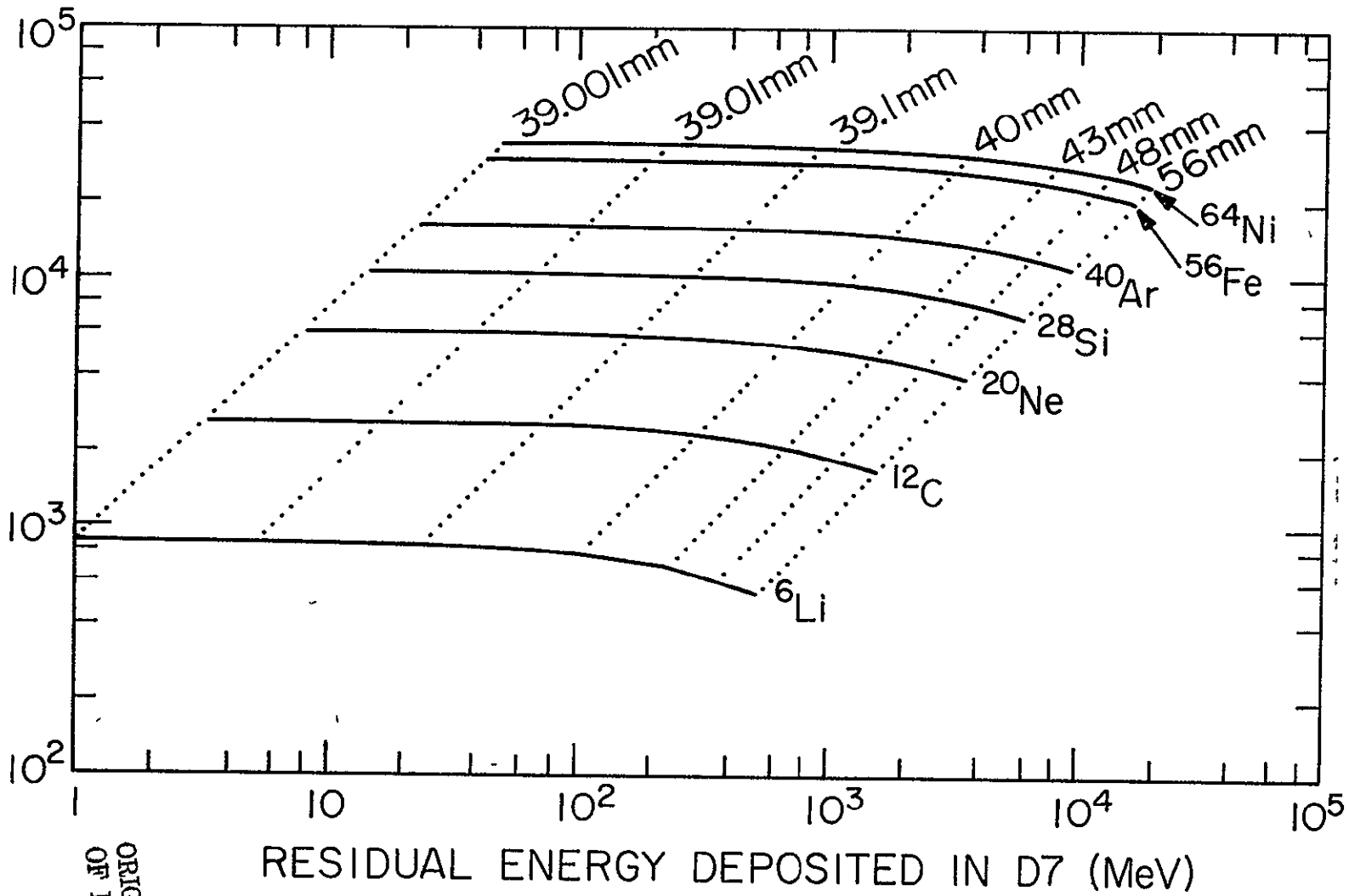
comparable to the uncertainty in  $L$  due to the finite angular resolution of the hodoscope.

Figure 25 shows the nominal response of the scintillators to various normally incident particles stopping in  $D_7$ . The maximum energy loss of interest in  $D_7$  is 20 GeV for normally incident particles and 22 GeV for particles incident at  $30^\circ$ . At low energies we should be able to detect particles which have penetrated only a small distance into  $D_7$ . Failure to detect such particles would cause them to be treated like particles which stopped in  $D_6$  and would introduce an error into our measurement of  $E'$ . If a particle were to penetrate  $10 \mu\text{m}$  into  $D_7$  and not be detected, a 0.6% error in our estimate of the energy loss in  $D_6$  ( $E'$ ) would result. This amount of material is a small fraction of the total thickness of the  $E'$  detector and therefore few particles will stop in this layer, so it is not unreasonable to exclude from analysis those particles which stop sufficiently near the boundary of two detectors that it is unclear in which detector they stopped. If we do exclude such events, the smallest signal of interest will be that produced by our  $\gamma$ -ray calibration sources, to be discussed later. The calibration source mounted on the  $D_7$  pm tube produces pulses approximately equivalent to an energy loss of 1.6 MeV in the  $D_7$  crystal. The overall dynamic range

FIGURE 25

Nominal  $\Delta E$  vs.  $E'$  tracks for normally incident particles stopping in D] are shown by solid lines. Lines of constant particle range are also shown (dotted).

TOTAL ENERGY LOSS IN D6 THROUGH D6 (MeV)



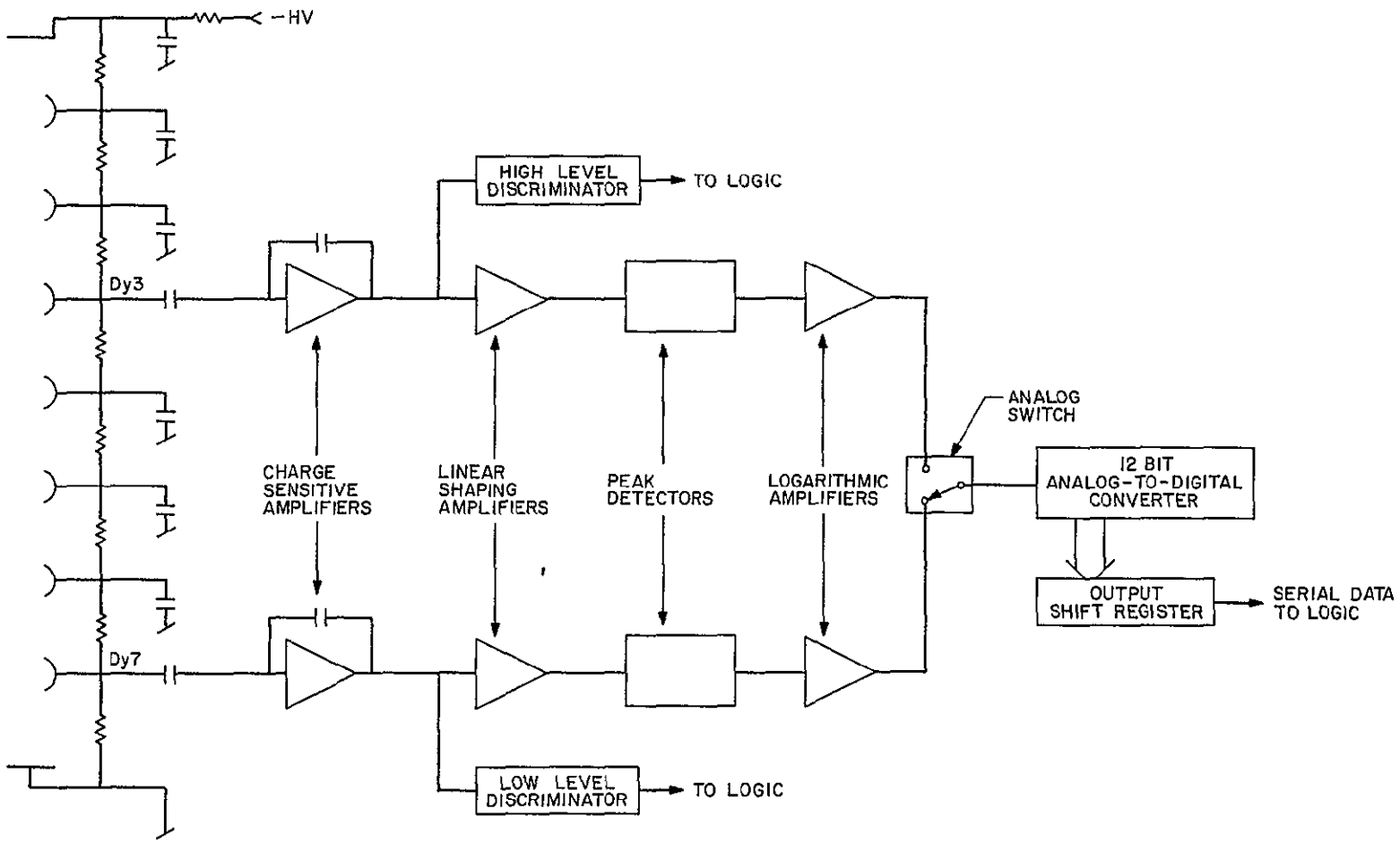
ORIGINAL PAGE IS  
OF POOR QUALITY

required in D7 (assuming no saturation of the scintillation at large energy losses) is  $\sim 1.4 \times 10^4$ .

Figure 2b shows the circuitry used to analyze the photomultiplier signals. Dynodes 8 through 11 of the photomultipliers are connected to the anode since for the large signals produced by heavy ions a large tube gain is not required. Signals from dynodes 3 and 7 are connected to separate amplifier chains. This arrangement is necessitated by the large range of energies deposited in the scintillators by the cosmic rays in which we are interested. The photomultiplier gain up to the stage being analyzed must be large enough so that electronic noise will not produce a large uncertainty in our energy measurements, even for the smallest signals of interest. However, we do not want to analyze signals from a dynode at which extreme space charge saturation is occurring. Due to the long decay time of the CsI(Tl) scintillation ( $\sim 1 \mu\text{sec}$ ) relatively large amounts of charge can be delivered to the dynode without saturation occurring. However, the onset of saturation occurs near the upper end of the range of pulse heights which we analyze on each dynode.

FIGURE 2b

Block diagram of pulse height analyzer  
circuitry.



ORIGINAL PAGE IS  
OF POOR QUALITY

Figure 27 illustrates the saturation characteristics of dynodes 3 and 7 in one of our photomultipliers. In this figure the ratio of the charge,  $Q$ , collected at the dynode of interest to the intensity of the light pulse,  $I$ , incident on the cathode of the tube is plotted as a function of  $Q$ . The tube was biased with 450 volts between the cathode and dynode 1 (for focusing purposes) and with 80 volts between each adjacent pair of dynodes up through the  $dy_7$ - $dy_8$  pair. Dynodes 8 through 11 were connected to the anode. This biasing arrangement yielded a ratio of 109 between the charges collected at  $dy_7$  and  $dy_3$  for a light input small enough so that  $dy_7$  exhibited no saturation. The cathode of the tube was illuminated by a light emitting diode (LED) pulsed in such a way as to produce an approximately exponentially decaying light pulse with a  $1 \mu\text{sec}$  time constant. The LED was placed at the focal point of a lens situated between the LED and the face of the photomultiplier. The lens served to produce an approximately parallel beam of light incident on the pm tube face. Between the lens and the tube face were inserted various combinations of neutral density filters for varying the light intensity. Each combination of filters used was calibrated using the pm tube response in the region where no space charge effects can be observed.

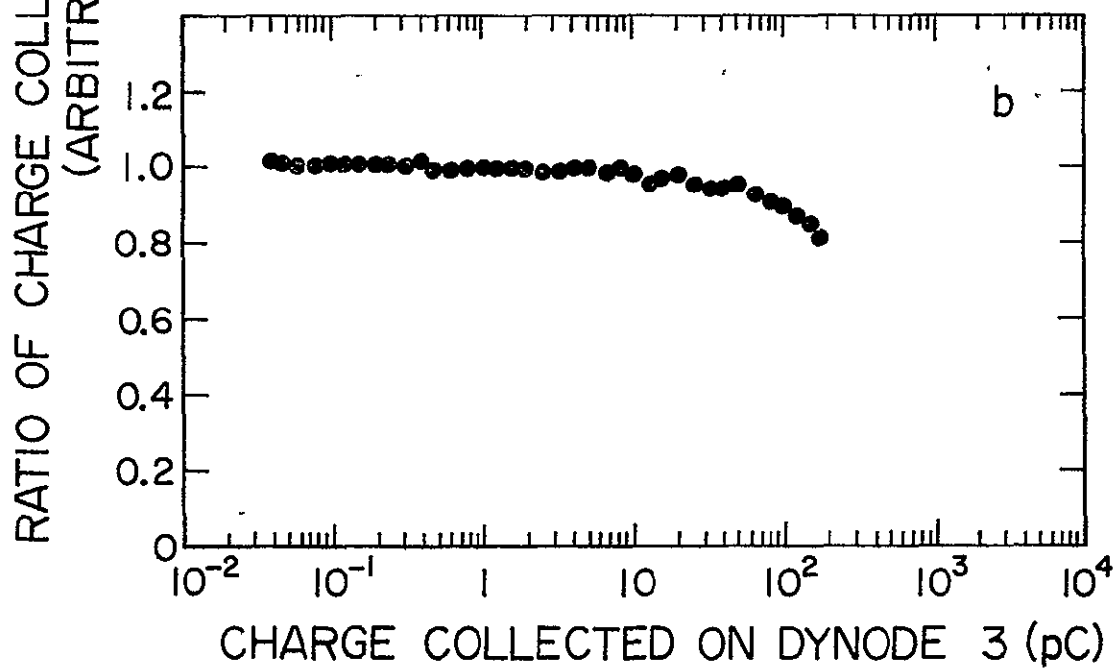
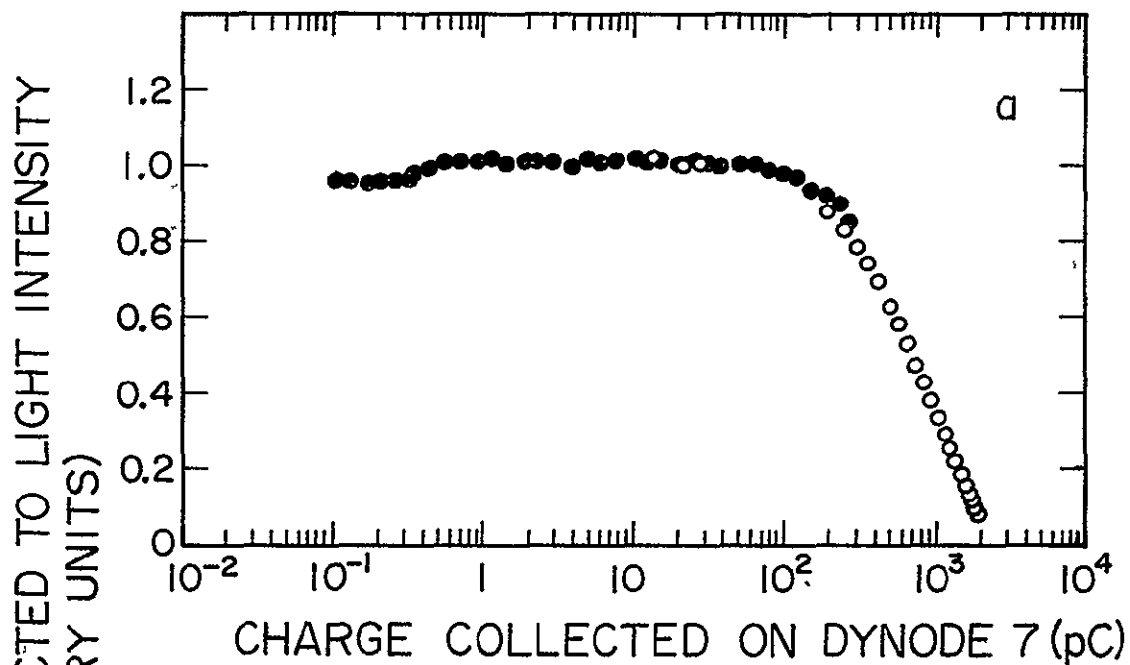
FIGURE 27

Saturation characteristics of EMI 9530R pm tube signals. The bias network used is discussed in the text. Uncertainties in the plotted points are dominated by systematic uncertainties in determining the light intensity incident on the pm tube cathode.

a) Saturation of signals measured on dynode 7. Open circles indicate data taken after set-up was modified to permit measurements at larger pulse heights.

b) Saturation of signals measured on dynode 3.

ORIGINAL PAGE IS  
OF POOR QUALITY



As can be seen in figure 27 the onset of space charge effects occurs at dynode 7 for a charge  $\sim 70$  pC and at dynode 3 for a charge  $\sim 10$  pC. This difference is probably the result of the large space charge density at later dynodes when dynode 3 is collecting charges  $\approx 10$  pC (when dynode 3 is collecting 10 pC, dynode 7 will be collecting  $\sim 550$  pC). It should be noted that we are able to operate our pm tubes with a certain degree of saturation without significantly degrading the performance of the instrument. Since we are using logarithmic pulse height analyzers to compress the signals, additional compression due to pm tube saturation can be tolerated if its effect is small compared to the logarithmic compression by the analyzers. Note, however, that pm tube saturation will complicate the interpretation of our pulse height measurements. In particular, a gain change (due, for example, to a change in the pm tube's temperature) will produce a different factor change in the observed signal size for pulses which cause pm tube saturation than for those which do not. We estimate that this effect will alter the pm tube temperature coefficient by  $\sim 10\%$  for the largest signals of interest.

The analog circuits used to analyze the pm tube signals have a dynamic range of approximately 100:1. Also, the voltage distributions on the dynodes yields a

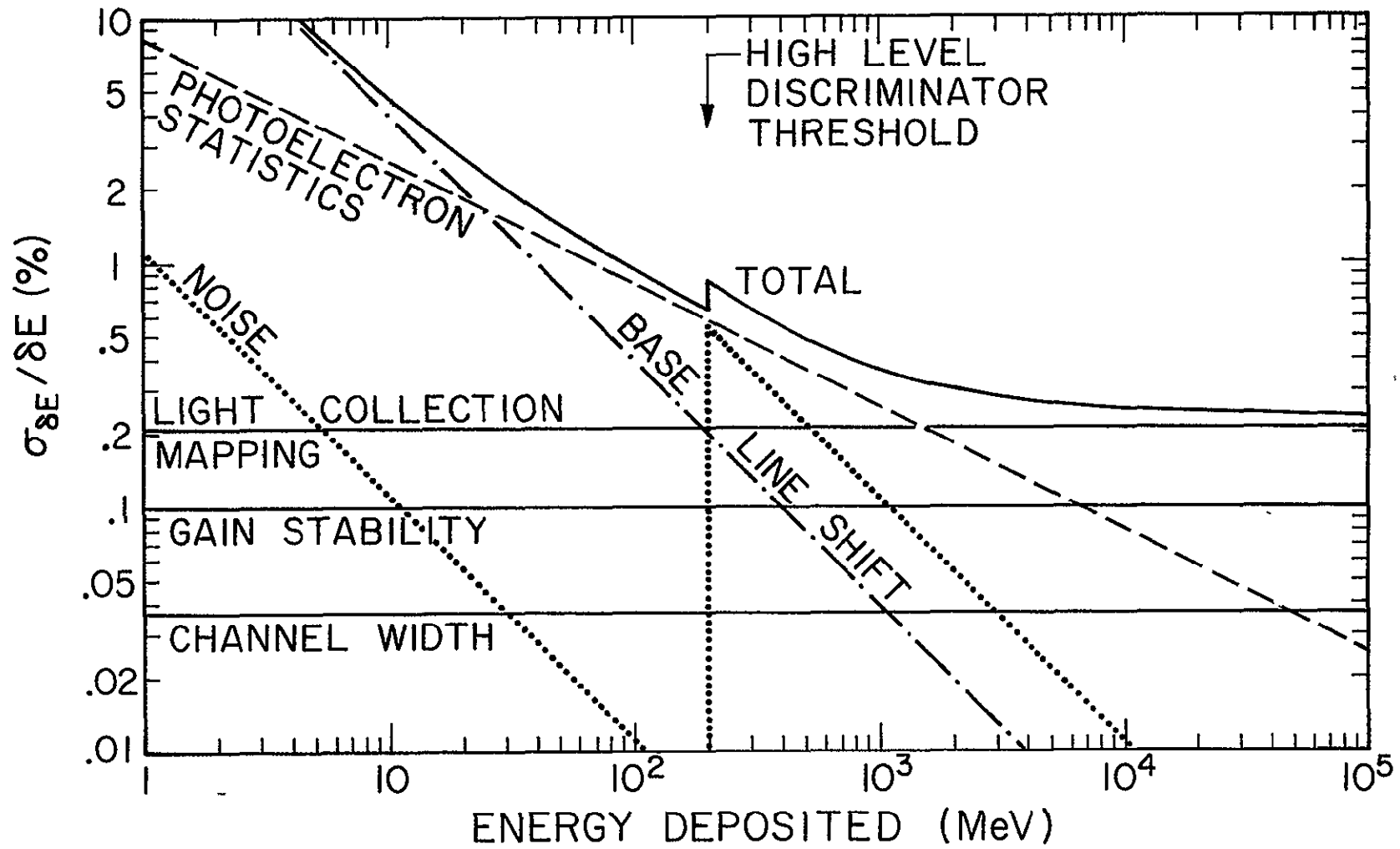
ratio  $\sim 100:1$  between the signals obtained from dynodes 7 and 3. On each dynode signals in the range 1 pC to 100 pC are analyzed, so that an overall dynamic range of  $\sim 10^4:1$  is obtained. Logic circuitry determines which of the two dynode signals will be pulse height analyzed based on whether the dynode 3 signal is large enough to trigger the discriminator. The pulse height analyzers have a logarithmic transfer function with an average channel width of 0.129%.

The process of detecting and encoding the energy losses in the scintillators involves the following steps: 1) production of light as ion-electron pairs produced by the passage of a charged particle are recombined, 2) transport of light from the point of production to the light pipe, 3) transport of light down the light pipe to the face of the pm tube, 4) production of photoelectrons as the light impinges on the photocathode, 5) gain by means of secondary emission at each of the dynodes, 6) amplification and shaping in the analog stages of the pulse height analyzer, 7) digitization in the analog-to-digital converter. Each of these stages introduces additional uncertainty into the measurement. The major sources of uncertainty are described in the following sections. Figure 28 shows the energy dependence of each of these sources of uncertainty in the energy

FIGURE 28

Energy measurement uncertainty in a single detector vs. energy deposited. Various contributions to the overall energy measurement uncertainty are also shown, as described in the text.

ORIGINAL PAGE IS  
OF POOR QUALITY



measurement. In addition the overall energy measurement uncertainty is shown.

The transport of photons to the photocathode and the production of electrons by photoelectric absorption and then by secondary emission constitute a chain of statistical processes. The compounding of the statistical errors in such a chain is treated in detail by Breitenberger (1955). The overall statistical uncertainty is dominated by the stage where the signal is being transported by the fewest carriers--that is by the production of photoelectrons at the cathode. The fractional uncertainty in the signal is approximately  $1/\sqrt{N}$ , where N is the number of carriers (photoelectrons) at this stage. We obtain a photoelectron yield of approximately 150 per MeV deposited in our scintillators. This estimate of the yield is uncertain by a factor of about 2. Thus photoelectron statistics lead to an energy measurement uncertainty

$$\frac{\sigma_{\delta E(\text{pe})}}{\delta E} \approx \frac{1}{\sqrt{150 \cdot \delta E}}$$

where  $\delta E$  is the energy loss in MeV in the scintillator of interest. In figure 28 we show this relationship of  $\sigma_{\delta E(\text{pe})}/\delta E$  to  $\delta E$ .

ORIGINAL PAGE IS  
OF POOR QUALITY

In order to interpret the signals measured by the pm tubes it is necessary to have a precise map of light collection efficiency vs. position in each of the scintillators. Such maps will ultimately be obtained from heavy ion calibrations at the BEVALAC at the Lawrence Berkeley Laboratory. Preliminary maps were made by looking at the amplitude variation of the photopeaks obtained using a collimated  $^{207}\text{Bi}$   $\gamma$ -ray source to illuminate selected areas of the crystal. Figure 29 shows light collection contours obtained in this manner. It is emphasized that although this map was obtained in a test configuration prior to assembly of the flight stack, we believe that the essential characteristics of this map are similar to those of the crystals in the flight stack. It can be seen from the figure that over more than 75% of the crystal area the light collection gradients are  $<0.2\%/mm$ , and increase to  $\sim 0.5\%/mm$  at the sides transverse to the light pipe's viewing direction.

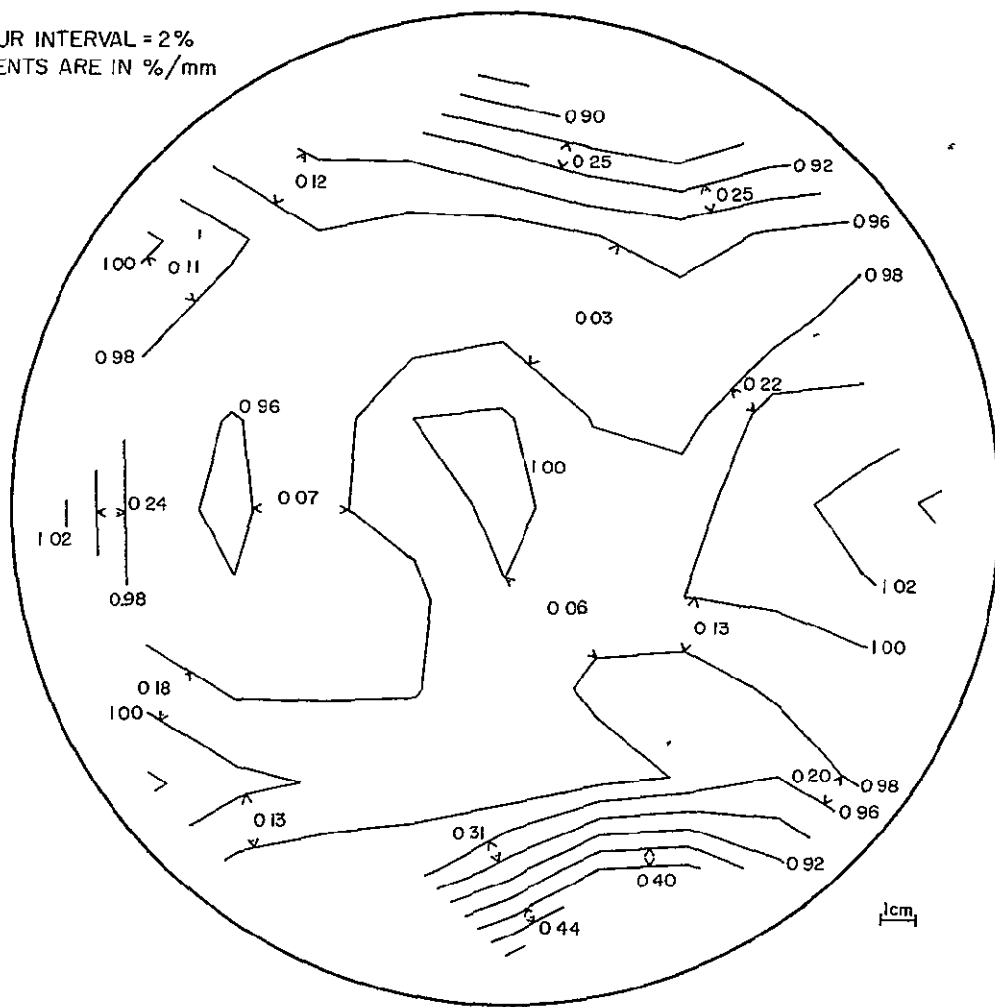
Since flight data must be corrected using light collection maps made during an accelerator calibration, and since the calibration and the flight may occur anywhere from several months to more than a year apart, it is essential that the response map not change over reasonably long periods of time. It is common in this type of experiment to use two or more photomultipliers to

FIGURE 29

Relative light collection efficiency contours measured using a collimated  $\gamma$ -ray source ( $^{207}\text{Bi}$ ) for D4 scintillator in a test set-up. Light collection gradients are also shown.

### LIGHT COLLECTION EFFICIENCY

CONTOUR INTERVAL = 2%  
GRADIENTS ARE IN %/mm



ORIGINAL PAGE IS  
OF POOR QUALITY

view a single scintillator and to sum the resulting charges at the input of a charge sensitive amplifier. However, as will be discussed below, photomultipliers exhibit gain variations with temperature. Furthermore, the detailed temperature characteristics of pm tubes vary between tubes of identical construction and even vary with time for any particular pm tube. Thus the relative weighting of the contributions from each tube to the overall response can change in an unknown manner and thereby alter the light collection map. In order to avoid this problem we have chosen to have only one pm tube viewing each scintillator. Gain changes in the tube will not affect the light collection of one area of the scintillator relative to another but rather will just cause an overall normalization error in the pulse heights. Techniques by which the normalization can be obtained during flight will be discussed later.

Since the light collection efficiency varies from point to point in the crystals, uncertainties in the energy loss measurement are produced due to uncertainties in the determination of a particle's trajectory. Light collection gradients of 0.2%/mm combined with a position uncertainty of 1 mm yield

$$\frac{\sigma_{\delta E(\text{light collection})}}{\delta E} \approx 0.002 .$$

The pulse height analyzer circuitry introduces several sources of uncertainty into our determination of the energy deposited in a scintillator. Random electronic noise in the linear amplifier stages is responsible for an uncertainty equivalent to an energy loss of 0.011 MeV in the low range of the pulse height analyzer and to an energy loss of 1.1 MeV in the high range, so we include a relative uncertainty of

$$\frac{\sigma_{\delta E(\text{noise})}}{\delta E} = \begin{cases} \frac{0.011 \text{ MeV}}{\delta E} & \delta E < 200 \text{ MeV} \\ \frac{1.1 \text{ MeV}}{\delta E} & \delta E > 200 \text{ MeV} \end{cases}$$

in our calculation of the overall energy measurement uncertainty. The various sources of background which stimulate the pm tubes (primarily the  $\gamma$ -ray calibration sources) cause the early stages of the pulse height analyzers to be continually active at a low signal level. Although these pulses are too small to trigger the discriminators they are capable of causing small base line shifts in the amplifiers. For the D7 scintillator, which is subject to the largest background, we measure

$$\frac{\sigma_{\delta E(\text{base line})}}{\delta E} \sim \frac{0.4 \text{ MeV}}{\delta E}$$

The analog-to-digital conversion introduces uncertainty in the energy measurement due to the finite channel width.

Our logarithmic analyzers have a channel width equal to 0.129% of the pulse height being measured, so we obtain

$$\frac{\sigma_{\delta E (c.w.)}}{\delta E} = \frac{0.00129}{\sqrt{12}} = 0.00037.$$

There are a number of systematic effects which will introduce significant errors if they cannot be eliminated by appropriate calibrations. The gain of the photomultipliers is subject to temperature variations as large as  $-0.8\%/^{\circ}\text{C}$ . However the pm tube gain is not a strictly reproducible function of temperature, so a knowledge of the pm tube temperature is not sufficient for making corrections to the pm tube gain. The scintillation efficiency of the CsI(Tl) crystals is also subject to temperature variations estimated to be  $\sim 0.1\%/^{\circ}\text{C}$  (Birks, 1964). The gain of the pulse height analyzers also exhibits a temperature dependence up to  $\sim 0.3\%/^{\circ}\text{C}$ .

Three types of in-flight calibrations are planned for purposes of correcting for these gain changes. Periodic pulser calibrations of the pulse height analyzers at a number of amplitudes should allow us to make corrections for any electronically produced variations in the signal sizes. In order to calibrate the photomultiplier gains a calibration source consisting of a small piece of CsI(Tl) and a  $2 \mu\text{Ci } ^{137}\text{Cs}$  source has been coupled directly to the

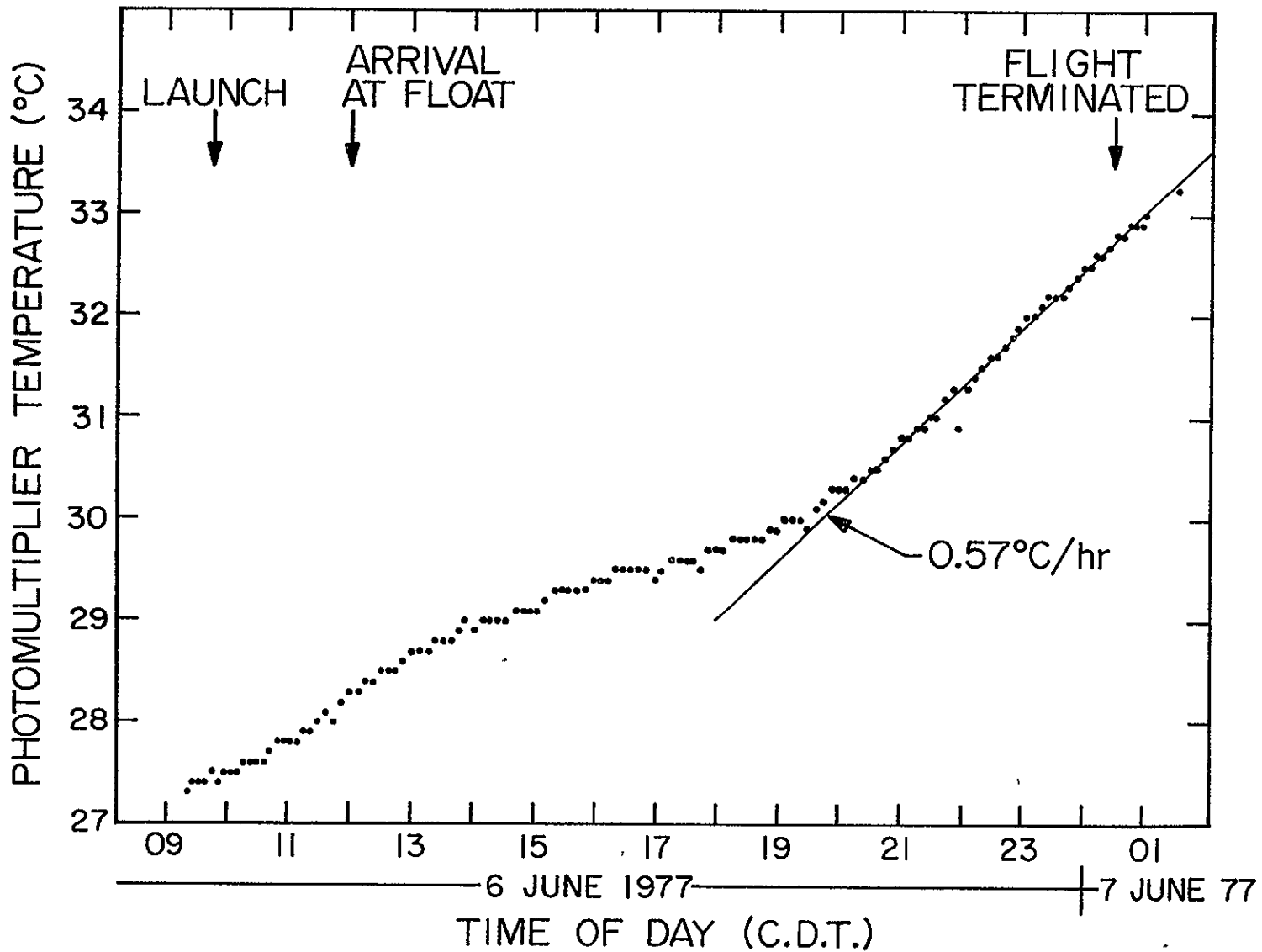
face of each pm tube. The logic is designed to periodically record non-coincident events, primarily  $\gamma$ -rays. Approximately 3000  $\gamma$ -ray pulse heights will be recorded per hour from each of the eight pm tubes. Fitting techniques should allow us to determine changes in the pm tube gains with a precision of a few tenths of a per cent about once per hour.

If such a calibration is to be sufficient it is essential that any variations of the pm tube temperature on time scales shorter than one hour be smooth. To produce this condition the pm tubes have been enclosed in thermally insulating boxes made of 2" thick slabs of polyethylene foam. Two thermistors have been mounted in contact with each pm tube to monitor the temperature variations seen by the tube. Figure 30 is a plot of the temperature measured at one of the pm tubes during a balloon flight of  $12\frac{1}{2}$  hours duration at float, launched from Aberdeen, South Dakota on 6 June 1977. The variation of the temperature was smooth and the maximum temperature gradient reached was  $0.57^{\circ}\text{C}/\text{hour}$ . This gradient combined with a photomultiplier temperature coefficient of  $0.8\%/^{\circ}\text{C}$  yields a variation of gain with time of  $0.5\%/hour$ .

FIGURE 30

Temperature variation of pm tubes during  
a balloon flight on 6 June 1977. The  
maximum temperature gradient is  
indicated.

ORIGINAL PAGE IS  
OF POOR QUALITY



Additional information on the variation of the scintillation efficiency and photomultiplier gains can be obtained from cosmic ray data itself. The logic assigns penetrating events--those which trigger the D8 scintillator (primarily relativistic carbon and oxygen)--a lower priority than stopping events. These events are read out only if no stopping event is available for readout. The expected penetrating rate ( $b \leq Z \leq 10$ ) is approximately 1500/hour. Landau fluctuations lead to an uncertainty of  $\sim 2-5\%$  in the energy loss of a relativistic carbon nucleus in the scintillators. So the mean signal produced by such particles should be obtained to  $\sim 0.1\%$  approximately once per hour. In estimating the uncertainty in our energy measurements we assume a rms gain uncertainty of  $0.1\%$  due to the limited precision of our gain calibration resulting from finite counting statistics, thus

$$\frac{\sigma_{\delta E(\text{gain shift})}}{\delta E} \approx 0.001$$

It can be seen in figure 28 that at low energy losses ( $\lesssim 25$  MeV) the energy measurement uncertainty is dominated by base line shift effects, at energies between  $\sim 25$  MeV and  $\sim 1.5$  GeV the uncertainty due to photoelectron statistics dominates, and at the energies above  $1.5$  GeV

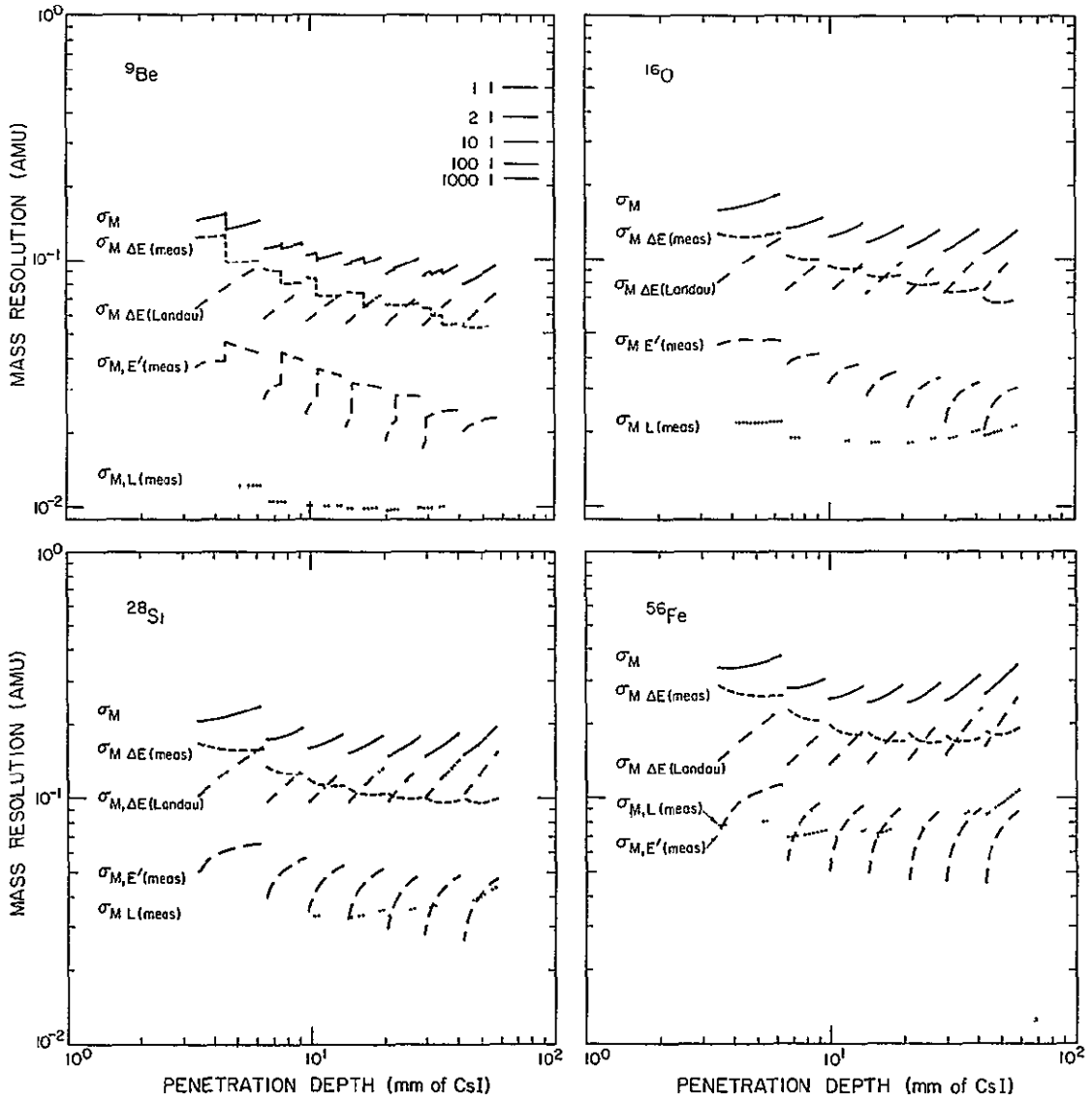
the uncertainty due to light collection variation with position dominates.

The energy measurement uncertainties described above apply separately to energy measurements in each of the scintillators through which a particle passes. So when we combine the energy loss measurements from several detectors to form  $\Delta E$  we must add the uncertainties in these measurements in quadrature to obtain the uncertainty in  $\Delta E$ . For those contributions to the energy measurement uncertainty which are proportional to the measured energy this compounding will reduce the magnitude of the contribution relative to that which would have been obtained in a single thick  $\Delta E$  detector. For contributions proportional to  $\sqrt{\delta E}$  the resulting uncertainty will be unchanged and for those which are independent of energy the uncertainty will be increased.

In figure 31 we show for the isotopes  ${}^9\text{Be}$ ,  ${}^{16}\text{O}$ ,  ${}^{28}\text{Si}$ , and  ${}^{56}\text{Fe}$  the mass resolution as a function of the depth to which the particle penetrates in the CsI(Tl) stack. These results are obtained by evaluating equation 5 using the partial derivatives in Table 1 and the uncertainties discussed in the preceding paragraphs. A  $15^\circ$  angle of incidence has been assumed in these calculations. In addition the contributions to the mass resolution due to

FIGURE 31

Mass resolution calculated for  $^9\text{Be}$ ,  $^{16}\text{O}$ ,  $^{28}\text{Si}$  and  $^{56}\text{Fe}$  incident at  $15^\circ$  as a function of depth of penetration ( $R/\sec\theta$ ) into the scintillator stack. Contributions due to uncertainties in measuring  $\Delta E$ ,  $E'$  and  $L$  are shown, as well as the contribution due to Landau fluctuations. The mass resolution required to separate adjacent isotopes with various relative abundances is indicated. The discontinuities in the  $^9\text{Be}$  curves are due to electronic noise near the high level discriminator threshold (see figure 28).



ORIGINAL PAGE IS  
OF POOR QUALITY

Landau fluctuations, thickness uncertainties, and uncertainties in the measurements of  $\Delta E$  and  $E'$  are shown. Tick marks on the right hand sides of these plots indicate the mass resolution required to obtain an inflection point between Gaussian distributions whose centers are separated by 1 AMU for various abundance ratios.

### 3. CALCULATIONS

Measurements of the isotopic composition of the cosmic rays are expected to place significant constraints on theories of the synthesis, acceleration and propagation of the cosmic rays. Such measurements should make it possible to refine estimates of astrophysical parameters which have been obtained from elemental abundances and should allow determination of additional parameters which cannot be obtained from elemental abundances alone. In section 3.1 we will briefly review the various classes of information which can be obtained from measurements of cosmic ray isotopic abundances. More detailed discussions of potential applications of isotopic composition measurements have been published by a number of authors (Meyer, 1975; Raisbeck et al., 1975a, 1975b; Shapiro and Silberberg, 1975b; Silberberg et al., 1976; Woosley, 1976). In section 3.2 we discuss the "leaky box model" of cosmic ray propagation and the assumptions upon which it is based. In section 3.3 we show how in the context of this model one can obtain cosmic ray source abundance ratios of isotopes of individual elements. We go on to evaluate the uncertainties in the ratios caused by uncertainties in various measurable parameters and we present curves which can be used to directly estimate source ratios and their uncertainties in several cases.

### 3.1 Information from Isotopic Composition

#### 3.1.1 Source Abundances

Theories of nucleosynthesis predict the relative abundances of large numbers of nuclides which will be synthesized under particular astrophysical conditions. From measurements of these abundances it is possible to derive values for important astrophysical parameters. In the case of the cosmic rays, however, abundance measurements have been largely restricted to the separation of individual elements, due to experimental difficulties in resolving isotopes. A great deal of information is lost if only elemental abundances can be measured. First, when the number of observed species is reduced, one's ability to stringently constrain the nucleosynthesis theories is diminished. Second, the influence of certain astrophysical parameters--for example, the neutron excess in the source--is strongly reflected in the synthesized isotopic abundances but only weakly in the elemental abundances. Consequently information concerning such parameters is largely obscured if only elemental abundances can be measured. Woosley (1976) has investigated the importance of measuring isotopic ratios among the iron peak elements for determining the degree of neutron enrichment of the

material from which these species were synthesized.

Furthermore, the elemental abundances observed at earth can be obtained from a wide range of isotopic source compositions. Therefore, it is necessary to measure the local isotopic composition in order to deduce the isotopic composition at the sources. In fact, there are cases where the isotopic composition must be measured in order to obtain even the elemental composition at the sources. For example, in a cosmic ray source composed of solar-like material, the calcium will be composed almost entirely of  $^{40}\text{Ca}$ . However the spallation of  $^{56}\text{Fe}$  would produce substantial amounts of secondary  $^{41}\text{Ca}$ ,  $^{42}\text{Ca}$ ,  $^{43}\text{Ca}$  and  $^{44}\text{Ca}$  as well as  $^{40}\text{Ca}$ . As a result, the observed calcium would be approximately half primary and half secondary in origin. On the other hand, if one can observe the isotope  $^{40}\text{Ca}$  alone, then one will be dealing with a primary-to-secondary ratio in excess of 5-to-1.

Additional motivation for the measurement of the isotopic composition of the cosmic rays has been provided by the suggestion of several authors that the cosmic rays are subject to elemental separation effects prior to being accelerated. Evidence has been presented (Cassé et al., 1975a; Cassé and Goret, 1977b) which suggests that the differences in elemental composition between the cosmic

rays and solar system material could be predominantly due to such selective acceleration effects. The relative abundances of the various isotopes of a particular element will not be affected by such charge dependent selection mechanisms. It is therefore desirable to use measurements of the isotopic composition of individual elements as a source of information which will not be altered by charge-dependent separation effects.

### 3.1.2 Secondary Production and Propagation

Much of the present knowledge regarding the propagation of the cosmic rays through the interstellar medium has been derived from the abundances of those elements which are believed to be absent at the cosmic ray sources. Due to lack of detailed information concerning the interaction of the cosmic rays with the electromagnetic fields in the propagation medium and of the boundary conditions appropriate for describing this medium, the propagation of cosmic rays has generally been treated by assuming a distribution of path-lengths through which the particles have passed during transport from their sources to the point of observation. If the path-length distributions described by such a model can be characterized by a single parameter (for example, the

thickness of a slab or the characteristic length of an exponential distribution) then it is possible to evaluate this parameter by using available nuclear fragmentation cross sections and the observed abundances of a single purely secondary species and of its progenitors. Once the path-length distribution is known, it becomes possible to calculate the secondary contributions to other species and then to obtain the primary contribution by subtracting the secondaries from the observed abundance. The source abundances can then be obtained by applying corrections for the nuclear destruction of these particles in passing through interstellar matter.

If, in applying this technique to determine the primary component of a particular element, one must use only elemental abundances, then it may be necessary to utilize an element relatively far from the element of interest as the tracer of secondary production. The elements below iron which are believed to be entirely of secondary origin are the light elements Li, Be, and B and the elements Sc, V and Mn in the iron group, plus the elements F and Cl. There are no elements which are obviously of purely secondary origin near some of the elements which one would like to investigate, for example Mg. A path-length derived from the light elements will reflect the spallation of carbon and oxygen, while a

path-length derived from the iron group elements will reflect the spallation of iron. The secondary magnesium, however, is produced predominantly by spallation of Si and S. So one is forced to make an additional assumption--for example, that the distribution of path-lengths is the same for all species--in order to obtain abundances of many elements at the cosmic ray sources.

In cases where isotopic abundances can be measured it is possible to avoid this difficulty. Many of the even-Z elements have one or more isotopes which should be of purely secondary origin. By using a secondary isotope of the element for which we want to obtain source abundances as a tracer of the secondary production during propagation, we obtain a correction which is appropriate for this element.

### 3.1.3 Radioactive Species

Various information can be obtained from radioactive species in the cosmic rays (Soutoul et al., 1975; Raisbeck et al., 1975a, 1975b). Isotopes which  $\beta$ -decay with half lives  $\sim 10^6$ - $10^7$  years can be used as a measure of the time since their production. If these isotopes are not produced at the cosmic ray sources one obtains a measure of the residence time of cosmic rays in the galaxy

(as determined by the rate of loss due to nuclear destruction and the escape from the galaxy). From  $\beta$ -unstable species which are predominantly of primary origin one obtains a measure of the time since synthesis of these nuclei in the sources. Unfortunately in the region  $Z \leq 28$  most  $\beta$ -decay nuclei are not expected to be produced in the cosmic ray sources. Possible exceptions are  $^{60}\text{Fe}$  and  $^{56}\text{Ni}$  (Waddington, 1975). However, these species have rather short half lives compared to present estimates (Hagen et al., 1977; Garcia-Munoz et al., 1977b; Müller et al., 1977; Webber et al., 1977) of the residence time of cosmic rays in the galaxy of  $\approx 10^6$  years (for  $^{60}\text{Fe}$   $\tau_{1/2} = 3 \times 10^5$  yr and for  $^{56}\text{Ni}$   $\tau_{1/2}$  is estimated to be  $\sim 2 \times 10^5$  yr (Cassé, 1973) when the absence of orbital electrons precludes the possibility of electron capture decay). Thus these nuclei should only be of value above several GeV/nuc where time dilation will extend the effective life time to  $\sim 10^6$  years.

Nuclei which can only decay by means of orbital electron capture can be used as probes of various astrophysical conditions. Those electron capture nuclides which are synthesized in the source region can be used to measure the time between synthesis and acceleration to relativistic energies (Cassé and Soutoul, 1975b; Soutoul et al., 1975; Soutoul et al., 1977) since only during

this time are they expected to have orbital electrons available for capture. Electron capture nuclei which are entirely of secondary origin will probe the density in the propagation medium since after picking up an orbital electron from the interstellar gas the nucleus will decay only if a time comparable to its electron capture half life can elapse before encountering an atom of the gas and undergoing an interaction which will re-strip the electron from the nucleus.

In most cases, measurements of elemental abundances are of little use in addressing these questions of the survival or decay of radioactive isotopes. Other isotopes of the same elements generally have significant abundances and the difference between complete survival and complete decay of the radioactive isotope may only be a few tenths of the observed elemental abundance. Uncertainties in the abundances of parent nuclei, in nuclear fragmentation cross sections and in estimates of the path-length in the interstellar medium can easily obscure differences of this magnitude.

### 3.2 Cosmic Ray Propagation -- Leaky Box Model

As mentioned above, various simplified models of the propagation of cosmic rays between their production and their arrival at earth have been used for unfolding the cosmic ray source composition from the effects of spallation during propagation. Of these models, the "leaky box model" (introduced by Cowsik et al., [1967]) is particularly appealing both because it can be obtained from a transport equation by invoking a number of simple, physically reasonable assumptions and because it has been applied with considerable success to observations of elemental abundances. In this section we will briefly review the leaky box model and the assumptions on which it is based.

The propagation of cosmic rays can be described by the transport equation (Gloeckler and Jokipii, [1969; Meneguzzi et al., [1971])

$$\frac{\partial n_i}{\partial t} - \vec{\nabla} \cdot [k \vec{\nabla} n_i] - \frac{\partial}{\partial E} \left[ \left( \frac{dE}{dt} \right)_i n_i \right] = C_i - D_i$$

In this equation  $n_i(\vec{r}, E, t)$  is the number per unit volume per unit energy per nucleon of particles of species  $i$  at position  $\vec{r}$ , energy per nucleon  $E$ , and time  $t$ . The left hand side describes local changes in this density due to change of position and energy, while the right hand side

describes changes of a non-local character (i.e., not described by a differential operator) which are due to creation ( $C_i$ ) and destruction ( $D_i$ ) of particles. The creation term,  $C_i$ , is used to describe the production of particles of species  $i$  in the cosmic ray sources and by spallation of heavier species, while the destruction term,  $D_i$ , describes the destruction of particles by inelastic nuclear interactions with the interstellar gas and by radioactive decay. This equation assumes that the spatial transport of cosmic rays is a diffusive process (presumably resulting from the scattering of particles by irregularities in the galactic magnetic field) and that the cosmic rays are isotropic.\*

Due to our lack of knowledge concerning the spatial distribution of cosmic ray sources and of interstellar magnetic fields and gas we assume, the diffusion coefficient,  $\kappa$ , the rate of energy loss,  $(dE/dt)_i$ , and the rates of particle creation,  $C_i$ , and destruction,  $D_i$ , are independent of position. Then the spatial dependence

---

\* Measurements of cosmic ray anisotropies at energies of  $10^{11}$  eV yield values  $< 2 \times 10^{-4}$  (see, for example, Elliot et al., 1970). At lower energies it is only possible to set an upper limit on the galactic cosmic ray anisotropy from measurements made near earth since interactions with the solar wind can produce local anisotropies in excess of the galactic value.

of  $n_i$  can only arise from the boundary conditions on this equation, which are yet to be specified. In the leaky box model it is assumed that the boundary of the confinement volume acts as a surface which reflects most of the particles incident upon it, but has a small probability of letting a particle escape from the volume.

It is conventional to make the additional assumption that the diffusion term in the transport equation can be neglected. In this case  $n_i$  is treated as a constant throughout the confinement region and the loss of particles at the boundary is accounted for by the inclusion of a position independent probability of loss per unit time in the term  $D_i$ . By making these approximations one obtains

$$\frac{\partial n_i}{\partial t} = \frac{\partial}{\partial E} \left[ \left( \frac{dE}{dt} \right)_i n_i \right] + C_i - D_i .$$

This approximation can be justified if the cosmic rays move freely about the confinement volume, encountering its surface many times before finally escaping. The typical amount of material traversed by cosmic rays before escaping is  $\sim 5.5 \text{ g/cm}^2$ , as deduced from measurements of the abundances of purely secondary cosmic rays relative to their primary progenitors (for example,  $\text{Li} + \text{Be} + \text{B}/\text{C} + \text{N} + \text{O}$ ). For an interstellar density of 1

H atom and  $0.1$  He atoms per  $\text{cm}^3$ , this amount of material corresponds to a distance of  $800$  kpc (approximately  $100$  times the distance between the sun and the galactic center). Since the various regions suggested for the confinement of the cosmic rays have scale sizes on the order of the galactic radius or smaller, it should be possible to neglect spatial gradients if the cosmic rays are not strongly scattered while traversing the confinement region. We should note that there are indications (Cesarsky et al., 1977) that there may be a significant gradient of cosmic ray density in our galaxy. If these results are borne out by further observations, it will be necessary to consider the confinement of cosmic rays in a region small compared to the size of the galaxy if the leaky box model is to be retained in its present formulation.

Next we assume that a steady state has been established so that we can set  $\partial n_i / \partial t = 0$  to give

$$0 = \frac{\partial}{\partial E} \left[ \left( \frac{dE}{dt} \right)_i n_i \right] + C_i - D_i .$$

The major energy changing process affecting cosmic ray nuclei is ionization energy loss due to collision with electrons in the interstellar gas. Thus we write

$$\left(\frac{dE}{dt}\right)_i = \frac{Z_i^2}{M_i} S(E) \beta c \rho,$$

where  $\rho$  is the density ( $\text{g/cm}^3$ ) of the interstellar gas and the other symbols have been defined in section 2 of this thesis. Note that although ionization energy loss is actually the result of a large number of discrete collisions, we can approximate it by a continuous rate of energy loss since other relevant length scales are much larger than the typical distance between collisions with interstellar electrons. For example, a particle with  $\gamma=2$  ( $E/M=931$  MeV/nuc) loses 90% of its energy in collisions which transfer less than 150 keV to an interstellar electron (Rossi, 1952). The particle's rate of specific ionization will be no less than  $4.1$  MeV/( $\text{g/cm}^2$ ) (the minimum  $dE/dx$  for a proton), so on the average it will travel no farther than  $35$   $\text{mg/cm}^2$  before losing 150 keV. This distance is to be compared with nuclear interaction lengths which range between 2 and 8  $\text{g/cm}^2$  and the escape mean free path of  $\sim 5.5$   $\text{g/cm}^2$ . Note also that the maximum energy which a heavy particle with  $\gamma=2$  can transfer to a free electron is  $\sim 3$  MeV. Such collisions are rare, but energy losses of this size will not significantly alter either the ionization rate or the nuclear interaction cross sections for particles at the energies being considered here.

The term,  $D_i$ , which accounts for the destruction of particles of species  $i$  can be written as (Meneguzzi et al., 1971)

$$D_i = (n_H \sigma_{pi} + n_{He} \sigma_{\alpha i}) \beta c n_i + \frac{n_i}{\tau_{esc}} + \frac{n_i}{\gamma \tau_i} \quad (7)$$

where  $n_H$  and  $n_{He}$  are the number densities of H and He, respectively, in the interstellar medium,  $\sigma_{pi}$  and  $\sigma_{\alpha i}$  are the cross sections for breakup of species  $i$  in a collision with an interstellar H or He nucleus, respectively,  $\tau_{esc}$  is the mean time for escape from the confinement volume, and  $\tau_i$  is the mean time for radioactive decay in the frame in which the particle is at rest ( $\tau_i \rightarrow \infty$  for stable species). The three terms on the right hand side of equation 7 represent loss by means of nuclear destruction, escape from the confinement region and radioactive decay, reading from left to right.

The creation term,  $C_i$ , is written

$$C_i = Q_i + \sum_j \int_0^\infty n_j(E') \left[ n_H \sigma_{pj i}(E, E') + n_{He} \sigma_{\alpha j i}(E, E') \right] \beta c dE'$$

where  $Q_i$  is the rate of production (per unit volume, per unit energy per nucleon) of cosmic rays of species  $i$  by the cosmic ray sources and  $\sigma_{pj i}(E, E')$  and  $\sigma_{\alpha j i}(E, E')$  are the cross sections for species  $j$  at energy per nucleon  $E'$  to produce species  $i$  at energy per nucleon  $E$  in a

collision with interstellar H or He, respectively. There is evidence (Greiner et al., 1975) that at the energies of interest here ( $\approx 100$  MeV/nuc) spallation products are predominantly produced with velocity (or energy per nucleon) nearly equal to that of the incident heavy nucleus. Therefore we obtain

$$C_i = Q_i + \sum_j n_j [n_H \sigma_{pji}(E) + n_{He} \sigma_{\alpha ji}(E)] \beta c .$$

It is convenient to replace the cosmic ray density  $n_i$  by the omnidirectional flux,  $\phi_i = n_i \beta c / 4\pi$ , and to define  $q_i \equiv Q_i / (n_H M_H + n_{He} M_{He})$ . We obtain

$$0 = -\frac{\phi_i}{\Lambda_{esc}} - \frac{\sigma_{pi} + (n_{He}/n_H) \sigma_{\alpha i}}{M_H + (n_{He}/n_H) M_{He}} \phi_i + \frac{Z_i^2}{M_i} \frac{d}{dE} (S(E) \phi_i) + q_i + \sum_j \phi_j \left[ \frac{\sigma_{pji} + (n_{He}/n_H) \sigma_{\alpha ji}}{M_H + (n_{He}/n_H) M_{He}} \right] . \quad (8)$$

In this equation we have written  $\Lambda_{esc} = \xi \beta c \tau_{esc}$  and we have assumed that we are not dealing with any radioactive species, so we can neglect destruction by radioactive decay. Equation 8 is the basic equation relating observed cosmic ray fluxes ( $\phi_i$ ) to source abundances ( $q_i$ ) in the leaky box model.

To simplify notation we will make the following definitions:

$$\frac{1}{\Lambda_{NDi}} \equiv \frac{\sigma_{\rho i} + (n_{He}/n_H)\sigma_{\alpha i}}{M_H + (n_{He}/n_H)M_{He}},$$

$$\hat{S}_i \equiv \sum_j \phi_j \left[ \frac{\sigma_{\rho ji} + (n_{He}/n_H)\sigma_{\alpha ji}}{M_H + (n_{He}/n_H)M_{He}} \right]$$

Then we obtain

$$0 = -\phi_i \left( \frac{1}{\Lambda_{esc}} + \frac{1}{\Lambda_{NDi}} \right) + \frac{Z_i^2}{M_i} \frac{d}{dE} (S(E)\phi_i) + q_i + \hat{S}_i \quad (9)$$

### 3.3 Secondary Tracer Formalism

We will now specialize to the case of the various isotopes of a single element. Thus we will drop the subscript on the nuclear charge,  $Z$ , in equation 9. Note that in equation 9 the  $\phi_i$  are the cosmic ray fluxes measured in local interstellar space and the "secondary source term",  $\hat{S}_i$ , depends only on these fluxes and on nuclear cross sections. Thus the only quantities in equation 9 which we cannot directly measure are the source abundances,  $q_i$ , and the "escape mean free path",  $\Lambda_{esc}$ . If we know that a particular species is not produced in the cosmic ray sources ( $q_i=0$ ) then we can obtain  $\Lambda_{esc}$  in terms of measurable quantities (Reames, 1974),

$$\frac{1}{\Lambda_{esc}} = \frac{\hat{S}_i}{\phi_i} - \frac{1}{\Lambda_{NDi}} + \frac{Z^2}{M_i} \frac{1}{\phi_i} \frac{\partial}{\partial E} (S(E)\phi_i).$$

If we substitute this value of  $\Lambda_{esc}$  obtained from species  $i$  into equation 9 written for species  $j$ , we obtain

$$q_j = \left(\frac{\phi_j}{\phi_i}\right) \hat{S}_i - \hat{S}_j + \left(\frac{\phi_j}{\phi_i}\right) \frac{Z^2}{M_i} \frac{\partial}{\partial E} (S(E)\phi_i) - \frac{Z^2}{M_j} \frac{\partial}{\partial E} (S(E)\phi_j) - \left(\frac{1}{\Lambda_{NDi}} - \frac{1}{\Lambda_{NDj}}\right) \phi_j \quad (10)$$

This equation can be simplified by approximating  $\phi_i$ ,  $\phi_j$  and  $s(E)$  in the vicinity of the energy of interest,  $E_0$ , by power laws:

$$\phi_i(E) = \phi_i(E_0) \left(\frac{E}{E_0}\right)^{-\gamma_i}, \quad \phi_j(E) = \phi_j(E_0) \left(\frac{E}{E_0}\right)^{-\gamma_j}, \quad S(E) = S(E_0) \left(\frac{E}{E_0}\right)^{-\alpha}$$

Then the ionization energy loss terms reduce to

$$\begin{aligned} & \left(\frac{\phi_j}{\phi_i}\right) \frac{Z^2}{M_i} \frac{\partial}{\partial E} (S(E)\phi_i) - \frac{Z^2}{M_j} \frac{\partial}{\partial E} (S(E)\phi_j) \\ & = -\frac{Z^2}{M_j} \left(\frac{S(E_0)}{E_0}\right) \left(\frac{M_j}{M_i} (\gamma_i + \alpha) - (\gamma_j + \alpha)\right) \phi_j \quad (11) \end{aligned}$$

Substituting 11 into 10 yields

$$q_j = \frac{\phi_j}{\phi_i} \hat{S}_i - \hat{S}_j - \left[ \frac{1}{\Lambda_{NDi}} - \frac{1}{\Lambda_{NDj}} + \frac{Z^2}{M_j} \frac{S(E)}{E} \left(\frac{M_j}{M_i} (\gamma_i + \alpha) - (\gamma_j + \alpha)\right) \right] \phi_j$$

We can write the analogous expression for the source abundance,  $q_k$ , of a third species, and the ratio of source

abundances can be written in the form:

$$\frac{q_i}{q_k} = \frac{\phi_j}{\phi_k} \left\{ \frac{1 - \frac{\phi_i}{\phi_j} \frac{\hat{S}_j}{\hat{S}_i} + \left[ \frac{1}{\Lambda_{NDj}} - \frac{1}{\Lambda_{NDi}} + \frac{Z^2}{M_j} \frac{S(E)}{E} \left( \alpha \left( \frac{M_i - M_j}{M_i} \right) + \gamma_j - \frac{M_j}{M_i} \gamma_i \right) \right] \frac{\phi_i}{\hat{S}_i}}{1 - \frac{\phi_i}{\phi_k} \frac{\hat{S}_k}{\hat{S}_i} + \left[ \frac{1}{\Lambda_{NDk}} - \frac{1}{\Lambda_{NDi}} + \frac{Z^2}{M_k} \frac{S(E)}{E} \left( \alpha \left( \frac{M_i - M_k}{M_i} \right) + \gamma_k - \frac{M_k}{M_i} \gamma_i \right) \right] \frac{\phi_i}{\hat{S}_i}} \right\} \quad (12)$$

The right hand side of equation 12 depends only on measurable quantities (local interstellar cosmic ray fluxes, spectral indices and nuclear cross sections). Below we will discuss the degree of precision to which these quantities must be known in order to obtain useful estimates of the ratio of source abundances  $q_j/q_k$ .

In evaluating equation 12 we employ fragmentation cross sections obtained from the semi-empirical formulas of Silberberg and Tsao (1973a) with modifications given by Silberberg et al. (197b). Total inelastic cross sections are obtained using the formulas (Tsao and Silberberg, 1975; Cheshire et al., 1974):

$$\sigma_{pi} = 54 \text{ mb } M_i^{2/3} (1 - 0.47 M_i^{-0.4}),$$

$$\sigma_{\alpha i} = 45 \text{ mb } (M_i^{1/3} + 4^{1/3})^2.$$

Notice that in evaluating equation 12 we require ratios of the fluxes of parent species (used in calculating  $\hat{S}_i$ ,  $\hat{S}_j$  and  $\hat{S}_k$ ) to the fluxes of the isotopes under consideration. However, at present, only elemental abundance ratios are available. For this reason we shall assume that the three isotopes of interest constitute the entire local abundance of the element being considered. This is an adequate approximation in all the cases which we shall examine if the source abundances are not vastly different from the solar system abundances. This assumption will not be a limitation when isotopic abundance observations of the elements which we are considering become available, since it will then be possible to appropriately renormalize the elemental abundances.

Note that the secondary tracer technique for obtaining source abundance ratios can only be applied in the case of elements having an isotope which is believed to be absent at the cosmic ray sources. Among such elements there are several which are of considerable importance for the theory of nucleosynthesis, for example S, Ar and Ca (Cassé and Meyer, 1977a).

ORIGINAL PAGE IS  
OF POOR QUALITY

## 3.3.1 Analysis of Uncertainties -- Motivation

Before beginning a detailed treatment of the effect of uncertainties in the measured quantities in equation 12 on the deduced source ratio we wish to motivate this treatment by means of a semi-quantitative discussion of a simplified case. For this purpose we shall make the following assumptions: 1) ionization energy loss is negligible ( $s(E)=0$ ), 2) the total inelastic cross sections for the species of interest are equal ( $\Lambda_{NDi} = \Lambda_{NDj} = \Lambda_{NDk}$ ), 3) isotope k is significantly more abundant in the local cosmic rays than species j or i ( $\phi_k \gg \phi_j \approx \phi_i$ ), 4) the observed flux of species j is largely secondary in origin while that of species k is largely primary in origin, and 5) cross sections for species i, j and k to make one another are negligible. Using assumptions (1) and (2) we can reduce equation 12 to

$$\frac{q_j}{q_k} = \frac{\phi_j - \phi_i (\hat{S}_j / \hat{S}_i)}{\phi_k - \phi_i (\hat{S}_k / \hat{S}_i)} .$$

Assumption (4) allows us to write

$$\frac{q_j}{q_k} = \frac{\phi_j}{\phi_k} - \frac{\phi_i}{\phi_k} \left( \frac{\hat{S}_j}{\hat{S}_i} \right)$$

This expression illustrates the difficulties involved in obtaining precise values of cosmic ray source ratios. The assumption that the observed flux of species j is largely

of secondary origin implies that the difference of the two terms on the right hand side of this equation is significantly less than either of these two terms individually. Therefore a small relative error in either of these two terms will translate into a relative error in  $q_j/q_k$  which is larger by a factor of approximately  $(\phi_j/\phi_k)/(q_j/q_k)$ .

In order to make this discussion more precise, we can calculate the uncertainty in the calculated source ratio due to uncertainties in the measurement of the local fluxes  $\phi_i$ ,  $\phi_j$  and  $\phi_k$  and in the determination of the secondary correction factor,  $R \equiv (\hat{S}_j/\hat{S}_i)$ . To simplify the notation we will write  $r_{jk} = \phi_j/\phi_k$ ,  $r_{ik} = \phi_i/\phi_k$  and  $\alpha_{jk} = q_j/q_k$ . Our assumptions (3) and (5) allow us to treat  $r_{jk}$ ,  $r_{ik}$  and  $R$  as statistically independent. We obtain

$$\left(\frac{\sigma_{\alpha_{jk}}}{\alpha_{jk}}\right)^2 = \left(\frac{\sigma_{r_{jk}}}{r_{jk}}\right)^2 \left(\frac{r_{jk}}{\alpha_{jk}}\right)^2 + \left[\left(\frac{\sigma_{r_{ik}}}{r_{ik}}\right)^2 + \left(\frac{\sigma_R}{R}\right)^2\right] \left(\frac{r_{jk}}{\alpha_{jk}} - 1\right)^2$$

If we now use assumptions (3) and (4) and also assume that the uncertainties in the observed fluxes are entirely statistical and given by  $\sigma_{r_{ik}} = \sqrt{r_{ik}/N}$  and  $\sigma_{r_{jk}} = \sqrt{r_{jk}/N}$ , we can write

$$\frac{\sigma_{\alpha_{jk}}}{\alpha_{jk}} = \frac{r_{jk}}{\alpha_{jk}} \sqrt{\frac{1}{N} \left( \frac{1}{r_{jk}} + \frac{1}{r_{ik}} \right) + \left( \frac{\sigma_R}{R} \right)^2}$$

where  $N$  is the observed number of events of species  $k$  (and

approximately equal to the combined total number of events of species  $i$ ,  $j$  and  $k$ ). This expression explicitly shows the magnification of both the statistical errors in the measured fluxes and the errors in the calculated quantity  $R$  by a factor of  $r_{jk}/\alpha_{jk}$  which is likely to be  $\approx 5$  for most of the cases examined below.

### 3.3.2 Source Ratio Uncertainties

We now wish to consider in detail the effects of uncertainties in the measurable quantities--local fluxes, spectra and nuclear cross sections--on the uncertainty in the source abundances that we derive using the secondary tracer technique. By so doing it is possible to identify those areas in which more precise measurements can improve our ability to derive cosmic ray source abundances.

For purposes of this discussion we restrict our attention to a particular set of possible source abundances. In particular, we use the elemental source ratios obtained by Silberberg et al. (197b) from available cosmic ray elemental abundance measurements near earth and from the assumption that the propagation is described by an exponential distribution of path-lengths. We follow their procedure (Tsao et al., 1973; Shapiro et al., 1975a) of distributing the source abundance of each

element among its stable isotopes in proportion to the solar system abundances compiled by Cameron (1973). We then set the source abundance of the isotopes which we are using as tracers to zero. Table 7 lists the resulting source abundances. For the tracer isotopes we indicate in parentheses the source abundances which we had before setting these abundances to zero.

The source abundances are then propagated through an exponential path-length distribution with  $\Lambda_{esc} = 5.5 \text{ g/cm}^2$  in a medium composed of H and He in a ratio  $\text{He}/\text{H} = 0.1$  by number of atoms. This calculation was performed for an interstellar energy of 700 MeV/nuc and ionization energy losses were neglected. Table 7 also shows local abundances obtained using this procedure.

In table 8 we summarize the effects of various uncertainties on the source ratio predictions obtained by applying the secondary tracer technique to isotopes of the elements O, Ne, S, Ar, and Ca. The local abundances listed in table 7 are employed as a basis for calculating source abundances using equation 12. Since the local abundances in table 7 were calculated neglecting ionization energy loss, when equation 12 is applied using these local abundances it should only reproduce the source abundances (also shown in the table) if we again assume

Table 1

## Source and Local Abundances\*

Isotope	Source	Local	Isotope	Source	Local
Ni-64	.009	.00412	Ar-40	0	.0952
Ni-62	.03	.0142	Ar-38	.13	.661
Ni-61	.01	.00598	Ar-37	0	.257
Ni-60	.21	.101	Ar-36	.67	.798
Ni-59	0	.00507	Cl-37	.20	.300
Ni-58	.54	.261	Cl-35	.08	.467
Ni-56	0	.00136	S-36	.0004	.0506
Co-59	0	.00352	S-34	.13	.574
Co-57	0	.0208	S-33	0 (.02)	.394
Fe-58	.01	.0377	S-32	2.85	2.15
Fe-57	.48	.242	P-31	.20	.620
Fe-56	20.17	9.86	Si-30	.65	.903
Fe-55	0	.517	Si-29	.99	1.08
Fe-54	1.28	.905	Si-28	19.36	13.0
Mn-55	.10	.337	Al-27	2.30	2.89
Mn-54	0	.331	Al-26	0	.528
Mn-53	0	.521	Mg-26	2.68	2.38
Cr-54	.01	.0606	Mg-25	2.43	2.82
Cr-53	.04	.239	Mg-24	18.89	14.1
Cr-52	.33	1.04	Na-23	.90	2.71
Cr-51	0	.594	Ne-22	1.63	2.81
Cr-50	.02	.341	Ne-21	0 (.04)	1.57
V-51	0	.116	Ne-20	13.33	11.4
V-50	0	.281	F-19	0	2.15
V-49	0	.566	O-18	.23	1.98
Ti-50	.005	.0369	O-17	0 (.04)	1.89
Ti-49	.006	.109	O-16	110.7	89.01
Ti-48	.07	.714	N-15	.03	11.04
Ti-47	.007	.667	N-14	7.97	13.84
Ti-46	.008	.588	C-13	1.11	6.00
Ti-44	0	.0308	C-12	98.89	94.00
Sc-45	0	.484	B-11	0	17.6
Ca-48	.004	.00225	B-10	0	8.13
Ca-46	.00008	.00776	Be-10	0	1.69
Ca-44	.05	.416	Be-9	0	2.80
Ca-43	0 (.003)	.393	Be-7	0	5.04
Ca-42	.02	.462	Li-7	0	6.99
Ca-41	0	.109	Li-6	0	8.37
Ca-40	2.33	1.34			
K-41	.007	.240			
K-40	0	.242			
K-39	.09	.496			

\* Normalized so that carbon=100.

ORIGINAL PAGE IS  
OF POOR QUALITY.

that  $s(E)=0$ . In line 1 of table 8 we show the source abundance ratios from table 7 ( $^{18}O/^{16}O$ ,  $^{22}Ne/^{20}Ne$ ,  $^{34}S/^{32}S$ ,  $^{38}Ar/^{36}Ar$ ,  $^{42}Ca/^{40}Ca$  and  $^{44}Ca/^{40}Ca$ ) for the cases which we are examining. Line 2 shows the values of these ratios which are obtained by applying equation 12 with  $s(E)=0$  to the local abundances listed in table 7. The agreement between lines 1 and 2 is not perfect, the residual differences of  $\lesssim 2\%$  being artifacts of the two numerical calculations. These differences are small compared to the important effects which we wish to examine.

Having investigated our ability to reproduce source abundance ratios using equation 12 we now wish to include the effects of ionization energy loss, since only when we do so will we be able to investigate the effects of uncertainties in the spectral shapes of the species of interest. In line 3 we show the source ratios resulting from the re-evaluation of equation 12 with the inclusion of the correct values of  $s(E)$  (at 700 MeV/nuc,  $s(E)/E \approx .006 \text{ cm}^2/\text{g}$ ) but still using the local abundances shown in table 7. The differences in the values of the source ratios calculated with and without the effects of ionization energy loss range up to 19% in the cases examined. Clearly the approximation that  $s(E)=0$  should be avoided even at energies as large as 700 MeV/nuc. In the

Table 8

Sources of Error in Calculated Source Ratios

Description	Primary Isotopes Tracer Isotope	<sup>16</sup> O, <sup>18</sup> O	<sup>20</sup> Ne, <sup>21</sup> Ne	<sup>32</sup> S, <sup>34</sup> S	<sup>36</sup> Ar, <sup>38</sup> Ar	<sup>36</sup> Ar, <sup>39</sup> Ar	<sup>40</sup> Ca, <sup>42</sup> Ca	<sup>40</sup> Ca, <sup>44</sup> Ca
		<sup>17</sup> O	<sup>22</sup> Ne	<sup>33</sup> S	<sup>37</sup> Ar	<sup>40</sup> Ar	<sup>43</sup> Ca	<sup>43</sup> Ca
1) Cameron q <sub>i</sub> /q <sub>k</sub>		2.08 × 10 <sup>-3</sup>	1.223 × 10 <sup>-1</sup>	4.65 × 10 <sup>-2</sup>	1.940 × 10 <sup>-1</sup>	1.940 × 10 <sup>-1</sup>	8.6 × 10 <sup>-3</sup>	2.15 × 10 <sup>-2</sup>
2) equation 12 with s(E)=0		2.04 × 10 <sup>-3</sup>	1.232 × 10 <sup>-1</sup>	4.56 × 10 <sup>-2</sup>	1.934 × 10 <sup>-1</sup>	1.939 × 10 <sup>-1</sup>	8.5 × 10 <sup>-3</sup>	2.14 × 10 <sup>-2</sup>
3) equation 12 with correct s(E)		1.94 × 10 <sup>-3</sup>	1.206 × 10 <sup>-1</sup>	4.36 × 10 <sup>-2</sup>	1.829 × 10 <sup>-1</sup>	2.015 × 10 <sup>-1</sup>	1.0 × 10 <sup>-3</sup>	1.97 × 10 <sup>-2</sup>
4) parent isotopes varied		1.34 × 10 <sup>-3</sup>	1.185 × 10 <sup>-1</sup>	4.13 × 10 <sup>-2</sup>	0.332 × 10 <sup>-1</sup>	4.500 × 10 <sup>-1</sup>	7.8 × 10 <sup>-3</sup>	4.08 × 10 <sup>-2</sup>
rms deviation resulting from								
5) variation of parent isotopes		0.2 × 10 <sup>-3</sup>	0.008 × 10 <sup>-1</sup>	0.54 × 10 <sup>-2</sup>	0.80 × 10 <sup>-1</sup>	0.55 × 10 <sup>-1</sup>	9.1 × 10 <sup>-3</sup>	1.1 × 10 <sup>-2</sup>
6) variation of parent elements		0.2 × 10 <sup>-3</sup>	0.049 × 10 <sup>-1</sup>	0.51 × 10 <sup>-2</sup>	0.50 × 10 <sup>-1</sup>	0.15 × 10 <sup>-1</sup>	4.6 × 10 <sup>-3</sup>	0.82 × 10 <sup>-2</sup>
7) 20% error in fragmentation cross section normalization		0.1 × 10 <sup>-3</sup>	0.01 × 10 <sup>-1</sup>	0.05 × 10 <sup>-2</sup>	0.025 × 10 <sup>-1</sup>	0.022 × 10 <sup>-1</sup>	0.4 × 10 <sup>-3</sup>	0.04 × 10 <sup>-2</sup>
8a) 35% uncorrelated errors in fragmentation cross sections		4.0 × 10 <sup>-3</sup>	0.37 × 10 <sup>-1</sup>	4.0 × 10 <sup>-2</sup>	4.6 × 10 <sup>-1</sup>	7.8 × 10 <sup>-1</sup>	6.4 × 10 <sup>-3</sup>	6.6 × 10 <sup>-2</sup>
8b) linear approximation		3. × 10 <sup>-3</sup>	0.33 × 10 <sup>-1</sup>	4.1 × 10 <sup>-2</sup>	2.1 × 10 <sup>-1</sup>	2.3 × 10 <sup>-1</sup>	6.3 × 10 <sup>-3</sup>	6.1 × 10 <sup>-2</sup>
9) 35% errors in fragmentation cross sections--partly correlated		0.5 × 10 <sup>-3</sup>	0.10 × 10 <sup>-1</sup>	1.2 × 10 <sup>-2</sup>	1.2 × 10 <sup>-1</sup>	0.78 × 10 <sup>-1</sup>	9.3 × 10 <sup>-3</sup>	0.89 × 10 <sup>-2</sup>
10) 10% errors in total inelastic cross section normalization		0.1 × 10 <sup>-3</sup>	0.007 × 10 <sup>-1</sup>	0.04 × 10 <sup>-2</sup>	0.022 × 10 <sup>-1</sup>	0.015 × 10 <sup>-1</sup>	0.3 × 10 <sup>-3</sup>	0.03 × 10 <sup>-2</sup>
11) 10% uncorrelated errors in total inelastic cross sections		0.1 × 10 <sup>-3</sup>	0.008 × 10 <sup>-1</sup>	0.05 × 10 <sup>-2</sup>	0.027 × 10 <sup>-1</sup>	0.056 × 10 <sup>-1</sup>	0.5 × 10 <sup>-3</sup>	0.04 × 10 <sup>-2</sup>
12) errors of 0.2 in spectral indices		0.4 × 10 <sup>-3</sup>	0.055 × 10 <sup>-1</sup>	0.83 × 10 <sup>-2</sup>	0.53 × 10 <sup>-1</sup>	0.47 × 10 <sup>-1</sup>	1.3 × 10 <sup>-3</sup>	0.89 × 10 <sup>-2</sup>
13) error due to statistics in measuring p <sub>i</sub> /p <sub>k</sub> and p <sub>j</sub> /p <sub>k</sub> using 1000 events		7.1 × 10 <sup>-3</sup>	0.28 × 10 <sup>-1</sup>	3.6 × 10 <sup>-2</sup>	1.4 × 10 <sup>-1</sup>	1.9 × 10 <sup>-1</sup>	3.7 × 10 <sup>-3</sup>	3.3 × 10 <sup>-2</sup>

15b

ORIGINAL PAGE IS  
OF POOR QUALITY

analysis which follows of other sources of error in calculating the source abundance ratios we have included the effects of ionization energy loss. Therefore the resulting ratios,  $q_j/q_k$ , should be compared with the values shown in line 3 of table 8 rather than with those in lines 1 and 2.

In calculating the effects of the various sources of error we have used a Monte Carlo technique in which the parameter being investigated is varied with an appropriate distribution and the remaining parameters are held fixed at their nominal values. We generate 200 such cases and calculate the rms deviation of the values of  $q_j/q_k$  obtained from equation 12.

### 3.3.2.1 Abundances of Parent Nuclei

The secondary source term,  $\hat{S}_i$ , is of the form

$$\hat{S}_i = \sum_l \left[ \frac{\sigma_{pl_i} + (n_{He}/n_H)\sigma_{\alpha p_i}}{M_H + (n_{He}/n_H)M_{He}} \right] \phi_l$$

where the summation is over all species which can produce species  $i$  by collision with interstellar hydrogen or helium. Since it is experimentally more difficult to resolve the isotopes of elements of higher atomic number than those of lower atomic number (see, for example,

figure 31), it is important to address the question of whether detailed knowledge of the isotopic composition of parent nuclei is required in evaluating  $\hat{S}_i$ , or whether the elemental abundances which are presently available (Benegas et al., 1975; Ormes et al., 1975; Silberberg et al., 1976; Caldwell and Meyer, 1977; Garcia-Munoz et al., 1977a) are adequate. In order to answer this question we have assumed that the local abundances of the three isotopes of interest are known and have used values of these local abundances from table 7. However we also assume that only elemental abundances of the heavier (parent) species are known. In order to evaluate equation 12 we must make some assumption about the isotopic make-up of the parent elements. We have chosen to assume that there is no a priori preference for one isotope of a particular parent element over another. Using this assumption we investigate the importance of knowing the isotopic composition of the parent elements. In evaluating equation 12 we have used nominal values of cross sections, spectral indices and elemental abundances while randomly varying the isotopic composition of each parent element. The isotopes that are stable in the cosmic rays are randomly assigned fractions of the total elemental abundance with equal weights. Having assigned abundances, we calculate the  $\hat{S}_i$  and then evaluate  $q_j/q_k$ .

for the flux ratios  $\phi_j/\phi_k$  and  $\phi_i/\phi_k$  obtained from table 7. This procedure was repeated 200 times to obtain a mean value of  $q_j/q_k$  and a standard deviation due to isotopic variations in parent nuclei. The resulting means are shown in line 4 of table 8, while the standard deviations are shown in line 5.

It can be seen that the mean value of  $q_j/q_k$  (line 4 of table 8) obtained while varying the isotopic composition of the parent elements is in some cases significantly different from the value in line 3 of the table, this difference sometimes being several times larger than the rms deviation (line 5) resulting from this variation. This is due to the fact that isotopes which are dominant in the solar abundances are those having the smallest neutron excess, at least up through  $Z=22$  (Cameron, 1973) and that spallation reactions which form products which have neutron excesses close to that of the parent nucleus are more probable than reactions which significantly alter the neutron excess. The largest such error occurs in the case of the isotopes of Ar. In this case the secondary production is largely due to spallation of calcium. The ratios of cross sections for producing the isotopes  $^{36}\text{Ar}$ ,  $^{37}\text{Ar}$ ,  $^{38}\text{Ar}$  and  $^{40}\text{Ar}$  in a  $p + ^{40}\text{Ca}$  reaction are 1 : 1.4 : 1.4 : 0 while in a  $p + ^{48}\text{Ca}$  reaction they are 1 : 0.2 : 5 : 7 (Silberberg and Tsao,

[973a). Because of this wide variation a knowledge of the isotopic abundance of Ca in the cosmic rays is essential for interpreting the observed abundances of the Ar isotopes.

In most cases the dominant contributions to the secondary production of an element come from other elements with atomic numbers close to that of the element of interest. For example, the secondary O is largely produced from Ne and Mg, the secondary Ne from Mg and Si, the secondary S from Ar and Ca, the secondary Ar from Ca and Fe, and the secondary Ca from Fe. It should be possible for an instrument capable of measuring the isotopic composition of the element of interest to also obtain measurements of the isotopic composition of these dominant parents. The use of such measurements in calculating  $\hat{S}_i$  should significantly reduce the uncertainty (both the rms uncertainty and the systematic shift) in the secondary corrections required.

It should be noted that uncertainties in  $q_j/q_k$  due to uncertainty in isotopic composition of the parent elements can be significantly reduced without having to resolve individual isotopes of these elements. Mass distributions with mass resolutions as large as 1 AMU should be of considerable value, since spallation cross sections tend

to vary smoothly with particle mass. In some cases such distributions are already available (Fisher et al., 1976). In the case of Ar where the dominant parent, Ca, has many stable isotopes, it should be particularly useful to eliminate some of these isotopes as major contributors to the production of secondary Ar.

In addition to the present lack of information concerning the isotopic abundances of the heavier elements ( $Z \gtrsim 10$ ), there are uncertainties in the elemental abundances which will produce uncertainties in the  $\hat{S}_i$  and hence in  $q_j/q_k$ . We have used the tabulation by Silberberg et al. (1976) of local elemental abundances and their uncertainties, based on the measurements of a number of investigators at rigidities  $\gtrsim 4$  GV (energies  $\gtrsim 1275$  MeV/nuc). Local abundances of the various elements were allowed to vary independently with Gaussian distributions with standard deviations equal to the uncertainties given by Silberberg et al. (1976). These uncertainties range between 2% for the most abundant elements (such as oxygen) to 50% for elements with small abundances (such as scandium). The isotopic compositions of all elements were simultaneously varied in the manner described above. Since the isotopic and elemental compositions were varied independently, we obtained the uncertainty in  $q_j/q_k$  due to elemental composition,

uncertainties alone by quadratic subtraction of the uncertainty from varying only the isotopic composition from that obtained while varying both elemental and isotopic compositions. In all the cases considered it was possible to obtain a statistically significant result by using 200 events. The uncertainty obtained in this manner is shown in line b of table 8.

In comparing lines 5 and b of table 8 it can be seen that the uncertainty in estimating  $q_j/q_k$  due to present uncertainties in elemental abundances is comparable to the uncertainty due to our total lack of information concerning the isotopic make-up of the various parent elements. Thus a detailed knowledge of the isotopic composition of these parents will not in most cases significantly improve the accuracy of calculations of source abundances until the elemental composition can be measured with increased precision. However, presently operating particle spectrometers have sufficient elemental resolution so that increased exposure above the earth's atmosphere would make it possible to reduce the elemental composition uncertainties to a point where some knowledge of the isotopic composition of parent species will be useful.

ORIGINAL PAGE IS  
OF POOR QUALITY

### 3.3.2.2 Fragmentation Cross Sections

In order to investigate the effects of uncertainties in the fragmentation cross sections,  $\sigma_{pL}$  and  $\sigma_{\alpha L}$ , on the calculated source abundances we have varied these cross sections in several ways. First, we have assumed that the uncertainties in these cross sections are entirely systematic, and in particular that there are no uncertainties in the ratios of the cross sections to one another but that there is simply an overall normalization error. One can obtain estimates of the magnitude of possible normalization errors by examining ratios of values obtained for the same cross sections from different experiments or calculations. Lindstrom et al. (1975a) found an average ratio of 1.22 between their measurements of cross sections for the production of lighter isotopes by the spallation of  $^{12}\text{C}$  and  $^{16}\text{O}$  and the value obtained from the semi-empirical formulas of Silberberg and Tsao (1973a). In line 7 of table 8 we show the uncertainty in  $q_j/q_k$  obtained due to a 20% uncertainty in the absolute normalization of the fragmentation cross sections. Even for a normalization uncertainty of this size, the uncertainty produced in  $q_j/q_k$  is comparable to uncertainties due to various other effects and at present is not a limitation on our ability to obtain cosmic ray source abundances.

Second, we have assumed that the uncertainties in the various spallation cross sections are entirely uncorrelated. We independently make a random selection of each of these cross sections from a Gaussian distribution with mean equal to the cross section calculated using the formulas of Silberberg and Tsao and a selected fractional standard deviation. Lindstrom et al. (1975a) obtain a standard deviation of 37% in the distribution of the ratios of their carbon and oxygen spallation cross sections to those calculated using the formulas of Silberberg and Tsao. Also, comparisons by Silberberg and Tsao (1973a) of their values to the measurements on which the semi-empirical formulas are based indicate uncertainties of ~30-40%. The resulting uncertainties in the calculated values of  $q_j/q_k$  are shown in line 8a of table 8 for 35% standard deviations in the fragmentation cross sections.

In most of the cases being considered the uncertainties in  $q_j/q_k$  due to uncorrelated cross section errors is at least as large as the value of  $q_j/q_k$  itself. In section 3.3.4 we will examine the extent to which these errors must be reduced in order to derive meaningful parameters characterizing the cosmic ray sources. In that calculation we will assume that the source ratio errors scale in proportion to the uncertainty in the

fragmentation cross sections. In order to establish the validity of such scaling of the errors in  $q_j/q_k$  in proportion to the fractional uncorrelated uncertainties in the fragmentation cross sections, we have recalculated the values in line 8a of table 8 by assuming cross section errors of 3.5% and then multiplying the resulting error in  $q_j/q_k$  by a factor of 10. These errors obtained from this "linear approximation" are shown in line 8b of table 8. A comparison of lines 8a and 8b shows that linear scaling of the errors in  $q_j/q_k$  for cross section errors less than 35% is reasonable except in the case of argon. The failure of this scaling in the case of argon is due to the fact that even the most abundant isotope,  $^{36}\text{Ar}$ , has a large secondary component, so that the denominator in equation 12 is relatively small. The variation of our estimate of the secondary correction due to large ( $\sim 35\%$ ) Gaussian errors in the fragmentation cross sections results in a non-Gaussian distribution of  $q_j/q_k$  values. The long tail on this distribution grossly affects the calculation of the rms spread of the distribution.

Third, we have assumed that ratios of cross sections for producing different isotopes from a single parent species can be precisely determined but that the absolute magnitude of these cross sections is uncertain by 35%. Such a situation should result when fragmentation cross

sections for producing various isotopes are measured in a single experiment such as those performed by Heckman and collaborators (Lindstrom et al., 1975a). In such experiments details of the experimental set-up such as target thickness and beam flux will affect the absolute cross sections obtained but should only weakly affect cross section ratios. In line 9 of table 8 we show the uncertainty in  $q_j/q_k$  produced by a 35% error of this type. We have also calculated these uncertainties using a linear extrapolation from those obtained assuming a 3.5% cross section error. Good agreement between these two calculations is obtained in each of the cases being considered.

A comparison of values in line 9 with those in line 8 shows that an improvement by a factor of between 3 and 10 in the effect of fragmentation cross section errors on the uncertainty in calculating source abundance ratios will result if the cross sections from a single parent can be obtained with high relative precision.

In evaluating the effect of cross section uncertainties on source ratio calculations we have used cross section errors based on comparisons between the semi-empirical cross sections of Silberberg and Tsao and various measured cross sections. These errors are

appropriate for the present calculation since the lack of measurements of most of the required cross sections forces us to utilize the semi-empirical results. However, it should be noted that frequently the uncertainties in measured fragmentation cross sections are somewhat less than the 35% assumed here (Silberberg and Tsao, 1973b; Lindstrom et al., 1975a; Perron, 1976). Thus measurement of cross sections for those reactions which dominate the secondary production of species which we are considering should significantly improve the accuracy of the calculations. Note also that the secondary production of many cosmic ray species may be dominated by contributions from a few nearby parents. In this case substantial reduction of the uncertainty in  $q_j/q_k$  may be achieved by improved measurements of a few key cross sections. In the present study we have not attempted to identify these key cross sections.

### 3.3.2.3 Total Inelastic Cross Sections

We have evaluated the contributions to the uncertainty in  $q_j/q_k$  which result from uncertainties in the total inelastic cross sections,  $\sigma_{pi}$  and  $\sigma_{\alpha i}$ . As was done in the case of fragmentation cross sections, we have examined two extreme cases--cross sections subject to a

normalization error but no relative error and cross sections subject to uncorrelated errors. Comparisons of total inelastic cross sections measured by fragmenting beams of C, O and Ar on a variety of targets (Cheshire et al., 1974; Lindstrom et al., 1975b) with simple geometrical models shows that such models yield cross sections accurate to  $\sim 10\%$ . We have used 10% as an estimate of both the normalization error and the uncorrelated errors in the total inelastic cross sections. The uncertainties in  $q_j/q_k$  resulting from these errors are shown in lines 10 and 11, respectively, of table 8. It can be seen that these errors make relatively small contributions to the overall uncertainty in  $q_j/q_k$ .

#### 3.3.2.4 Spectral Indices

Uncertainties in the spectral indices of the observed fluxes of isotopes of the elements of interest contribute to the uncertainty in the derived source ratio since ionization energy loss continually reduces the energy of individual cosmic ray particles resulting in an effective sink (or source) of particles at any particular energy. The magnitude of this effect depends on the slope of the equilibrium spectra. We have assumed that at the energies of interest the local interstellar spectra of the

species which we are considering are proportional to the proton and alpha particle spectra obtained by Garrard (1973) from near-earth measurements and calculations of the effects of solar modulation. Garrard found a spectrum of the form

$$j\left(\frac{E}{M}\right) \propto \left(\frac{E}{M} + (1-\mu)m\right)^{-2.65},$$

with  $m=931$  MeV/nuc. He obtains  $\mu=0.25 \pm 0.2$ . From this spectral shape we obtain the spectral index at 700 MeV/nuc as

$$\gamma = 1.33 \pm 0.18.$$

It should be recognized that this value and its uncertainty can only be treated as an indication of those which should be obtainable from near-earth spectra of the species of interest if these spectra can be measured with greater statistical accuracy than they have been measured at this time. In order to reduce the uncertainties in the spectral indices it will be necessary to refine our understanding of the solar modulation process or to make abundance measurements outside of the solar cavity.

In line 12 of table 8 we show the uncertainty in  $q_j/q_k$  which results from independent uncertainties of 0.2 in the spectral indices of both of the primary isotopes

and of the secondary tracer isotope. For the cases which we are considering this source of uncertainty will become important when the uncertainty due to uncorrelated fragmentation cross section errors can be significantly reduced. It should be noted that since the spectral indices appear in equation 12 multiplied by  $s(E)/E$ , the effects of uncertainties in these indices will decrease with increasing energy.

### 3.3.2.5 Isotopic Abundances

Finally, we show in line 13 of table 8 the uncertainty in  $q_j/q_k$  due to uncertainties in measuring the isotopic ratios  $\phi_i/\phi_k$  and  $\phi_j/\phi_k$ . We assume in this and in all subsequent sections that the uncertainties in these ratios are entirely statistical (i.e., that measurements can be made with good mass resolution). We have calculated the uncertainties in  $q_j/q_k$  for the case of 1000 events observed among the three species (i, j, and k). It can be seen from table 4 that for the elements considered here the HEIST instrument will accumulate between 100 and 5000 events per day over its entire energy range. The uncertainties shown in table 8 due to uncertainties in the measured isotopic ratios are proportional to  $1/\sqrt{N}$ , where N is the number of events observed, so this uncertainty can

easily be scaled to the number of events actually observed in an experiment.

The uncertainties in measuring isotopic abundance ratios are generally the most significant contributions to the uncertainty in the calculated source ratio along with the uncertainty due to uncorrelated errors in fragmentation cross sections (assuming 1000 events are observed). In order to reduce this uncertainty it will be necessary to obtain increased exposure factors (geometrical factor times duration of exposure) and to obtain sufficient mass resolution so that systematic errors in the measurement will not limit one's ability to reduce the uncertainty in the measured ratios to the statistical limits.

### 3.3.2.b Summary of Uncertainties

At present, the precision attainable in deriving isotopic source ratios is limited primarily by uncertainties in fragmentation cross sections and by the limited counting statistics obtained by typical cosmic ray experiments. The first of these uncertainties can be improved by identifying those cross sections which dominate the production of the element of interest and then making high precision measurements of the ratios of

these cross sections. In fact, significant progress has been made both at Berkeley (Lindstrom et al., 1975a) and at Orsay (Perron, 1976; Raisbeck and Yiou, 1977a; Raisbeck et al., 1977b) in the past few years and it should soon be possible to utilize measured cross sections rather than those obtained from the semi-empirical formulas in many cases. The uncertainty due to limited counting statistics will be reduced when it becomes possible to fly experiments with large geometrical factors ( $\approx 100$  cm sr) for extended periods on spacecraft outside of the earth's atmosphere.

The systematic uncertainty which is present in some cases due to uncertainty in the isotopic make-up of parent elements can be reduced, as mentioned above, by using low resolution mass spectra to establish limits on the distribution of parent isotopes. Clearly, even greater improvement will result if isotopes of the important parent species can be individually resolved.

ORIGINAL PAGE IS  
OF POOR QUALITY

### 3.3.3 Curves for Interpreting Local Abundances

We now wish to extend the treatment of source ratio uncertainties in section 3.3.2 to a range of local isotopic abundances other than those which would be obtained from a solar-like source. By so doing it will be possible to characterize the dependence of source abundance uncertainties on the magnitudes of the abundance ratios observed in local interstellar space. These results used in conjunction with models which predict the dependence of the source abundances on various astrophysical parameters make it possible to evaluate the significance of conclusions concerning these parameters which are derived from cosmic ray observations. Conversely, these results can be utilized for the purpose of designing experiments capable of distinguishing between alternative astrophysical models at a predetermined significance level.

We separately consider the following triplets of isotopes:  $^{16}\text{O}$ ,  $^{18}\text{O}$ ,  $^{17}\text{O}$ ;  $^{20}\text{Ne}$ ,  $^{22}\text{Ne}$ ,  $^{21}\text{Ne}$ ;  $^{32}\text{S}$ ,  $^{34}\text{S}$ ,  $^{33}\text{S}$ ;  $^{40}\text{Ca}$ ,  $^{42}\text{Ca}$ ,  $^{43}\text{Ca}$ ; and  $^{40}\text{Ca}$ ,  $^{44}\text{Ca}$ ,  $^{43}\text{Ca}$ . In each case the last isotope listed is assumed to be absent at the cosmic ray source. The isotopic abundances of these species can yield information concerning both the nucleosynthesis processes responsible for the production

of the cosmic rays and the state of evolution of the material from which the cosmic rays are derived. In section 3.3.4 we will discuss how local abundances are affected by one of the important source parameters.

For each case we have obtained three families of curves. First, we use equation 12 to obtain the dependence of  $q_j/q_k$  on the local abundance ratios  $\phi_j/\phi_k$  and  $\phi_j/\phi_k$ . In so doing we have assumed an energy of 700 MeV/nuc, have included the effects of ionization energy loss and have used nominal values of cross sections, spectral indices and elemental abundances of parent species. However, we have individually randomized the local isotopic composition of each parent element in order to avoid biasing the results toward a solar-like abundance distribution. As shown in section 3.3.2.1 systematic shifts of the calculated source abundances can be produced by varying one's assumption concerning the local isotopic composition of the parent elements. For this reason we note that if observational information concerning the isotopic make-up of the dominant parent elements is available it may be inappropriate to use the curves which we will present when attempting to derive source ratios from cosmic ray abundance measurements. Instead, these curves should be recalculated incorporating as many data as are available regarding the isotopic

composition of the parents. However, the curves which we present are useful for investigating the dependence of the various uncertainties discussed in section 3.3.2 on the source and local ratios.

The other two families of curves which we present show the dependence on the local abundance ratios of the dominant uncertainties in the derived source ratios. These uncertainties are due to statistical errors in the measurement of the local abundances and to uncertainties in the parameters in equation 12. The calculation of the statistical uncertainties extends the results presented in section 3.3.2.5 for the case of a solar-like cosmic ray source. In evaluating the calculation uncertainties we restrict our attention to the effects of uncorrelated errors in the fragmentation cross sections. At the present level of uncertainties the effect of these errors significantly exceeds the combined effects of the other errors discussed above. However these other errors set a lower limit on the level to which the uncorrelated cross section errors can be reduced before the curves which we present can no longer be interpreted as representing the overall calculational uncertainty in obtaining  $q_j/q_k$ .

### 3.3.3.1 Source Ratio Curves

The curves relating the source ratio  $q_j/q_k$  to the local abundance ratios  $\phi_i/\phi_k$  and  $\phi_j/\phi_k$  are obtained in the following manner. Using nominal values of cross sections, spectral indices and elemental abundances of parent species, but randomly varying the isotopic composition of each parent element, we have evaluated equation 12 a number of times for each of a large number of combinations of the observed ratios,  $\phi_i/\phi_k$  and  $\phi_j/\phi_k$ . For each such pair of local isotope ratios, the resulting values of the source ratio,  $q_j/q_k$ , were averaged to obtain an unweighted mean of those source ratios which are consistent with the observed elemental abundances of heavier species. For selected values of the source ratio,  $q_j/q_k$ , interpolation has been performed to obtain the locus of points in the  $\phi_i/\phi_k$  vs.  $q_j/q_k$  plane which can be obtained from a cosmic ray source in which the species  $i$  is absent and which yields the desired local ratio,  $\phi_i/\phi_k$ , after propagation. In addition, these combinations of source and local abundance ratios are consistent with a leaky box propagation model and with observed values of local spectra and elemental abundances of parent nuclei. These curves are plotted as solid lines in figure 32a through e.

FIGURE 32

Families of curves showing the relationship between cosmic ray abundance ratios in local interstellar space and abundance ratios at the sources (solid curves). Also shown are the uncertainties which result when source ratios are calculated from observed abundances due to 1) statistical errors in the measured local abundances (dotted curves) and 2) errors in calculating the secondary corrections to the observed fluxes due to uncertainties in the nuclear fragmentation cross sections (dashed curves). Calculations are based on the secondary tracer technique (see text) as applied to triplets of isotopes (k, j, i) of a single element. Species i is assumed to be absent at the cosmic ray sources. The ordinate is the source abundance ratio,  $q_j/q_k$ , while the abscissa is the corresponding local ratio,  $\phi_j/\phi_k$ . The solid curves are parameterized by the local ratio  $\phi_i/\phi_k$ , which characterizes the

amount of secondary production during propagation. The dotted curves, showing the source ratio uncertainties due to statistical errors in the flux measurements are based on the observation of 1000 events distributed among the three isotopes of interest. The indicated fractional uncertainties can be scaled in proportion to  $\sqrt{1000/N}$  for observations of N events. The dashed curves, showing uncertainties due to uncorrelated fragmentation cross section errors, are based on cross section errors of 35%. The indicated fractional uncertainties can be scaled in proportion to  $f/0.35$  for relative cross section errors of  $(100 \times f)\%$ .

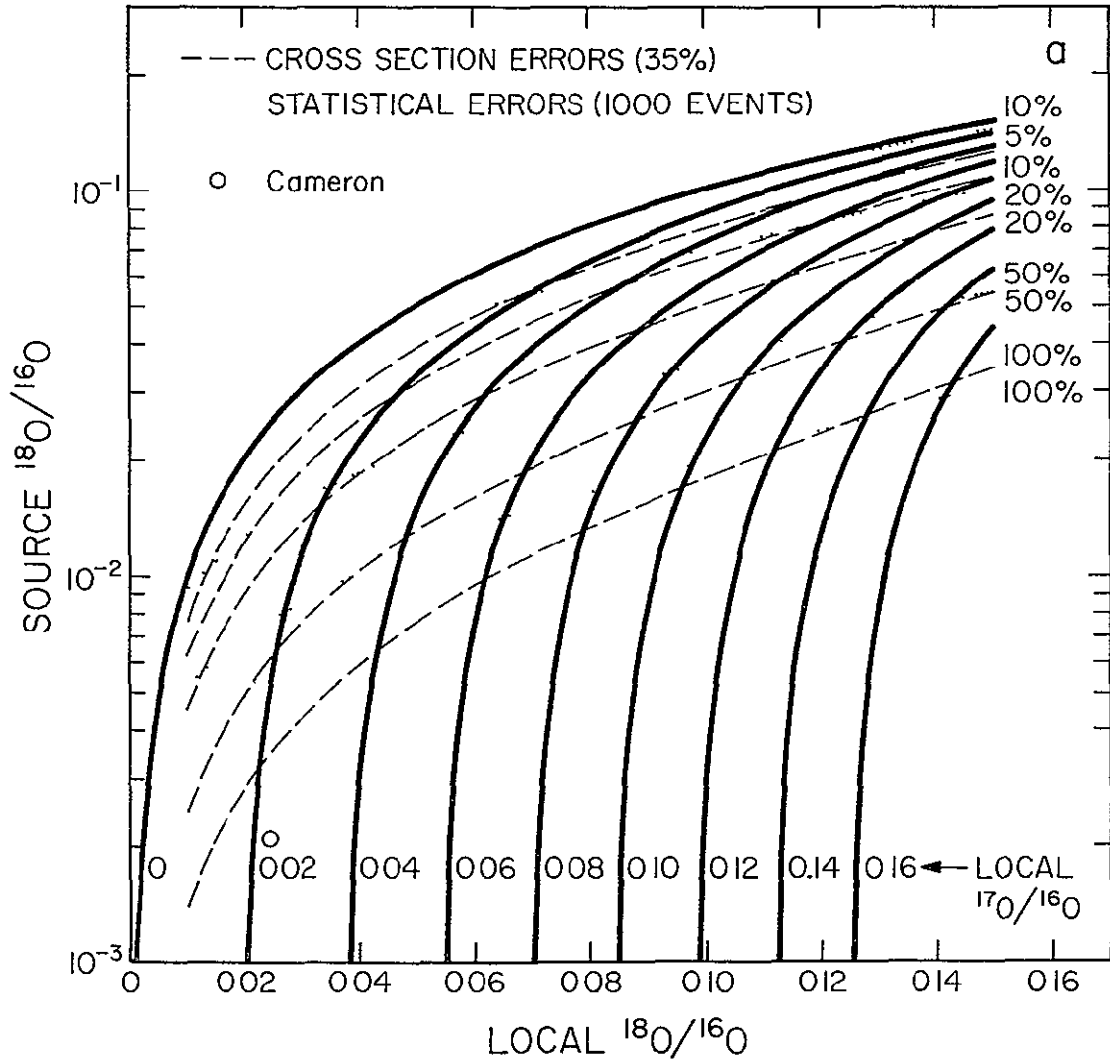
In each case we indicate the point corresponding to cosmic rays obtained from a source having a solar-like isotopic composition, as given by Cameron (1973). See table 7. In cases (c) and (d) we show the abundances which would result from production of the elements S and Ca, respectively, by explosive oxygen burning in environments having various degrees of neutron enrichment,  $\eta$ , as presented by Woosley et al. (1973). See section 3.3.4 of

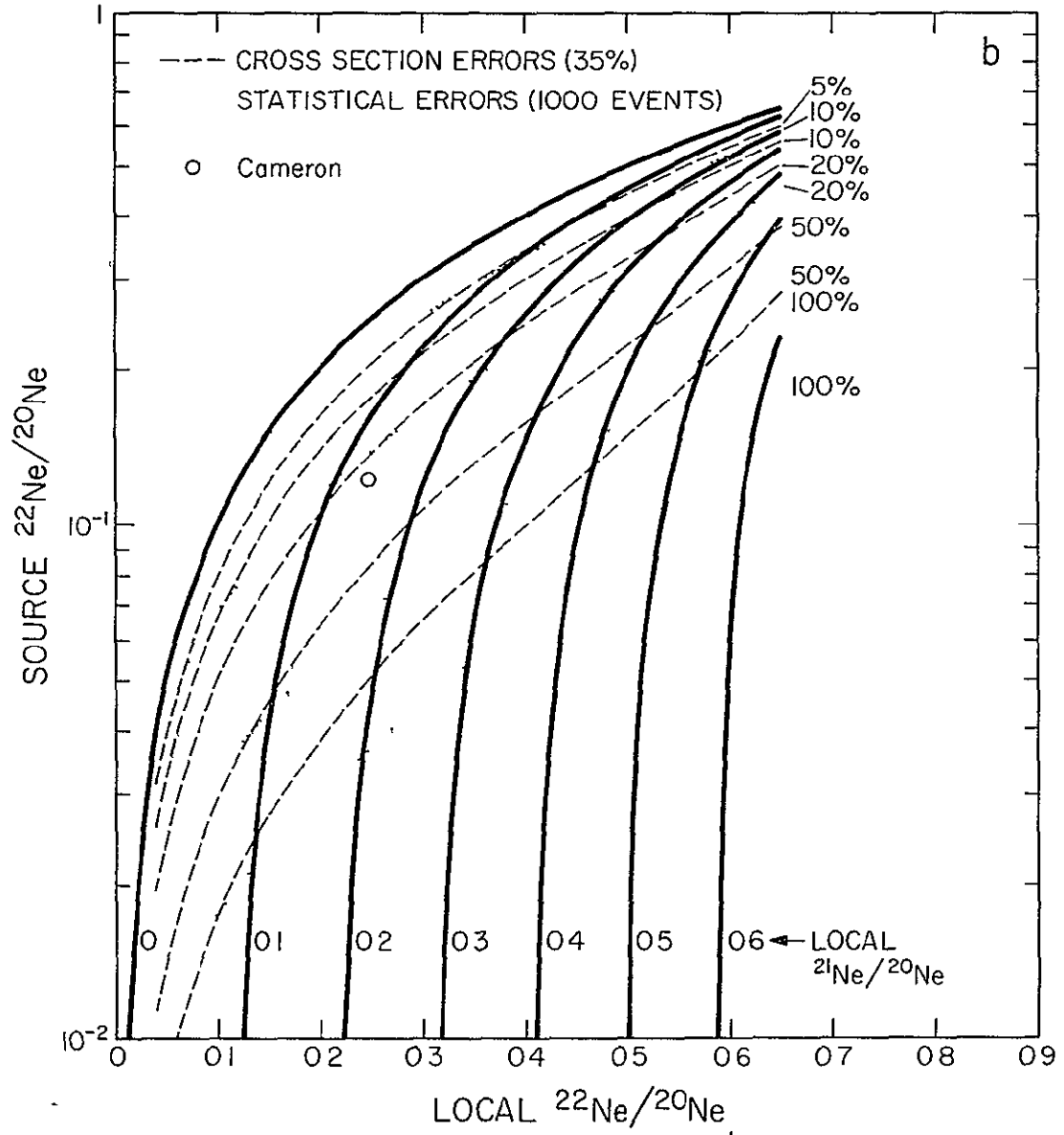
the text.

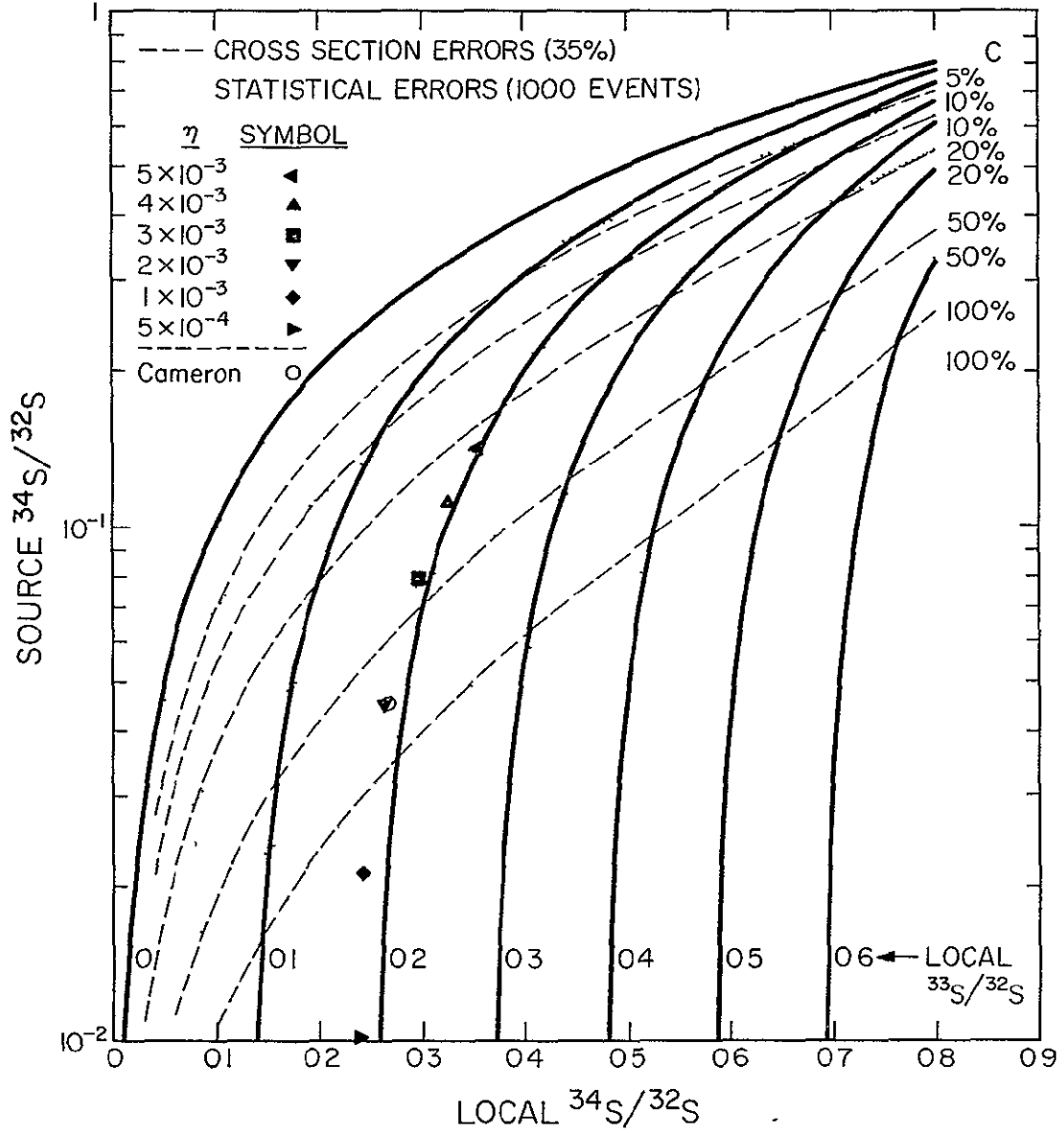
The isotopes (k, j, i) treated in the various plots are as follows:

- a)  $^{16}\text{O}$ ,  $^{18}\text{O}$ ,  $^{17}\text{O}$
- b)  $^{20}\text{Ne}$ ,  $^{22}\text{Ne}$ ,  $^{21}\text{Ne}$
- c)  $^{32}\text{S}$ ,  $^{34}\text{S}$ ,  $^{33}\text{S}$
- d)  $^{40}\text{Ca}$ ,  $^{42}\text{Ca}$ ,  $^{43}\text{Ca}$
- e)  $^{40}\text{Ca}$ ,  $^{44}\text{Ca}$ ,  $^{43}\text{Ca}$ .

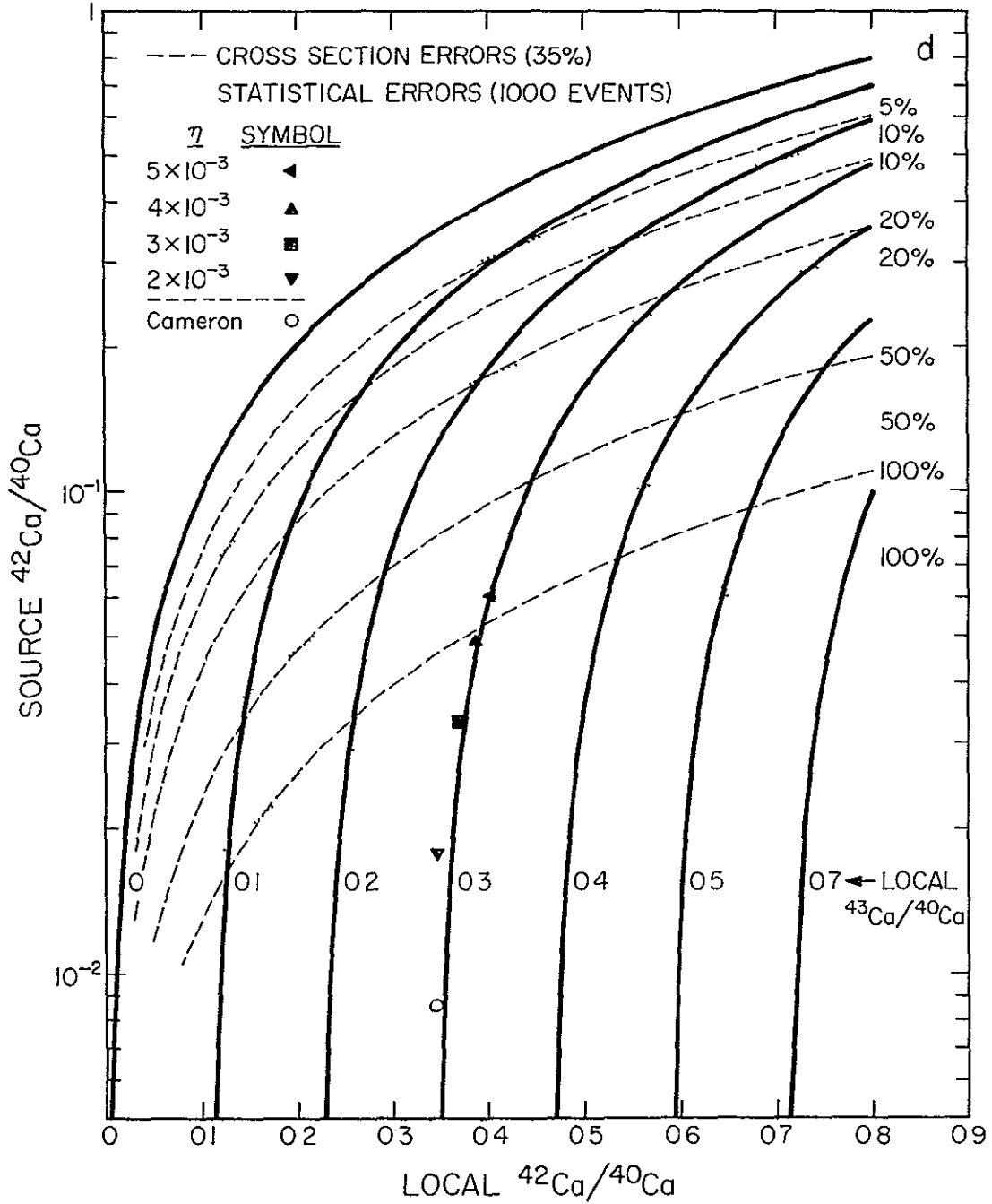
ORIGINAL PAGE IS  
OF POOR QUALITY



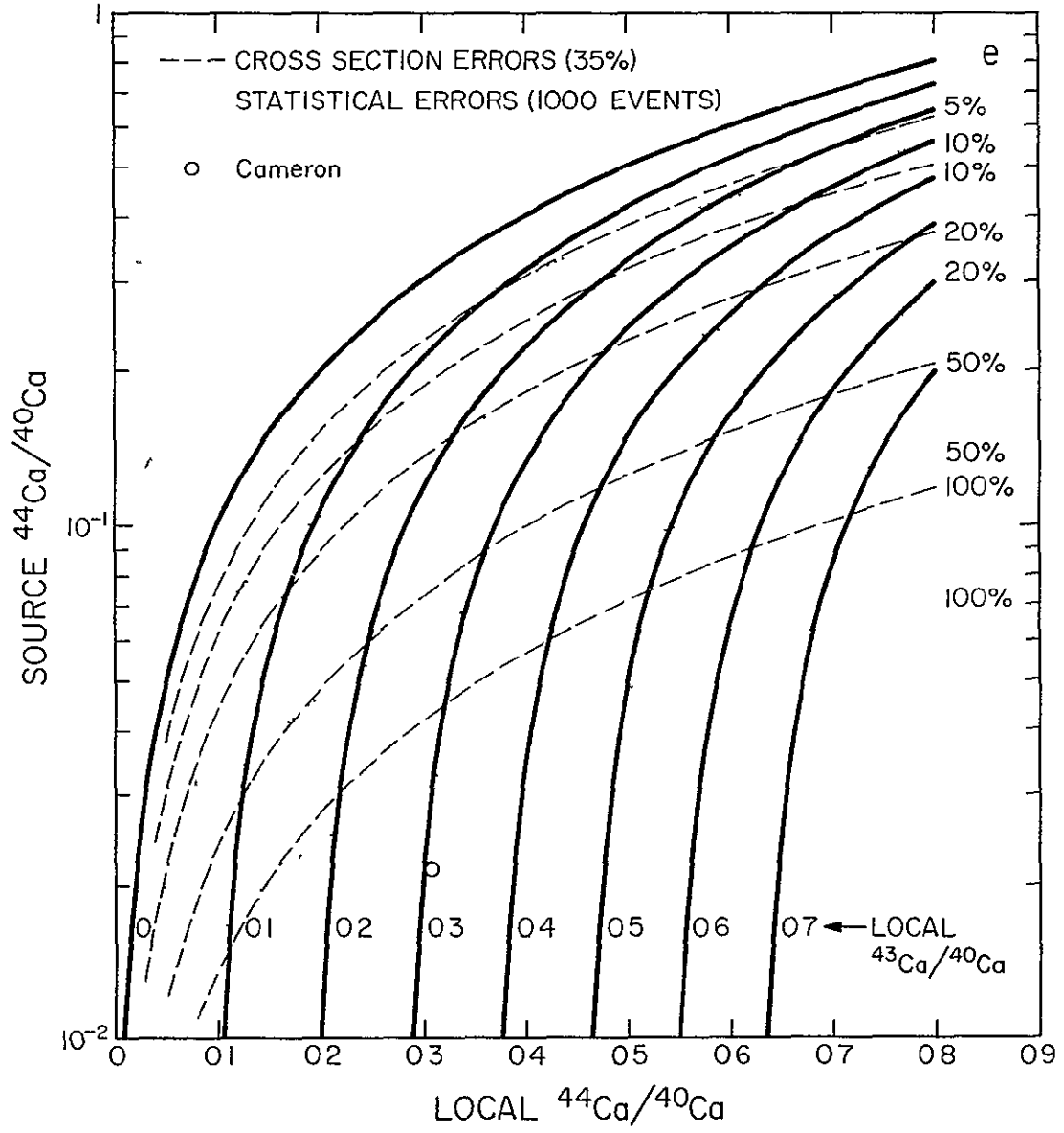




ORIGINAL PAGE IS  
 OF POOR QUALITY



C-3



A number of features are common to all of these figures. First, notice that along the line  $\phi_i/\phi_k=0$  we have  $\phi_j/\phi_k = q_j/q_k$ . This is because of our assumption that species  $i$  is absent at the cosmic ray sources. If species  $i$  is also absent in the local cosmic rays, then the amount of interstellar material traversed during propagation must be negligible and the source abundances will be the same as the observed abundances.

Second, at a fixed value of the source ratio,  $q_j/q_k$ , the slopes of the various curves of constant  $\phi_i/\phi_k$  increases as one goes to larger values of  $\phi_i/\phi_k$ . This increasing sensitivity of  $q_j/q_k$  to the local ratio  $\phi_j/\phi_k$  results from the fact that as  $\phi_i$  increases relative to  $\phi_k$ , the fraction of the flux  $\phi_j$  which is of secondary origin also increases. Therefore a given absolute change in  $\phi_j$  will correspond to an increasingly large relative change in  $q_j$  as one increases  $\phi_i/\phi_k$ .

Third, for each value of  $\phi_i/\phi_k$  there is a minimum value of  $\phi_j/\phi_k$  which can be attained (corresponding to  $q_j/q_k=0$ ). If the measured ratio  $\phi_j/\phi_k$  falls far enough below this limiting value of the curve corresponding to the measured ratio  $\phi_i/\phi_k$  to be inconsistent with errors in measuring these ratios and in calculating the location of the curves, we would conclude that species  $i$  is unsuitable

for use as a tracer of secondary production and probably has a non-negligible source abundance. Note, however, that it is possible for a point to fall above the limiting value of  $\phi_j/\phi_k$  even if  $q_i > 0$ . In some cases, for example the isotopes of Ar, it should be possible to use consistency checks between source abundances obtained using more than one possible tracer to eliminate this possibility.

### 3.3.3.2 Statistical Error Curves

In calculating statistical uncertainties we have assumed that we have 1000 events distributed among the three isotopes of interest. The numbers of events of each of these isotopes are assumed to be statistically independent. The uncertainty in the deduced ratio can be expressed as

$$\begin{aligned} \sigma_{q_j/q_k}^2 &= \left( \frac{\partial(q_j/q_k)}{\partial(\phi_j/\phi_k)} \right)^2 \left( \frac{\partial(\phi_j/\phi_k)}{\partial\phi_j} \right)^2 \sigma_{\phi_j}^2 + \left( \frac{\partial(q_j/q_k)}{\partial(\phi_i/\phi_k)} \right)^2 \left( \frac{\partial(\phi_i/\phi_k)}{\partial\phi_i} \right)^2 \sigma_{\phi_i}^2 \\ &+ \left[ \left( \frac{\partial(q_j/q_k)}{\partial(\phi_j/\phi_k)} \right) \left( \frac{\partial(\phi_j/\phi_k)}{\partial\phi_k} \right) + \left( \frac{\partial(q_j/q_k)}{\partial(\phi_i/\phi_k)} \right) \left( \frac{\partial(\phi_i/\phi_k)}{\partial\phi_k} \right) \right]^2 \sigma_{\phi_k}^2 \\ \sigma_{q_j/q_k} &= \left\{ \left( \frac{\partial(q_j/q_k)}{\partial(\phi_j/\phi_k)} \right)^2 \left( \frac{\phi_j}{\phi_k} \right) + \left( \frac{\partial(q_j/q_k)}{\partial(\phi_i/\phi_k)} \right)^2 \left( \frac{\phi_i}{\phi_k} \right) \right. \\ &\left. + \left[ \left( \frac{\partial(q_j/q_k)}{\partial(\phi_j/\phi_k)} \right) \left( \frac{\phi_j}{\phi_k} \right) + \left( \frac{\partial(q_j/q_k)}{\partial(\phi_i/\phi_k)} \right) \left( \frac{\phi_i}{\phi_k} \right) \right]^2 \right\}^{1/2} \sqrt{\frac{1 + (\phi_j/\phi_k) + (\phi_i/\phi_k)}{N}} \end{aligned}$$

The partial derivatives of  $q_j/q_k$  with respect to the measured ratios  $\phi_j/\phi_k$  and  $\phi_i/\phi_k$  are approximated by finite differences obtained from the curves in figure 32.

The dotted lines in figures 32a through 32e are lines of constant fractional uncertainty in the calculated values of  $q_j/q_k$  due to statistical errors in the measurement of local abundances. These curves are labeled with the fractional error obtained when a total of 1000 events are accumulated. The uncertainties can be scaled by a factor of  $\sqrt{1000/N}$  if the total number of events is N.

### 3.3.3.3 Computational Error Curves

In order to evaluate the uncertainty in source ratios caused by the uncertainty in the location of the various curves of constant  $q_j/q_k$  in figures 32a through 32e we have repeated the procedure used to obtain these curves while randomly varying the fragmentation cross sections and the isotopic abundances of the parent nuclei. As shown in section 3.3.2 the uncertainty in the calculated source abundances is due almost entirely to uncorrelated errors in the fragmentation cross sections, if the local abundances are precisely known. Therefore, this calculation of the uncertainties should closely

approximate the overall uncertainties which would be obtained due to the combined effect of the errors in all the parameters discussed in section 3.3.2, other than the flux ratios  $\phi_i/\phi_k$  and  $\phi_j/\phi_k$ . By calculating the rms deviation of a number of values of  $q_j/q_k$  generated at constant  $\phi_i/\phi_k$  and  $\phi_j/\phi_k$  we obtain the required uncertainties. In figure 32 we indicate by dashed lines the curves along which various fractional uncertainties in  $q_j/q_k$  result due to the uncertainties in calculating the locations of the lines of constant  $q_j/q_k$ . The qualitative characteristics of these uncertainty lines are easily understood. The uncertainty in  $q_j/q_k$  becomes large at large values of  $\phi_i/\phi_k$  independent of the value of  $\phi_j/\phi_k$  since when  $\phi_i$  becomes comparable to  $\phi_k$  the flux  $\phi_k$  must be largely of secondary origin and hence, the rather large uncertainties in secondary production will be directly reflected in the deduced source ratio. When  $\phi_i$  is small compared to  $\phi_k$  we only get a large uncertainty in  $q_j/q_k$  when  $\phi_j$  is also small. Again this simply means that  $\phi_j$  has a large secondary component (although  $\phi_k$  does not) and the uncertainty in this component will be reflected in the uncertainty in the deduced source abundance.

The lines of constant percentage error due to uncorrelated uncertainties in the fragmentation cross sections are based on an rms uncertainty of 35% in these

cross sections. The calculation uncertainties indicated in figure 32 can be scaled in proportion to this percentage uncertainty.

In the case of Ne (figure 32b) for local  $^{21}\text{Ne}/^{20}\text{Ne}$  ratios in excess of  $\sim 0.35$ , the rms spread (due to 35% cross section uncertainties) in the source value of  $^{22}\text{Ne}/^{20}\text{Ne}$  becomes larger than would be obtained by scaling from the case of cross section uncertainties smaller than 35%. This is because in this region the secondary component of the local flux of  $^{20}\text{Ne}$  is becoming a significant part of the total flux, so the denominator in equation 12 is relatively small. The 35% variation of the fragmentation cross sections produces a distribution of source  $^{22}\text{Ne}/^{20}\text{Ne}$  values having a long tail. This tail causes an unusually large value of the rms spread of these source ratios. Since we are attempting to produce a family of curves which can be scaled to yield source ratio uncertainties due to cross section errors  $\leq 35\%$ , we have recalculated the curves in the region where the local value of  $^{21}\text{Ne}/^{20}\text{Ne}$  is greater than 0.35 using cross section errors of 17.5%. These results (after being scaled up by a factor of 2) are plotted in figure 32b rather than the corresponding results obtained for cross section errors of 35%. In this way we obtain a family of curves which can be scaled to smaller cross section errors

over the entire range of local abundances plotted in the figure.

A similar situation occurs in the case of S (figure 32c) for local  $^{33}\text{S}/^{32}\text{S}$  ratios exceeding  $\sim 0.45$ . The curves have been modified in this region in the same way as described above for the case of Ne. None of the other three cases considered required such a correction over the range of parameters being considered.

Note, however, that when uncorrelated cross section errors are reduced to  $\lesssim 10\%$  the other contributions to the uncertainty in calculating the location of these curves become significant and these curves can no longer be used to obtain the overall uncertainty in the calculation of source abundance ratios.

### 3.3.4 Range of Source Abundances

In the preceding sections we have shown that over a sizeable range of local abundances of the isotopes of O, Ne, S and Ca large uncertainties will result when source abundance ratios of these isotopes are calculated both due to the poor statistical accuracy of the measurements which are presently possible and to the large uncertainties in cross sections required for estimating the secondary

ORIGINAL PAGE IS  
OF POOR QUALITY

component in the observed fluxes. It has also been shown (see table 8) that for solar-like source abundance distributions of the isotopes of these elements such large uncertainties will be obtained in most of the cases considered here. We now wish to examine the question of whether the errors expected if the cosmic ray source composition is of some reasonable, non-solar form may be less significant. Such an examination will allow us to determine the levels to which the errors considered in section 3.3.3 must be reduced in order to yield significant results.

We have considered the range of abundances obtainable in the charge range  $16 \leq Z \leq 20$  if the cosmic rays in this charge interval are produced by explosive oxygen burning (Woosley et al., 1973). These authors show that for appropriate choices of the temperature, density and neutron excess in the explosion it is possible to accurately reproduce the observed solar system abundances in this charge range. They also examine the effect of varying the neutron excess on the resulting abundances. The neutron excess is defined as

$$\eta \equiv \frac{n_n - n_p}{n_n + n_p}$$

where  $n_n$  and  $n_p$  are respectively the number densities of

neutrons and protons (both free and bound in nuclei) in the region of the explosion. Solar-like abundances are produced for  $\eta \sim 1-2 \times 10^{-3}$ . For selected values of  $\eta$ , by using the calculated source ratios  $^{42}\text{Ca}/^{40}\text{Ca}$ ,  $^{38}\text{Ar}/^{36}\text{Ar}$ ,  $^{37}\text{Cl}/^{36}\text{Cl}$  and  $^{34}\text{S}/^{32}\text{S}$  given by Woosley et al. (1973) and assuming that the other isotopes of these elements are absent at the cosmic ray sources we have calculated the expected local abundances resulting from propagation with an exponential distribution of path-lengths with a mean of  $5.5 \text{ g/cm}^2$ . We have performed the calculations at  $700 \text{ MeV/nuc}$  and have neglected ionization energy loss. The source abundances used for isotopes of the elements other than Ca, Ar, Cl and S were those of Cameron (1973) as described in section 3.3.2.

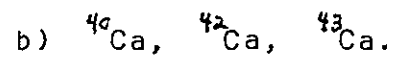
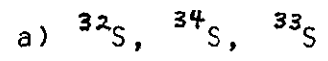
In varying the neutron excess from  $10^{-2}$  to  $10^{-4}$  a hundred fold increase in the source ratios  $^{34}\text{S}/^{32}\text{S}$ ,  $^{38}\text{Ar}/^{36}\text{Ar}$  and  $^{42}\text{Ca}/^{40}\text{Ca}$  is produced. In figures 32c and d we show the points at which the local abundances resulting from this calculation fall for selected values of  $\eta$ . The results for the Ar isotopes are not shown due to difficulties in interpreting Ar abundances without information on Ca abundances, as discussed above. It can be seen in these figures that an increase of  $\eta$  by a factor  $\sim 3$  over the value which produces solar abundances would yield source abundances which should be marginally

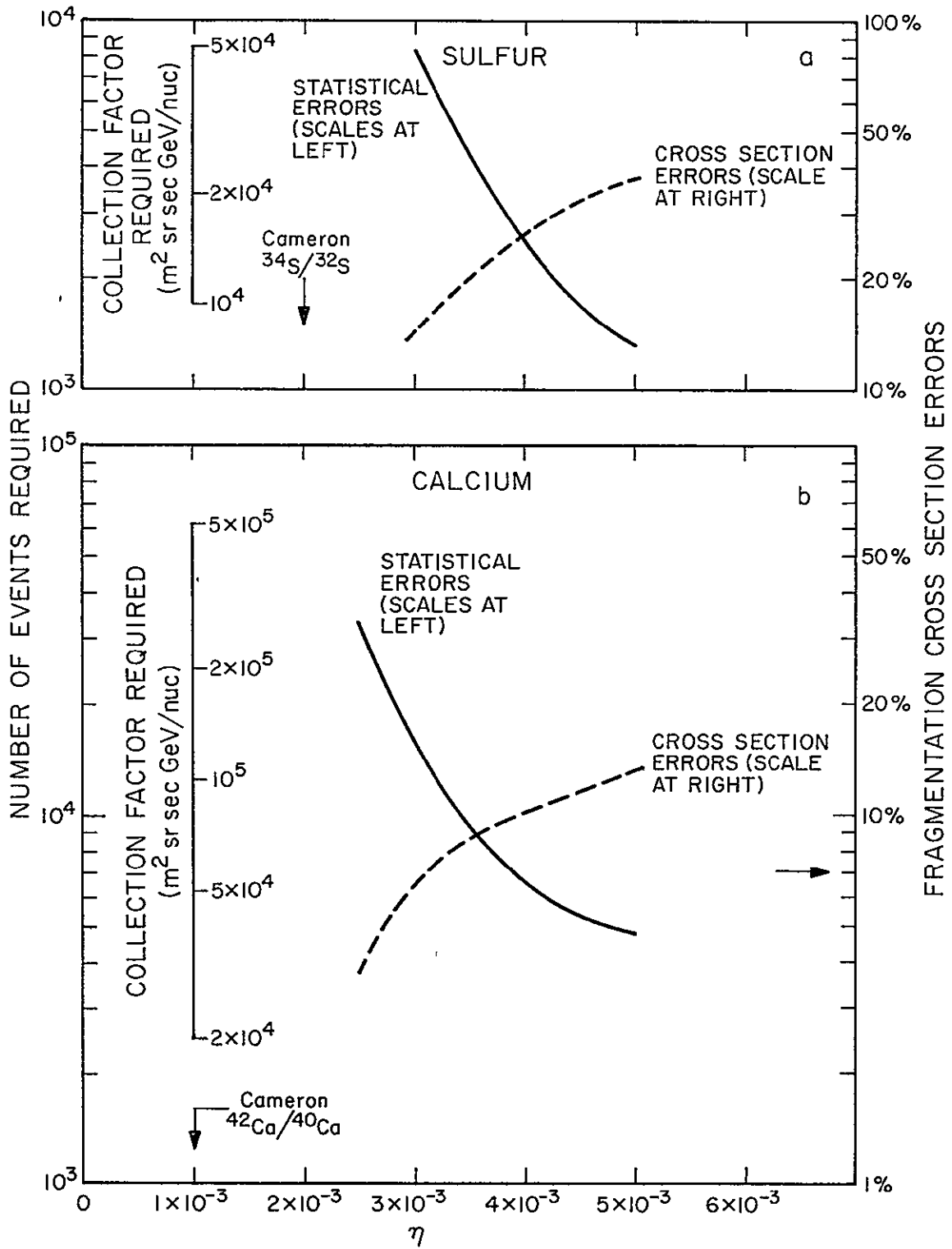
FIGURE 33

Numbers of events (solid curves) and level of fragmentation cross section errors (dashed curves) required in order to distinguish cosmic ray abundances synthesized by explosive oxygen burning in environments with various levels of the neutron excess,  $\eta$ , from abundances synthesized in an environment whose composition is solar-like. Also shown is a scale indicating the collection factors required in order to obtain various numbers of events in observations made near 500 MeV/nuc. The values of  $\eta$  at which the explosive oxygen burning model reproduces the solar value of the isotope ratios being considered are indicated. Finally, in the case of the calcium isotopes, we indicate by an arrow the level of fragmentation cross section errors below which other sources of calculational uncertainty exceed the uncertainty arising from the cross section errors (in the case of sulfur, the cross section errors are

ORIGINAL PAGE IS  
OF POOR QUALITY

dominant over the range which we are considering). The triplets of isotopes employed in obtaining the curves are:





ORIGINAL PAGE IS OF POOR QUALITY

distinguishable from solar-like abundances in the case of S and indistinguishable in the case of Ca

We have used the dependence of the isotopic ratios  $^{34}\text{S}/^{32}\text{S}$  and  $^{42}\text{Ca}/^{40}\text{Ca}$  on  $\eta$  from Woosley et al. (1973) the solar values of these ratios from Cameron (1973) and the error calculations described above to estimate the degree to which measurements of local fluxes and measurements of fragmentation cross sections must be improved in order to distinguish between production in a solar-like environment and production in a region with enhanced neutron excess. We have assumed that the two sources of error (measurement statistics and cross section errors) contribute equally to the error in determining  $q_j/q_k$  and we require that the overall error in  $q_j/q_k$  be 50% of the difference between the values of  $q_j/q_k$  for the solar case and for the value of  $\eta$  being considered.

In figure 33a we show, as a function of  $\eta$ , the number of sulfur events (solid curve) needed in order to reduce the statistical uncertainty in the calculated value of the source ratio  $^{34}\text{S}/^{32}\text{S}$  far enough to distinguish this ratio from the corresponding solar-like ratio. The collection factor ( $\text{m}^2 \text{sr sec (GeV/nuc)}$ ) required in order to obtain these numbers of events above the earth's atmosphere at an energy  $\sim 500$  MeV/nuc is also shown. The

dashed line shows the level to which uncorrelated errors in measurements of the relevant fragmentation cross sections must be reduced in order to make the same distinction between solar and non-solar environments. Figure 33b shows the corresponding values for the case of the source ratio  $^{42}\text{Ca}/^{40}\text{Ca}$ . In this case the calculated fractional error in the fragmentation cross sections must be reduced to a level which is so low that other calculation errors will no longer be negligible. In table 8 it can be seen that when the uncorrelated fragmentation cross section errors are reduced to  $\sim 7\%$  (in the solar-like case) they will contribute an amount equal to the combined effect of all other calculation errors to the error in  $q_j/q_k$ . Therefore even if the fragmentation cross section errors can be reduced to  $\sim 10\%$ , it will not be possible to distinguish a cosmic ray source with  $\eta \lesssim 4 \times 10^{-3}$  from a solar-like source unless other errors discussed in section 3.3.2 can also be reduced. In figures 33a and b we indicate the value of  $\eta$  at which the model of Woosley et al. (1973) reproduces the solar system value of the abundance ratio being considered. The difference of the two values of  $\eta$  is well within the accuracy expected from the nucleosynthesis calculations.

### 3.3.5 Solar Modulation Effects

In the above discussion we have assumed that observations could be made of abundances of the cosmic rays in local interstellar space. However, fluxes observed near earth have been modified by their interaction with the fluctuating magnetic field in the solar wind in penetrating to the orbit of earth. This phenomenon of solar modulation has been extensively studied. The subject has been reviewed by Jokipii (1971) and by Fisk (1974).

The effects of convection, diffusion and adiabatic energy loss on cosmic ray spectra are described by a Fokker-Planck equation (Parker, 1965). These effects will alter spectra by preventing a fraction (depending on magnetic rigidity) of the interstellar particles from penetrating to the earth's orbit and by redistributing particles having a particular energy in interstellar space over a range of degraded energies.

Gleeson and co-workers have shown (Urch and Gleeson, 1973; Webb and Gleeson, 1973; Gleeson and Webb, 1975) that those particles with a mass-to-charge ratio of 2 which are observed at a particular energy near earth originate in interstellar space from a distribution of energies whose mean is  $\sim 100-150$  MeV/nuc greater than the

ORIGINAL PAGE IS  
OF POOR QUALITY

observed energy during times of minimum solar activity and  $\sim 200-350$  MeV/nuc greater than the observed energy at solar maximum. These distributions are approximately Gaussian in shape with full width at half maximum in the range 30-50 MeV/nuc at solar minimum and 70-110 MeV/nuc at solar maximum. In addition, particles of lower M/Z but the same energy per nucleon lose more energy during solar modulation than those of higher M/Z. The difference in the mean energy loss by particles with M/Z=2.2 and those with M/Z=2 is  $\sim 20$  MeV/nuc at solar minimum and  $\sim 40$  MeV/nuc at solar maximum.

Isotopic abundance ratios measured at earth will differ from those which are present at the same energy in interstellar space due to two effects. First, due to the loss of energy during solar modulation the particles at a fixed energy at earth originated at higher energies in interstellar space. If the ratio being considered is strongly dependent on energy then the magnitude of the energy loss must be accurately determined in order to interpret the measured abundances. This situation occurs when one is considering the ratio of an isotope which has a large secondary component to one which is largely primary if observations are made below a few hundred MeV/nuc, since at these low energies many of the fragmentation cross sections exhibit a sizeable energy

dependence and the effects of ionization energy loss on the spectral shape become significant. At energies approaching 1000 MeV/nuc, however, the fragmentation cross sections are approximately independent of energy and ionization energy loss effects are unimportant so abundance ratios should approach a constant value.

Second, even if the interstellar spectra of the species of interest have a constant ratio at all energies, the ratio measured at a constant energy per nucleon at earth will be altered since different isotopes with the same energy per nucleon have different magnetic rigidities (proportional to their mass-to-charge ratios). The transmission of interstellar particles to earth and the redistribution of their energies is predominantly a rigidity-dependent process since it arises from the scattering of the particles from irregularities in the interplanetary magnetic field.

In order to estimate the magnitude of this effect we have performed a numerical solution of the spherically symmetric Fokker-Planck equation

$$0 = \frac{1}{r^2} \frac{\partial}{\partial r} \left[ r^2 \kappa \frac{\partial U}{\partial r} - \frac{\partial}{\partial r} (r^2 V_{sw} U) \right] + \frac{2V_{sw}}{3r} \frac{\partial}{\partial T} (\alpha \cdot T \cdot U), \quad (15)$$

using the method of Fisk ([97]). In this equation  $r$  is the radial distance from the sun,  $T$  is the kinetic energy

of the particles being considered,  $V_{sw}$  is the solar wind velocity (taken to be 400 km/sec),  $K$  is the diffusion coefficient. In addition,  $U$  is the number of cosmic ray particles per unit volume and per unit kinetic energy (related to the flux,  $j$ , by  $j = \beta c U / 4\pi$ ) and  $\alpha = (T + 2mc^2) / (T + mc^2)$  ( $mc^2$  being the rest energy of the particles being considered). We have assumed that the interstellar spectra of both species of interest are proportional to the interstellar spectra obtained by Garrard (1973) from studies of the modulation of H and He nuclei:

$$j\left(\frac{E}{M}\right) \propto \left(\frac{E}{M} + 0.75 \cdot (931 \text{ MeV/nuc})\right)^{-2.65} \quad (14)$$

The diffusion coefficient has been assumed to be of the form

$$K = k_0 \cdot \begin{cases} P & P \geq P_0 \\ \sqrt{P_0 P} & P < P_0 \end{cases}$$

where  $k_0$  and  $P_0$  are constants,  $P$  is the particle's magnetic rigidity and  $\beta c$  is its velocity. This form is assumed to apply within a radius  $D$  of the sun and it is assumed that there is no modulation outside of this radius. We have used Garrard's values for  $P$  and for the modulation parameter

$$\eta(1\text{AU}) = \frac{V_{sw}(D-1\text{AU})}{k_0} \quad (15)$$

where  $V_{sw}$  is the solar wind velocity and is assumed to have a constant value of 400 km/sec. Using values of  $D=10, 20$  and  $50$  AU we have used equation 15 to calculate  $k_0$ . The parameters  $k_0, P_0$  and  $D$  along with the spectrum 14 were used in obtaining spectra at 1 AU from equation 13. In table 9 we show the abundance ratios obtained at earth at a fixed energy per nucleon as a function of this energy for species having mass-to-charge ratios of 2 and 2.2. In addition to the results obtained from the numerical solution using the parameters given above, we show results obtained using the force field approximation (Gleeson and Axford, 1968) with the same values of  $\eta(1\text{AU})$  given by Garrard. It can be seen from the table that the effects of solar modulation are not sensitive to  $D$  if the value of  $\eta(1\text{AU})$  is held constant. At solar minimum direct comparison of abundances measured at a fixed energy at 1 AU will result in an error of  $\sim 5-15\%$  when comparing isotopes with  $M/Z=2$  and  $M/Z=2.2$  due to differences in the level of modulation at the different rigidities of these particles. At solar maximum this error increases to  $\sim 10-25\%$ . It will be necessary to apply the appropriate solar modulation corrections to abundance ratios measured near earth if solar modulation effects are not to be a

Table 9  
Correction Factors\* for Solar Modulation

E/M (MeV/nuc)	-- D=10 AU --		-- D=20 AU --		--D=50 AU --		force field	
	<u>1965</u>	<u>1970</u>	<u>1965</u>	<u>1970</u>	<u>1965</u>	<u>1970</u>	<u>1965</u>	<u>1970</u>
100	1.136	1.233	1.133	1.228	1.143	1.225	1.091	1.208
205	1.104	1.206	1.102	1.203	1.130	1.203	1.077	1.181
316	1.088	1.178	1.084	1.177	1.088	1.179	1.069	1.163
562	1.062	1.140	1.062	1.140	1.054	1.153	1.056	1.136
750	1.047	1.121	1.052	1.123	1.056	1.143	1.050	1.121
1000	1.045	1.102	1.041	1.106	1.045	1.111	1.043	1.106

\*  $[J(M/Z=2.2)/J(M/Z=2)]_{1AU} / [J(M/Z=2.2)/J(M/Z=2)]_{\pm 5}$

serious limitation on our ability to interpret such measurements.

Finally, we note that with the limited counting statistics achievable with present day instruments it will be necessary to combine data over a fairly large energy interval (at least several hundred MeV/nuc) in order to reduce statistical errors to an acceptable level. As a consequence, the averaging resulting from the solar modulation process should not presently severely limit the capability of these experiments.

#### 4. SUMMARY AND CONCLUSIONS

We have presented a detailed evaluation of the mass resolution capabilities of the Caltech HEIST instrument. The instrument employs an energy-loss - residual energy technique to make mass measurements of elements from Li through Ni at energies between 30 and 800 MeV/nuc. We have shown that Landau fluctuations in the energy loss measurement result in a fundamental limit to the achievable rms mass resolution which ranges from  $\sim .07$  AMU ( $Z \sim 3$ ) to  $\sim .2$  AMU ( $Z \sim 26$ ). Additional contributions to the mass uncertainty due to errors in measuring the trajectory and energy losses of cosmic ray particles have been shown to increase the overall rms mass resolution to  $\sim .1$  AMU for  $Z \sim 3$  and to  $\sim .3$  AMU for  $Z \sim 26$ . Such resolution will permit unambiguous separation of adjacent isotopes of the lighter elements and separation of isotopes differing by two mass units in the iron region (assuming that the isotope lying between these two has negligible abundance).

Cosmic ray isotope spectrometers will, within a few years, have provided data which will make it possible to tell whether the isotopic composition of the cosmic ray sources is dramatically different from the composition of solar system material. For example, if the composition of

ORIGINAL PAGE IS  
OF POOR QUALITY.

an element in the cosmic ray sources is dominated by a single isotope different from the isotope dominating the solar abundances, this difference should be readily identified.

We have gone on to evaluate in detail the uncertainties which will arise in deriving abundance ratios at the cosmic ray source from measurements made in local interstellar space. In this analysis we have considered elements which have at least one isotope which is likely to have a negligible abundance at the cosmic ray sources. This element is employed as a tracer of the production of secondary cosmic rays by means of spallation reactions during propagation. By basing secondary corrections to the observed fluxes on the observed abundance of a purely secondary isotope of the same element, we are able to avoid uncertainties resulting from the possibility of charge dependent acceleration mechanisms. This analysis was performed in the context of the leaky box model of cosmic ray propagation.

The uncertainties affecting the calculation of cosmic ray source ratios are of two types: 1) those arising from the statistical errors in the measured fluxes and 2) those arising from uncertainties in the calculation of the secondary component of these fluxes. In typical present

day cosmic ray experiments the statistical uncertainties in the derived source abundances should be significant, in some cases exceeding the abundances themselves.

The uncertainty in calculating the secondary corrections arises from the combined effects of uncertainties in a number of parameters employed in this calculation. The dominant contribution arises from uncorrelated errors in the important nuclear fragmentation cross sections. Many of the important cross sections have not yet been measured and are typically obtained from semi-empirical formulas. The uncertainties in these cross sections--estimated to be  $\sim 35\%$ --also produce source abundance uncertainties comparable to the abundances themselves. Measurements of the important cross sections can, of course, reduce this uncertainty. We have shown that it should be particularly useful to measure with high precision the ratios of cross sections for producing the isotopes of interest from individual parents. Even if errors  $\sim 35\%$  remain in the absolute cross sections, the effect of these errors on the calculated source ratio will be reduced by a factor  $\approx 2$ .

Other calculation uncertainties will become significant when the fragmentation cross section errors can be reduced by a factor of 3 or 4 from the 35% level

ORIGINAL PAGE IS  
OF POOR QUALITY

which we have assumed. The most important of these are due to: 1) uncertainties in the composition (both elemental and isotopic) of the parent species which are fragmented to produce the observed secondaries and 2) uncertainties in the shape of the equilibrium interstellar spectra of the isotopes which we are considering.

By assuming that all stable isotopes of a given element are, a priori, equally likely in the local cosmic rays, we obtain uncertainties of  $\approx 50\%$  in the calculated source ratios. In addition, we have shown that it is possible with specific parent isotope distributions to obtain significant systematic shifts of the calculated source ratio from the value obtained by averaging over randomly assigned isotopic compositions. For cosmic rays derived from a solar-like source, these shifts can be several times the standard deviation obtained from randomizing isotopic compositions. We have pointed out that since often the production of secondary cosmic rays is dominated by the spallation of species of approximately the same atomic number, it is likely that simultaneous measurements of the isotopic composition of an element of interest and of a few important parent elements will substantially reduce both the rms error and the systematic shifts which we obtain from randomized isotopic make-up of the parent element.

Uncertainties in the elemental composition of the parents also yield a source ratio uncertainty of  $\approx 50\%$ . Our estimates of these uncertainties are based on elemental composition errors which largely reflect the variation from experiment to experiment of the measured elemental abundances. These differences--presumably due to systematic errors in the measurements--should soon be reduced by measurements using higher resolution instruments with good statistical accuracy. Therefore the present uncertainties in the elemental composition of the parent population should not seriously limit our ability to calculate accurate source abundances.

Uncertainties in the shape of the spectra of the species of interest contribute source ratio errors which are typically  $\approx 30\%$ . Precise determination of the interstellar spectra requires flux measurements with large statistics at a number of energies and also accurate calculations of the effects of solar modulation. It is clear that such refinements will not be available for interpreting the data from the first generation of cosmic ray isotope experiments. We note, however, that the effects of uncertainties in the spectra will be minimized for measurements at energies in excess of  $1 \text{ GeV/nuc}$  since at these high energies the effects of ionization energy loss are minimized (and it is these effects which make the

ORIGINAL PAGE IS  
OF POOR QUALITY

spectral shape important). Also, at high energies the influence of solar modulation on the observed spectra will be less than at lower energies.

Families of curves were presented for the elements O, Ne, S and Ca (figure 32) which show the dependence of the resulting source ratio uncertainties on the observed fluxes. In computing the effect of the uncertainty in the calculation of the secondary contributions we have only considered the errors in the nuclear fragmentation cross sections, since presently these constitute by far the dominant source of calculational error. Curves showing the statistical errors were based on a total of 1000 events distributed among the three isotopes of the element being considered. The curves showing the errors due to fragmentation cross section errors were based on uncorrelated errors of 35% in these cross sections. The scaling of both types of errors has been discussed.

Using these curves we have examined the extent to which the uncertainties must be reduced in order to distinguish fairly minor differences in the isotopic composition at the cosmic ray sources. In so doing we have specialized to the case of abundances produced by means of explosive oxygen burning in environments exhibiting various levels of neutron excess. Using the

neutron excess as an independent variable we have shown the number of events and the level of fragmentation cross section errors which will be required in order to distinguish production in an environment with this neutron excess from production in a solar-like environment.

Finally we have shown that solar modulation effects are capable of altering the abundance ratios observed near earth by up to 25% from those present outside the heliosphere. Consequently solar modulation corrections must be made as a first step in interpreting any isotopic abundance observations made near earth.

ORIGINAL PAGE IS  
OF POOR QUALITY

## APPENDIX A -- UNCERTAINTY IN MEASURED ABUNDANCE RATIOS

In this appendix we obtain estimates of the uncertainty in abundance ratios obtained from measured mass distributions. In section A.1 we obtain a relationship between the desired uncertainty in a ratio and the number of events required in order to reduce the uncertainty to this level. This relationship depends on the magnitude of the ratio and on the mass resolution. In section A.2 we summarize the derivation of the relation between mass resolution and abundance ratio required to obtain an inflection point in the measured mass distribution. This relationship is a measure of the mass resolution required in order to insure that systematic errors cannot invalidate the deduced abundance ratios. In both of these treatments we consider only the case of two isotopes with non-negligible abundance and we assume that the mass resolution is equal for the two isotopes.

## A.1 Statistical Errors

We consider a mass distribution consisting of two Gaussian mass peaks having unit separation between their means, standard deviation  $\sigma$  and relative abundance  $r$ . The probability density for samples obtained from this distribution is:

$$p(M) dM = \frac{1}{\sqrt{2\pi}} \frac{1}{\sigma} \left[ (1-f) e^{-\frac{M^2}{2\sigma^2}} + f e^{-\frac{(M-1)^2}{2\sigma^2}} \right] \quad (A.1)$$

where  $f=r/(1+r)$ . If a sample of  $N$  events is obtained from this distribution, one can obtain an estimate of  $f$  by various means. One technique is to accumulate the measured events in mass bins and to use the maximum likelihood method (see, for example, Mathews and Walker, [970]) to obtain the most probable estimate of  $f$ . We will represent the number of counts in the  $i^{\text{th}}$  bin by  $n_i$  and the lower and upper limits of the  $i^{\text{th}}$  bin by  $M_i$  and  $M_{i+1}$ , respectively. Then the probability of any particular event falling in the  $i^{\text{th}}$  bin can be written as

$$\begin{aligned} p_i &= \int_{M_i}^{M_{i+1}} p(M) dM \\ &= (1-f) \left[ I\left(\frac{M_{i+1}}{\sigma}\right) - I\left(\frac{M_i}{\sigma}\right) \right] + f \cdot \left[ I\left(\frac{M_{i+1}-1}{\sigma}\right) - I\left(\frac{M_i-1}{\sigma}\right) \right] \quad (A.2) \end{aligned}$$

where

$$I(x) \equiv \int_{-\infty}^x \frac{1}{\sqrt{2\pi}} e^{-\frac{u^2}{2}} du .$$

Also, we denote by  $N$  the total number of events accumulated and by  $\sigma_i$  the uncertainty in the number of

events obtained in the  $i^{\text{th}}$  bin.

If the number of counts in each bin has a Gaussian distribution, then several simplifications result. First, the maximum likelihood estimate of  $f$  is simply the value of  $f$  obtained by performing a least squares fit of A.1 to the data:

$$0 = \frac{\partial}{\partial f} \left\{ N^2 \sum_i \frac{1}{\sigma_i^2} \left[ \frac{n_i}{N} - (1-f) \left( I\left(\frac{M_{i+1}}{\sigma}\right) - I\left(\frac{M_i}{\sigma}\right) \right) - f \cdot \left( I\left(\frac{M_{i+1}-1}{\sigma}\right) - I\left(\frac{M_i-1}{\sigma}\right) \right) \right]^2 \right\}.$$

Second, the uncertainty in our estimate of  $f$  can be obtained in simple analytical form as

$$\sigma_f = \left\{ N^2 \sum_i \left[ \left( I\left(\frac{M_{i+1}-1}{\sigma}\right) - I\left(\frac{M_i-1}{\sigma}\right) \right) - \left( I\left(\frac{M_{i+1}}{\sigma}\right) - I\left(\frac{M_i}{\sigma}\right) \right) \right]^2 \frac{1}{\sigma_i^2} \right\}^{-\frac{1}{2}} \quad (\text{A.3})$$

In the case which we are considering, the number of counts in each bin will have a Poisson distribution with mean  $Np_i$  and, hence, standard deviation  $\sqrt{Np_i}$ . However the central limit theorem of statistics (Mathews and Walker, 1970) guarantees that for sufficiently large values of  $Np_i$  this distribution approaches a Gaussian with these values of the mean and standard deviation. For the sake of simplicity we employ equation A.3 in all cases using  $\sigma_i = \sqrt{Np_i}$  to obtain

$$\sigma_f = \frac{1}{\sqrt{N}} \left\{ \sum_i \frac{\left[ \left( I\left(\frac{M_{i+1}-1}{\sigma}\right) - I\left(\frac{M_i-1}{\sigma}\right) \right) - \left( I\left(\frac{M_{i+1}}{\sigma}\right) - I\left(\frac{M_i}{\sigma}\right) \right) \right]^2}{(1-f) \left[ I\left(\frac{M_{i+1}}{\sigma}\right) - I\left(\frac{M_i}{\sigma}\right) \right] + f \left[ I\left(\frac{M_{i+1}-1}{\sigma}\right) - I\left(\frac{M_i-1}{\sigma}\right) \right]} \right\}^{-\frac{1}{2}} \quad (\text{A.4})$$

The simple scaling of  $\sigma_f$  in proportion to  $1/\sqrt{N}$  is likely to breakdown for small values of  $N$ .

The uncertainty in the abundance ratio,  $r$ , can be obtained from  $\sigma_f$  using

$$\sigma_r = \frac{\sigma_f}{(1-f)^2} \quad (\text{A.5})$$

We have evaluated equations A.4 and A.5 using 36 bins each of width  $\Delta M=0.2$  between  $M_{\min}=-3$  and  $M_{\max}=4$  in order to obtain the curves shown in figure 3. We have found that the values of  $\sigma_r$  obtained vary by less than 10% when  $\Delta M$  is varied between 0.05 and 0.5 and when  $M_{\min}$  is varied between -3 and -1 (with  $M_{\max}=-M_{\min}+1$ ).

## A.2 Systematic Errors

As discussed in section 2.1 the possible presence of systematic errors in the determination of particle masses makes it important to achieve sufficient mass resolution to obtain separate mass peaks for adjacent isotopes. As a criterion for separation we demand that Gaussian distributions with means separated by one unit have an inflection point. Mass resolution which is better than the value obtained by applying this condition will yield two distinct maxima in the mass distribution whereas worse

resolution will not. In the following treatment we will assume that no statistical uncertainties are present (i.e., that a large number of events has been accumulated).

We are considering the distribution  $p(M)$  given in equation A.1. The conditions for obtaining an inflection point in this distribution are  $p'(M)=0$  and  $p''(M)=0$ . Applying these conditions to equation A.1 we find that for  $f < 1/2$  there will be an inflection point at

$$M = \frac{1}{2} \left( 1 + \sqrt{1 - (2\sigma)^2} \right)$$

if  $\sigma$  and  $r \equiv f/(1-f)$  are related by

$$\frac{1}{r} = \frac{2\sigma}{1 + \sqrt{1 - (2\sigma)^2}} \exp\left(\frac{\sqrt{1 - (2\sigma)^2}}{2\sigma^2}\right).$$

This relationship between the mass resolution and the abundance ratio is shown in figure 4.

ORIGINAL PAGE IS  
OF POOR QUALITY

## APPENDIX B -- TRAJECTORY UNCERTAINTIES

In this appendix we evaluate the uncertainties in the trajectory of a particle as determined by measurements in our proportional counter hodoscope. In particular, we obtain uncertainties in the position at which the trajectory intersects various levels in the scintillator stack and the uncertainty in  $\sec\theta$ , where  $\theta$  is the particle's angle of incidence measured from the axis of the crystal stack.

We consider the case of four measurements of the x-coordinate and four of the y-coordinate made at various positions along the particle's track, and we assume that each of these measurements has an uncertainty of  $\sigma_{MWPc}$ . We illustrate this geometry in figure B.1. The origin of the z axis is chosen to coincide with the depth at which we wish to obtain the uncertainties in the absolute x and y positions of the track. We separately fit straight lines to the x and to the y measurements:

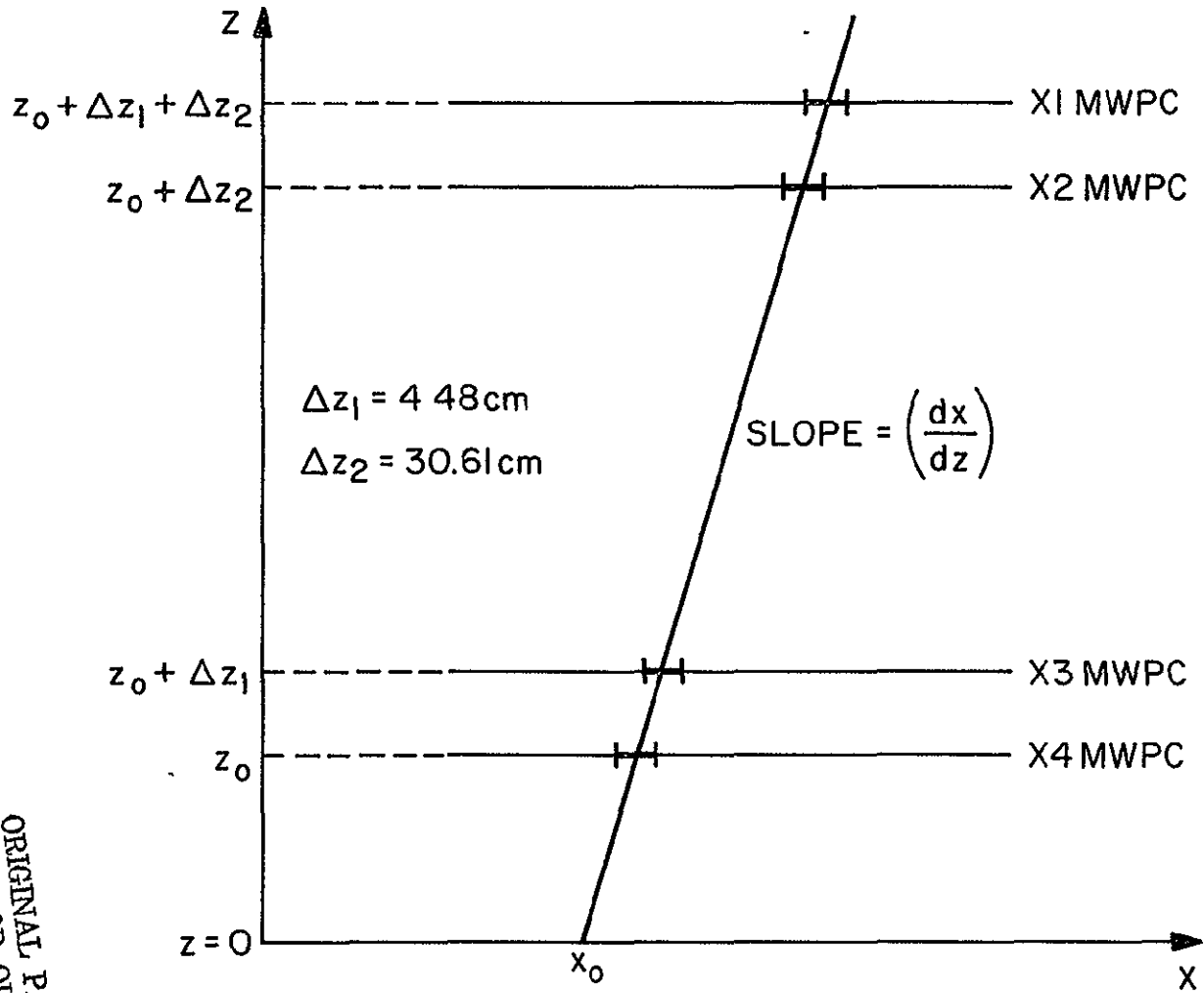
$$X = X_0 + \left(\frac{dx}{dz}\right)Z,$$

$$y = y_0 + \left(\frac{dy}{dz}\right)Z.$$

FIGURE B.1

Schematic illustration of parameters used to describe the hodoscope geometry ( $z_0, \Delta z_1, \Delta z_2$ ) and the trajectory of a particle ( $x_0, dx/dz$ ). Values of  $\Delta z_1$  and  $\Delta z_2$  for the HEIST hodoscope are shown.

ORIGINAL PAGE IS  
OF POOR QUALITY



The maximum likelihood method (Mathews and Walker, 1970) can be used to evaluate the parameters  $x_0$ ,  $y_0$ ,  $dx/dz$ , and  $dy/dz$ . In this case the maximum likelihood method reduces to a simple linear least squares fit and the coefficients are obtained by solving the matrix equation

$$\underbrace{\begin{pmatrix} \sum_{j=1}^4 \frac{1}{\sigma_{MWPC}^2} & \sum_{j=1}^4 \frac{z_j}{\sigma_{MWPC}^2} \\ \sum_{j=1}^4 \frac{z_j}{\sigma_{MWPC}^2} & \sum_{j=1}^4 \frac{z_j^2}{\sigma_{MWPC}^2} \end{pmatrix}}_{IM} \begin{pmatrix} x_0 \\ \frac{dx}{dz} \end{pmatrix} = \begin{pmatrix} \sum_{j=1}^4 \frac{x_j}{\sigma_{MWPC}^2} \\ \sum_{j=1}^4 \frac{x_j z_j}{\sigma_{MWPC}^2} \end{pmatrix}$$

The uncertainties in the fitted coefficients are obtained from the diagonal elements of the "error matrix",  $IM^{-1}$ ,

$$\begin{aligned} \sigma_{x_0} &= \sqrt{(IM^{-1})_{00}} \\ &= \left[ \frac{\sum \frac{z_j^2}{\sigma_{MWPC}^2}}{\left(\sum \frac{1}{\sigma_{MWPC}^2}\right)\left(\sum \frac{z_j^2}{\sigma_{MWPC}^2}\right) - \left(\sum \frac{z_j}{\sigma_{MWPC}^2}\right)^2} \right]^{1/2} \\ &= \frac{\sigma_{MWPC}}{2} \sqrt{1 + \frac{(2z_0 + \Delta z_1 + \Delta z_2)^2}{(\Delta z_1)^2 + (\Delta z_2)^2}} \end{aligned}$$

$$\sigma_{\frac{dx}{dz}} = \sqrt{(IM^{-1})_{11}}$$

$$\sigma_{\frac{dx}{dz}} = \left[ \frac{\sum \frac{1}{\sigma_{MWPC}^2}}{\left(\sum \frac{1}{\sigma_{MWPC}^2}\right)\left(\sum \frac{z_j^2}{\sigma_{MWPC}^2}\right) - \left(\sum \frac{z_j}{\sigma_{MWPC}^2}\right)^2} \right]^{\frac{1}{2}}$$

$$= \frac{\sigma_{MWPC}}{\sqrt{(\Delta z_1)^2 + (\Delta z_2)^2}}$$

The analogous expressions are obtained for  $y_0$  and  $dy/dz$ . Note, however, that in order to obtain  $x_0$  and  $y_0$  at the same depth in the crystal stack, different values of  $z_0$  must be used since each  $y$  measurement is made at a depth which is approximately 2.24 cm closer to the crystal stack than the corresponding  $x$  measurement.

#### B.1 Absolute Position Uncertainty

In table B.1 we list the ratio of the position uncertainties,  $\sigma_{x_0}$  and  $\sigma_{y_0}$ , at various depths in the HEIST scintillator stack to the position uncertainty,  $\sigma_{MWPC}$ , in each of the proportional counters. Values of  $\Delta z_1$  and  $\Delta z_2$  listed in figure B.1 are employed. It can be seen from table B.1 that this ratio varies between 0.87 and 1.09 depending on the depth in the scintillator stack. In our geometry the presence of redundant position measurements compensates for the degradation of position resolution due

Table B.1

Position Uncertainties in the Scintillator Stack

<u>Location in Scintillator Stack</u>	$\bar{z}_0$ for <u>x Measurement</u>	$\bar{z}_0$ for <u>y Measurement</u>	$\frac{\sigma_{x_0}}{\sigma_{MWPC}}$	$\frac{\sigma_{y_0}}{\sigma_{MWPC}}$
Top of D0	6.76 cm	4.52 cm	0.93	0.87
Top of D1	7.10 cm	4.86 cm	0.94	0.88
Top of D2	7.45 cm	5.21 cm	0.95	0.89
Top of D3	7.77 cm	5.53 cm	0.96	0.90
Top of D4	8.20 cm	5.96 cm	0.97	0.91
Top of D5	8.81 cm	6.57 cm	0.99	0.93
Top of D6	9.61 cm	7.37 cm	1.01	0.95
Top of D7	10.82 cm	8.58 cm	1.04	0.98
Bottom of D7	12.52 cm	10.28 cm	1.09	1.03

to the extrapolation of the trajectory from the hodoscope to the scintillator stack.

### B.2 Uncertainty in $\sec \theta$

We can obtain the uncertainty in  $\sec \theta$  from the expressions obtained above for  $\sigma_{\frac{dx}{dz}}$  and  $\sigma_{\frac{dy}{dz}}$  by noting that

$$\sec \theta = \sqrt{\left(\frac{dx}{dz}\right)^2 + \left(\frac{dy}{dz}\right)^2 + 1}$$

so that

$$\sigma_{\sec \theta} = \frac{1}{\sec \theta} \left[ \left(\frac{dx}{dz}\right)^2 \sigma_{\left(\frac{dx}{dz}\right)}^2 + \left(\frac{dy}{dz}\right)^2 \sigma_{\left(\frac{dy}{dz}\right)}^2 \right]^{\frac{1}{2}}$$

After simple algebraic manipulations we obtain

$$\frac{\sigma_{\sec \theta}}{\sec \theta} = \frac{\sin 2\theta}{2} \frac{\sigma_{\text{MWPC}}}{\sqrt{(\Delta z_1)^2 + (\Delta z_2)^2}}$$

Insertion of values of  $\Delta z_1$  and  $\Delta z_2$  from figure B.1 in this expression yields

$$\frac{\sigma_{\sec \theta}}{\sec \theta} = 0.0016 \sin 2\theta \cdot \sigma_{\text{MWPC}}$$

where  $\sigma_{\text{MWPC}}$  is expressed in millimeters.

REFERENCES

- Barkas, W. H., Berger, M. J., "Tables of Energy Losses and Ranges of Heavy Charged Particles," NASA SP-3013 (1964).
- Benegas, J. C., Israel, M. H., Klarmann, J. and Maehl, R. C., "Charge and Energy Spectra of Heavy Cosmic Rays," Fourteenth International Cosmic Ray Conference, Munich, 1, 251 (1975).
- Bevington, Philip R., Data Reduction and Error Analysis for the Physical Sciences, McGraw-Hill, New York (1969).
- Birks, J. B., The Theory and Practice of Scintillation Counting, MacMillan, New York, (1964).
- Breitenberger, Ernest, "Scintillation Spectrometer Statistics," Progress in Nuclear Physics, Frisch, O. R. (ed.), 4, 56 (1955).
- Brownlee, R. G., Chapman, G. J., David, S. A., Fisher, A. J., Horton, L., Goorevich, L., Kohn, P. C., McCusker, C. B. A., Outhred, A., Parkinson, A. F., Peak, L. S., Rathgeber, M. H., Ryan, M. J. and Winn, M. M., "The Energy Spectrum of Cosmic Radiation from  $10^{10}$  to  $2 \times 10^{20}$  eV," Acta Physica Academiae Scientiarum Hungaricae, 29, Supplement 1, 377 (1970).
- Caldwell, John H. and Meyer, Peter, "Charge Composition and Energy Spectra of Cosmic-Ray Nuclei at Energies Above 5 GeV per Nucleon," Fifteenth International Cosmic Ray Conference, Plovdiv, Bulgaria, 1, 243 (1977).
- Cameron, A. G. W., "Abundances of the Elements in the Solar System," Space Science Reviews, 15, 121 (1973).
- Cassé, M., " $^{56}\text{Ni}$  in Cosmic Rays?," Thirteenth International Cosmic Ray Conference, Denver, 1, 546 (1973).
- Cassé, M., Goret, P. and Cesarsky, C. J., "Atomic Properties of the Elements and Cosmic Ray Composition at the Source," Fourteenth International Cosmic Ray Conference, Munich, 2, 646 (1975a).

- Cassé, M. and Soutoul, A., "Time Delay Between Explosive Nucleosynthesis and Cosmic-Ray Acceleration," Astrophysical Journal Letters, 175 (1975b).
- Cassé, M. and Meyer, J. P., "Silicon, Sulphur, Argon, Calcium: Puzzling Thoughts on a Key Quartet," Fifteenth International Cosmic Ray Conference, Plovdiv, Bulgaria, 2, 131 (1977a).
- Cassé, M. and Goret, P., "Ionization Models of Cosmic Ray Sources," preprint OAP-499, Kellogg Radiation Laboratory, California Institute of Technology (1977b).
- Cesarsky, C. J., Cassé, M. and Paul, J. A., "Cosmic Rays, Spiral Structure and Molecular Clouds in the Galaxy," Astronomy and Astrophysics, 60, 139 (1977).
- Charpak, G., "Evolution of the Automatic Spark Chambers," Annual Reviews of Nuclear Science, 20, 195 (1970).
- Cheshire, D. L., Huggett, R. W., Johnson, D. P., Jones, W. V., Roundtree, S. P., Verma, S. D., Schmidt, W. K. H., Kurz, R. J., Bowen, T. and Krider, E. P., "Fragmentation Cross Sections of 2.1-GeV/nucleon  $^{12}\text{C}$  and  $^{16}\text{O}$  Ions," Physical Review, D10, 25 (1974).
- Cowsik, R., Pal, Yash, Tandon, S. N. and Verma, R. P., "Steady State Cosmic-Ray Nuclei--Their Spectral Shape and Path Length at Low Energies," Physical Review, 158, 1238 (1967).
- Doolittle, R. F., Polivogt, U. and Eskovitz, A. J., "Multiwire Proportional Chamber Development, Final Report," TRW Report (1973).
- Elliot, H., Thambyahpillai, T. and Peacock, D. S., "Search for a Siderial Anisotropy at 60 m.w.e. Depth," Acta Physica Academiae Scientiarum Hungaricae, 29, Supplement 3, 491 (1970).
- Evans, Robley D., The Atomic Nucleus, McGraw-Hill, New York (1955).
- Fisher, A. J., Hagen, F. A., Maehl, R. C., Ormes, J. F. and Arens, J. F., "The Isotopic Composition of Cosmic Rays with  $5 \leq Z \leq 26$ ," Astrophysical Journal,

205, 938 (1976).

- Fisk, L. A., "Solar Modulation of Galactic Cosmic Rays, 2," Journal of Geophysical Research, 76, 221 (1971).
- Fisk, Lennard A., "Solar Modulation," in High Energy Particles and Quanta in Astrophysics, McDonald, Frank B. and Fichtel, Carl E. (eds.), MIT Press, Cambridge, Mass. (1974).
- Garcia-Munoz, M., "Cosmic Ray Charge Composition ( $Z \leq 28$ )," Thirteenth International Cosmic Ray Conference, Denver, 5, 3513 (1973).
- Garcia-Munoz, M., Mason, G. M., Simpson, J. A. and Wefel, J. P., "Charge and Energy Spectra of Heavy Cosmic Rays at Intermediate Energies," Fifteenth International Cosmic Ray Conference, Plovdiv, Bulgaria, 1, 230 (1977a).
- Garcia-Munoz, M., Mason, G. M. and Simpson, J. A., "The Age of the Galactic Cosmic Rays Derived from the Abundance of  $^{10}\text{Be}$ ," Astrophysical Journal, 217 (1977b).
- Garrard, Thomas Lee, "A Quantitative Investigation of the Solar Modulation of Cosmic-Ray Protons and Helium Nuclei," Ph.D. thesis, California Institute of Technology (1973).
- Gleeson, L. J. and Axford, W. I., "Solar Modulation of Galactic Cosmic Rays," Astrophysical Journal, 154, 1011 (1968).
- Gleeson, L. J. and Webb, G. M., "Modulation and Spectral Redistribution of Galactic Cosmic Rays," Fourteenth International Cosmic Ray Conference, Munich, 3, 893 (1975).
- Gloeckler, G. and Jokipii, J. R., "Physical Basis of the Transport and Composition of Cosmic Rays in the Galaxy," Physical Review Letters, 22, 1448 (1969).
- Greiner, D. E., Lindstrom, P. J., Heckman, H. H., Cork, Bruce and Bieser, F. S., "Momentum Distribution of Isotopes Produced by Fragmentation of Relativistic  $^{12}\text{C}$  and  $^{16}\text{O}$  Projectiles," Physical Review Letters, 35, 152 (1975).
- Grove, R., Lee, K., Perez-Mendez, V. and Sperinde, J., "Electromagnetic Delay Line Readout for Proportional

- Wire Chambers," Nuclear Instruments and Methods, 89, 257 (1970).
- Grove, R., Ko, I., Leskovar, B. and Perez-Mendez, V., "Phase Compensated Delay Lines for Wire Chamber Readout," Nuclear Instruments and Methods, 99, 381 (1972).
- Grove, R., Perez-Mendez, V. and Sperinde, J., "Improved Delay Lines for Proportional Wire Chamber Readout," Nuclear Instruments and Methods, 106, 407 (1973).
- Hagen, Frank Andrew, "On the Age of Cosmic Rays as Derived From the Abundance of  $^{10}\text{Be}$ ," Ph.D. thesis, University of Maryland (1976).
- Hagen, F. A., Fisher, A. J. and Ormes, J. F., " $^{10}\text{Be}$  Abundance and the Age of Cosmic Rays: A Balloon Measurement," Astrophysical Journal, 212, 262 (1977).
- Hurford, Gordon James, "Observations of Hydrogen and Helium Isotopes in Solar Cosmic Rays," Ph.D thesis, California Institute of Technology (1974).
- Janni, Joseph F., "Calculations of Energy Loss, Range, Pathlength, Stragglng, Multiple Scattering, and the Probability of Inelastic Nuclear Collisions for 0.1-to 1000-MeV Protons," Air Force Weapons Laboratory technical report no. AFWL-TR-65-150 (1966).
- Jokipii, J. R., "Propagation of Cosmic Rays in the Solar Wind," Reviews of Geophysics and Space Physics, 9, 27 (1971).
- Lacy, J. L. and Lindsey, R. S., "High Resolution Readout of Multiwire Proportional Counters Using the Cathode Coupled Delay Line Technique," NASA Johnson Space Center, Cosmic Ray Group preprint (1973).
- Lindstrom, P. J., Greiner, D. E., Heckman, H. H., Cork, Bruce and Bieser, F. S., "Isotope Production Cross Sections from the Fragmentation of  $^{16}\text{O}$  and  $^{12}\text{C}$  at Relativistic Energies," Lawrence Berkeley Laboratory preprint LBL-3650 (1975a).
- Lindstrom, P. J., Greiner, D. E., Heckman, H. H., Cork, Bruce and Bieser, F. S., "Fragmentation of  $^{40}\text{Ar}$  at 100 GeV/c," Fourteenth International Cosmic Ray Conference, Munich, 1, 2315 (1975b).

- Lund, Niels, "Chemical Composition of the Cosmic Radiation and the Electron Component," Fourteenth International Cosmic Ray Conference, Munich, 11, 374b (1975).
- Mathews, J. and Walker, R. L., Mathematical Methods of Physics, second edition, Benjamin, New York (1970).
- Meneguzzi, M., Audouze, J. and Reeves, H., "The Production of the Elements Li, Be, B by Galactic Cosmic Rays in Space and its Relation to Stellar Observations," Astronomy and Astrophysics, 15, 377 (1971).
- Meyer, J. P., "Isotopic Composition of Cosmic Rays," Fourteenth International Cosmic Ray Conference, Munich, 11, 3698 (1975).
- Müller, Dietrich and Prince, Thomas, "Cosmic Ray Electrons: A Discussion of Recent Observations," Fifteenth International Cosmic Ray Conference, Plovdiv, Bulgaria, 1, 360 (1977).
- Northcliffe, L. C. and Schilling, R. F., "Range and Stopping-Power Tables for Heavy Ions," Nuclear Data Tables, A7, 233 (1970).
- Ormes, J. F., Fisher, A., Hagen, F., Maehl, R. and Arens, J. F., "A Balloon Measurement of the Cosmic Ray Element Abundances," Fourteenth International Cosmic Ray Conference, Munich, 1, 245 (1975).
- Parker, E. N., "The Passage of Energetic Charged Particles through Interplanetary Space," Planetary and Space Science, 13, 9 (1965).
- Perez-Mendez, V. and Parker, S. I., "Recent Developments in Delay Line Readout of Multiwire Proportional Chambers," IEEE Transactions on Nuclear Science, NS-21, 45 (1974).
- Perron, Claude, "Cross Sections for Production of Stable and Long-Lived Nuclides by High Energy Spallation of Iron; Cosmic Ray Implications," Physical Review, C14, 1108 (1976).
- Preston, Melvin Alexander, Physics of the Nucleus, Addison-Wesley, Reading, Mass. (1962).
- Raisbeck, G. M., Comstock, G., Perron, C. and Yiou, F., "Electron Capture Isotopes as Cosmic Ray

- Hydrometers," Fourteenth International Cosmic Ray Conference, Munich, 2, 560 (1975a).
- Raisbeck, G. M., Comstock, G., Perron, C. and Yiou, F., "Cosmic Ray Electron Capture Isotopes as Probes of Solar Modulation," Fourteenth International Cosmic Ray Conference, Munich, 3, 937. (1975b).
- Raisbeck, G. M. and Yiou, F., "Cross Sections for Spallation Production of  $^{44}\text{Ti}$ : Application to Determining Cosmic Ray Acceleration Time," Fifteenth International Cosmic Ray Conference, Plovdiv, Bulgaria, 2, 115 (1977a).
- Raisbeck, G. M., Menninga, C., Brodzinski, R. and Wogman, N., "Cross Sections for the Production of  $^{26}\text{Al}$  from Targets of Si, Al and Fe Irradiated by Protons of 600 MeV," Fifteenth International Cosmic Ray Conference, Plovdiv, Bulgaria, 2, 11b (1977b).
- Reames, D. V., "The Abundances of Nuclei in the Cosmic Radiation," in High Energy Particles and Quanta in Astrophysics, McDonald, Frank B. and Fichtel, Carl E. (eds.), MIT Press, Cambridge, Mass. (1974).
- Rossi, Bruno, High-Energy Particles, Prentice-Hall, Englewood Cliffs, N.J. (1952).
- Seltzer, S. M. and Berger, M. J., "Energy Loss Straggling of Protons and Mesons: Tabulation of the Vavilov Distribution," Studies in Penetration of Charged Particles in Matter, NAS-NRC Publication 1133, 187 (1964).
- Shapiro, M. M., Silberberg, R. and Tsao, C. H., "What New Cross Sections Say About Source Composition and Cosmic Ray Propagation," Fourteenth International Cosmic Ray Conference, Munich, 2, 532 (1975a).
- Shapiro, M. M. and Silberberg, R., "Cosmic-Ray Chronology from Isotopic Composition," Fourteenth International Cosmic Ray Conference, Munich, 2, 538 (1975b).
- Silberberg, R. and Tsao, C. H., "Partial Cross-Sections in High-Energy Nuclear Reactions, and Astrophysical Applications. I. Targets with  $Z \leq 28$ ," Astrophysical Journal Supplement, 25, 315 (1973a).
- Silberberg, R. and Tsao, C. H., "Cross Sections for Proton-Nucleus Interactions at High Energies," NRL

Report 7593 (1973b).

- Silberberg, R., Tsao, C. H. and Shapiro, M. M., "Semiempirical Cross Sections, and Applications to Nuclear Interactions of Cosmic Rays," in Spallation Nuclear Reactions and Their Applications, Shen, Merker (eds.), D. Reidel, Dordrecht-Holland, 49 (1976).
- Silberberg, R. and Tsao, C. H., "Calculations of Nucleus-Nucleus Cross Sections, and the Attenuation of Complex Cosmic-Ray Nuclei in the Atmosphere," Fifteenth International Cosmic Ray Conference, Plovdiv, Bulgaria, 2, 89 (1977).
- Soutoul, A., Cassé, M. and Juliusson, E., "Time Delay Between the Nucleosynthesis of Cosmic Rays and Their Acceleration to Relativistic Energies," Fourteenth International Cosmic Ray Conference, Munich, 2, 455 (1975).
- Soutoul, A., Cassé, M. and Juliusson, E., "Time Delay Between the Nucleosynthesis of Cosmic Rays and Their Acceleration to Relativistic Energies," preprint OAP-494, Kellogg Radiation Laboratory, California Institute of Technology (1977).
- Stone, E. C., "Cosmic Ray Isotopes," Thirteenth International Cosmic Ray Conference, Denver, 5, 3615 (1973).
- Stone, E. C., "Methods for the Determination of Z and M Using  $dE/dx$ , Čerenkov and Total Energy Measurements," invited paper, ESRO Workshop on "Research Goals for Cosmic Ray Astrophysics in the 1980's," Frascati, Italy (1974).
- Sullivan, J. D., "Geometrical Factor and Directional Response of Single and Multi-Element Particle Telescopes," Nuclear Instruments and Methods, 95, 5 (1971).
- Tsao, C. H., Shapiro, M. M. and Silberberg, R., "Cosmic Ray Isotopes at Energies  $>2$  GeV/amu," Thirteenth International Cosmic Ray Conference, Denver, 1, 107 (1973).
- Tsao, C. H. and Silberberg, R., "Break-up Cross Sections of Cosmic Rays with Nuclei in Interstellar Helium, in Air and in Detector Materials," Fourteenth

- International Conference, Munich, 2, 516 (1975).
- Urch, I. H. and Gleeson, L. J., "Energy Losses of Galactic Cosmic Rays in the Interplanetary Medium," Astrophysics and Space Science, 20, 177 (1973).
- Waddington, C. J., "A Chart of Cosmic Ray Isotopes," Fourteenth International Cosmic Ray Conference, Munich, 2, 521 (1975).
- Waddington, C. J., "The Cosmic Ray Nuclides," Fifteenth International Cosmic Ray Conference, Plovdiv, Bulgaria, rapporteur paper (1977).
- Webb, G. M. and Gleeson, L. J., "Monoenergetic-Source Solutions of the Steady-State Cosmic-Ray Equation of Transport," Thirteenth International Cosmic Ray Conference, Denver, 5, 3253 (1973).
- Webber, W. R. and Kish, J., "Cosmic Ray Isotope and Charge Resolution Using Large Area Scintillator-Cherenkov-Total Energy Telescopes," Nuclear Instruments and Methods, 99, 237 (1972).
- Webber, W. R., Lezniak, J. A., Kish, J. C. and Simpson, G. A., "A Measurement of the Abundance of Cosmic Ray Be and its Implications for the Cosmic Ray Age," Astrophysical Letters, 18, 125 (1977).
- Woosley, S. E., Arnett, W. David and Clayton, Donald D., "The Explosive Burning of Oxygen and Silicon," Astrophysical Journal Supplement, 26, 231 (1973).
- Woosley, S. E., "Importance of Isotopic Composition of Iron in Cosmic Rays," Astrophysics and Space Science, 39, 103 (1976).